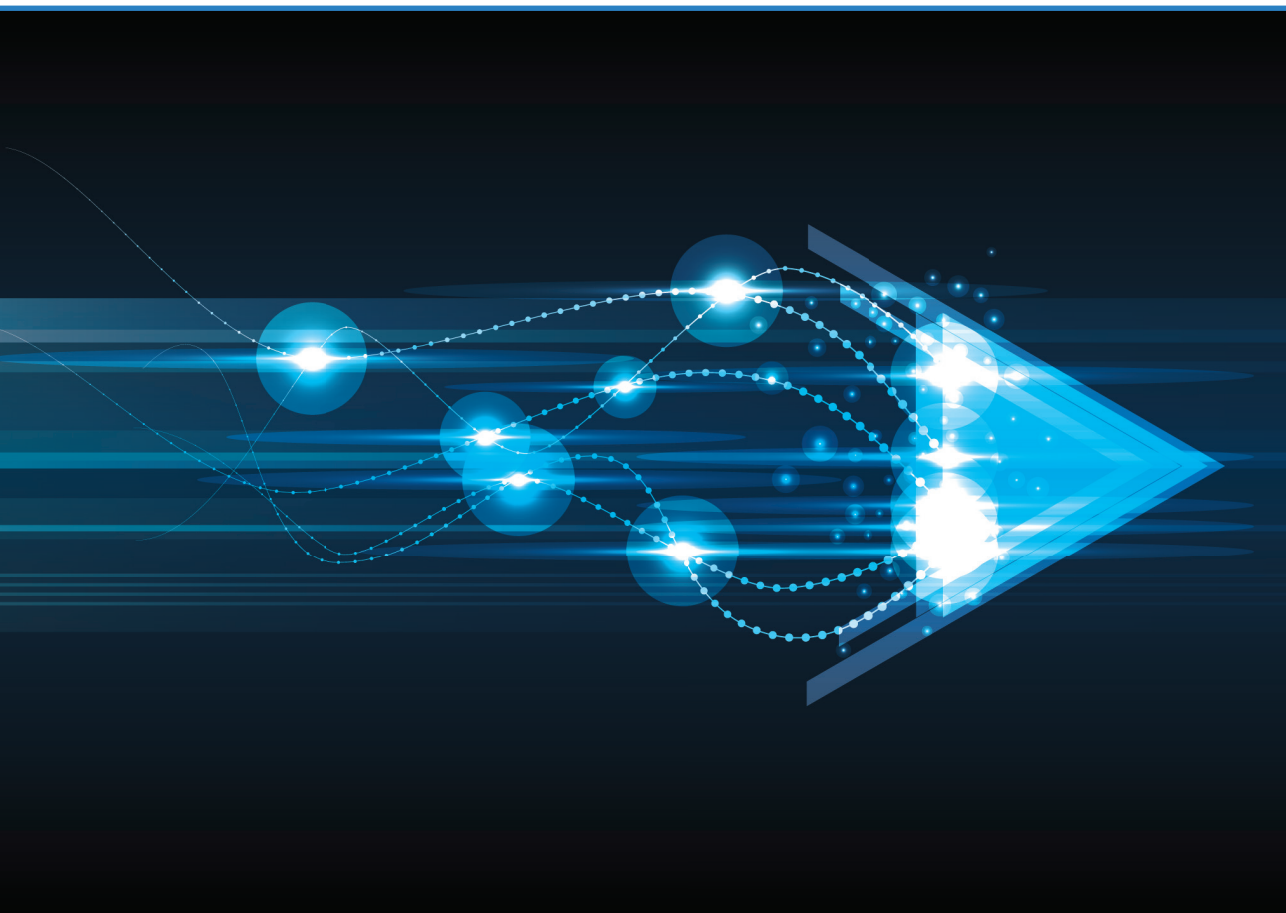**Aleksandr Krotov**

DEVELOPMENT OF OPTICAL COMMUNICATION SYSTEMS WITH HIGH-RELIABILITY OPTICAL SENSORS

Doctoral Thesis

RIGA TECHNICAL UNIVERSITY

Faculty of Computer Science, Information Technology and Energy
Institute of Photonics, Electronics and Telecommunications

Aleksandr Krotov

Doctoral Student of the Study Programme "Telecommunications"

DEVELOPMENT OF OPTICAL COMMUNICATION SYSTEMS WITH HIGH-RELIABILITY OPTICAL SENSORS

Doctoral Thesis

Scientific supervisors:

Professor Dr. sc. ing. Vjačeslavs Bobrovs

Ph.D. Svitlana Matsenko

RTU Press

Riga 2024

Krotov, A. Development of Optical Communication Systems with High-Reliability Optical Sensors. Doctoral Thesis. Riga: RTU Press, 2024. 119 p.

DOCTORAL THESIS PROPOSED TO RIGA TECHNICAL UNIVERSITY FOR PROMOTION TO THE SCIENTIFIC DEGREE OF DOCTOR OF SCIENCE

To be granted the scientific degree of Doctor of Science (Ph. D.), the present Doctoral Thesis has been submitted for defence at the open meeting of RTU Promotion Council on 30 August 2024 at the Faculty of Computer Science, Information Technology and Energy (FCSITE) of Riga Technical University (RTU), 12 Azenes Str., Room 201.

OFFICIAL REVIEWERS

Researcher, Ph.D. Semen Chervinskii

Tampere University, Finland

Professor, Ph.D. Lu Zhang

Zhejiang University, China

Professor, Dr.sc.ing. Aleksandrs Ipatovs

Riga Technical University

DECLARATION OF ACADEMIC INTEGRITY

I hereby declare that the Doctoral Thesis submitted for review to Riga Technical University for promotion to the scientific degree of Doctor of Science (Ph. D.) is my own. I confirm that this Doctoral Thesis has not been submitted to any other university for promotion to a scientific degree.

Aleksandr Krotov ……………………………. (signature)

Date: ………………………

The Doctoral Thesis has been prepared as a thematically united collection of scientific publications. It comprises eight scientific articles and publications in conference proceedings proceeding from the author's existing works indexed in SCOPUS, WoS, and IEEE databases. The publications are written in English; their total volume is 62 pages.

ACKNOWLEDGMENTS

LIST OF ABBREVIATIONS

A
AE – *Aviation Equipment*
ADC – *Analog-to-Digital Converter*
AirDC – *Air Data Computer*
APC – *Angled Physical Contact*
ARINC – *Aircraft Digital Video Interface*
B
BER – *Bit-Error-Rate*
BIC – *Bound States in the Continuum*
BRAS – *Broadband Remote Access Server*
BRAS-OLT – *Broadband Remote Access Server Optical Line Terminal*
C
CCD – *Charged-Coupled Device*
CDRSP – *Central Device for Switching and Routing Packets*
CLK – *Clock*
CPA – *Coherent Perfect Absorption*
CSMA/CD – *Carrier Sense Multiple Access with Collision Detection*
CWDM - *Coarse Wave Division Multiplexing*
D
DEMUX – *Demultiplexer*
DMA – *Direct Memory Access*
DNSSN – *LZP Project "Dynamics of Non-Scattering States in Nanophotonic"*
DSRP – *Device for Switching and Routing Packets*
E
EM – *Electronic Module*
EMO – *Electromagnetic Environment*
EMC – *Electromagnetic Compatibility*
ENZ – *Epsilon Near-Zero*
F
FS – *Functional Systems*
FEC – *Forward Error Correction*
FOC – *Fiber-Optic Communication*
FTTB – *Fiber-To-The-Building*
FCSITE – *Faculty of Computer Science, Information Technology and Energy*
G
GMI – *Generalized Mutual Information*
GPON – *Gigabit-Capable Passive Optical Network*
GPNS – *Generalized Positional Numeral Systems*
H
HIRF – *High-Intensity Radiated Field*
I
IEEE – *Institute of Electrical and Electronics Engineers*
IP – *Internet Protocol*
IPTD – *Average Network Transmission Delay*
IPDV – *Average Network Data Variation*
IPTV – *Internet Protocol Television*
IPET – *Institute of Photonics, Electronics and Telecommunications*
ITU–T – International Telecommunication Unit – Telecommunication Standardization Sector
K
KTH – *Royal Swedish Technical University*
L

LDPC-IRA – *Low-Density Parity-Check Irregular Repeat Accumulate*
LDPC – *Low-Density Parity Check*
LED – *Light-Emitting Diode*
LZP – *Latvian Council of Science*
M
MUX – *Multiplexer*
N
NEO-NATE – *LZP Project "Novel non-Hermitian Singularities in All-Dielectric Nanostructures"*
NIR – *Near-Infrared*
O
ONT – *Optical Network Terminal*
OLT – *Optical Line Terminal*
P
PAM – *Pulse-Amplitude Modulation*
PAM-M – *Multi-level Pulse Amplitude Modulation*
PS – *Power Splitter*
Q
QAM – *Quadrature Amplitude Modulation*
QoS – *Quality of Service*
R
RAM – *Random Access Memory*
REE – *Radio Electronic Equipment*
RLS – *Radio Location System*
RTU – *Riga Technical University*
Rx – *Reciever*
S
SNR – *Signal-Noise Ratio*
SFP – *Small Form-Factor Pluggable*
SIP – *Session Initiation Protocol*
T
TAU – *Tel Aviv University*
Tx – *Transmitter*
U
UART – *Universal Asynchronous Receiver / Transmitter*
UAV – U*nmanned Aerial Vehicles*
USART – *Universal Synchronous/Asynchronous Receiver/Transmitter*
V
VoD – *Video on Demand*
VoIP – *Voice Over Internet Protocol*
W
WDM – *Wavelength Division Multiplexing*
WDM-PON – *Wavelength Division Multiplexed Passive Optical Network*
WoS – *Web of Science*

CONTENTS

CHAPTER 1: OVERVIEW

1.1. Introduction

The development and improvement of modern aircraft onboard radio-electronic equipment (avionics) is associated with the implementation of information and telecommunication technologies. As a result, the requirements for data transmission networks on aircraft are constantly growing [1]. On the one hand, every year, the improvement of subscriber devices (traffic generators) of the aircraft on-board network [2], [3] requires the increased performance of aircraft onboard information and telecommunication networks: greater throughput, scalability, ensuring the required level of delays [4–6]. On the other hand, the execution of these requirements must be ensured with unconditional compliance with the mass-dimensional characteristics of avionics and the tendency to decrease them.

As a rule, any technical decision taken in relation to aviation equipment (AE) proceeds from a compromise between the weight, size, and characteristics that the AE product must provide while considering the fact that the AE has strict requirements for resistance to external factors, reliability, and electromagnetic compatibility [7], [8]. According to the complexity of the testing cycle of single products and the increasing complexity of the task, problematic situations often arise during the development or modernization of systems, complexes, and sets of AE. In particular, the solution to the problem of ensuring the proper characteristics of on-board information and telecommunications networks is complex [9], [10] but does not exclude the requirements imposed on the components of the whole system.

In aviation, the object of electromagnetic compatibility (EMC) research is an aircraft and its onboard equipment capable of generating electromagnetic interference [11] or being susceptible to it. A special research object is the external electromagnetic fields on the flight paths. The aircraft's onboard devices are divided into radio-electronic, electronic, and electromechanical; they are divided into potential sources and receptors of unintentional interference [12]. The EMC of the aircraft's onboard equipment is determined by the characteristics of three main objects: sources of unintended interference, interference detectors, and the environment in which interference is propagated from the source to the receptor.

Unintentional disturbances are considered sources of interference formed during the operation of aircraft onboard equipment and radiations of radio transmitting devices located outside the aircraft (land-based and sea-based and other aircraft). Onboard radio transmitters are the most powerful sources of unintentional interference on the aircraft [13]. They emit continuous and pulsed signals in the frequency range from 2 MHz to 10 GHz. Their capacities are 20... 400 watts – for continuous signals and up to several kW – for pulsed. The spectrum consists of the main and extra-local radiation, radiation at harmonics of the operating frequency, noise and transit radiation [14], [15]. Potential sources of interference in the aircraft are pulse power converters, engine ignition systems, pulse de-icing systems, and digital electronic systems [16]. The main parameters of the interference sources are the following: the interference power in the radio frequency (RF) range (f) and the width of the spectrum of generated interference $\Delta F_{gen}(f)$.

According to the degree of impact of failure on flight safety, aircraft systems are divided into four levels: **A**, **B**, **C** and **D** [**17**]. Level **A** includes systems that perform so-called "critical" functions. Their violation leads to catastrophic consequences [**18**]. Examples are telecommunications systems on board, electrical control, engine control, etc.

Level **B** includes electrical and electronic systems that perform a function, the violation of which leads to an emergency situation.

Level **C** includes electrical and electronic systems that perform functions, the violation of which significantly complicates flight conditions.

Level **D** includes electrical and electronic systems that perform functions, the violation of which does not significantly complicate the conditions of the flight.

Communication systems and aircraft navigation support systems are examples of level B and C systems, which are display systems that provide direction, location, and route data. Failure of a level B or C system is not catastrophic, but it can contribute to other failures.

Electromagnetic compatibility EMC depends on two factors:

- o internal electromagnetic environment (EMO) in the locations of equipment enclosures, antennas and antenna-feeder lines, information exchange lines of functional systems (FS), etc.;
- o the noise immunity of the radio receivers (RR) and the susceptibility of the avionics to interference.

To date, the greatest danger is expected from the impact of pulsed radiation fields at frequencies from 400 MHz to 10 GHz [**19**], [**20**], which mainly affect electronic circuits.

1.2. Rationale

Analysis of trends in the development of onboard information and telecommunication networks [**21–23**] and sensors [**24**], [**25**] in the conditions of high-intensity electromagnetic fields has allowed us to establish that significant improvements in the resistance of information networks to high-intensity electromagnetic fields are urgently needed today.

As a result of the analysis of the means of increasing durability, network organization and noise-resistant coding methods were identified, and sensors onboard aircraft were considered. System methodological problems and contradictions in the construction of networks, organization of coding, and use of pressure sensors were identified.

The analysis of existing scientific works in this field of research has shown that to build a secure network with guaranteed delivery of messages under increased electromagnetic impact [**26**], [**27**], modernization of the scientific and methodological apparatus is required. For these purposes, the prospects of applying the mainline fault-tolerant coding methods and the application of optical sensors to a new area of research are substantiated. This will allow methodological problems to be solved caused by the influence of electromagnetic fields on the onboard information and telecommunication network [**28**], [**29**].

The disadvantages of existing networks include the use of fiber channel cables with high weight and relatively low throughput, low resistance of transceivers to the effects of fields, as well as high susceptibility of electronic sensors of static and full pressure to the impact of EMV [**30**], [**31**].

1.3. The aim and tasks of the Doctoral Thesis

Summarizing the above-mentioned facts about the directions of development of on-board information and telecommunication networks and sensors in the conditions of high-intensity electromagnetic fields, the following **aim of the Doctoral Thesis is proposed:**

Experimentally develop approaches to the construction of information systems based on optical sensors and broadband access facilities that ensure the transmission of traffic from subscribers of the onboard network, meeting the requirements for ensuring the level of delays and requirements for electromagnetic compatibility of onboard equipment providing the possibility of including new devices in the existing network and upgrading existing ones.

To achieve the aim set, the following theses were put forward:

1. A specialized code implementation with irregular repetition and forward error accumulation more than triples the signal transmission efficiency of the aircraft's high-speed digital video interface using 16-QAM (quadrature amplitude modulation) and improves system stability when exposed to high-intensity radiated fields.

2. The use of deformable CuBe2Ni(Co) bronze membranes with a sinusoidal profile and a rigid center, along with light-emitting diodes and charge-coupled device arrays, for measuring membrane deflection allows for increasing the precision of absolute and static pressure sensor measurements by at least 50%, reducing energy consumption by at least 70%, decreasing the processing time required for information processing, and reducing the weight of the final sensor by at least 25 %, compared to frequency absolute and static pressure sensors.

3. By introducing asymmetry in the distribution of losses and gains through altering the thickness of the layers, one can transition to the point of generating coherent ideal absorption, characterized by a significant increase in generation intensity and a sharp rise in the quality factor exceeding 10^8.

1.4. The key tasks of the Doctoral Thesis

To achieve the set goal of the dissertation and to prove the proposed theses, it is necessary to perform the following **key tasks:**

1. Develop and implement a fiber optic access network and aircraft onboard network that optimizes channel resource allocation at specific wavelengths, leading to improved quality-of-service (QoS) indicators for traffic within the network that doubles network capacity compared to traditional wave multiplex technologies.

2. Develop a new pressure sensor, showcasing significant enhancements and performance indicators and improved efficiency gains that reduce data transmission, lower supply voltage requirements, and contribute to enhanced energy efficiency and system performance.

3. Explore the potential of non-Hermitian photonics based on insights gained from research, emphasizing the asymmetric characteristics that can be harnessed to achieve

desired optical functionalities, therefore, pave the way for further studies in advancing photonics technology and addressing challenges across various domains.

4. Enhance transmission efficiency within the ARINC-818 communication protocol by integrating LDPC-IRA coding, surpassing traditional methods by more than threefold and therefore addressing challenges related to high-intensity radiated fields (HIRF) interference, thereby enhancing system stability and reliability through improved coding efficiency.

1.5. Research methods

To perform the tasks outlined in the Doctoral Thesis and to analyze the problems, mathematical calculations, numerical simulations, and experimental measurements have been used. Numerical simulations were implemented in RSoft OptSim and VPI Design Suite simulation software, which are based on the nonlinear Schrödinger equation using the split-step method, the Fourier transform, and the Monte Carlo method for estimating the bit-error-rate (BER). Mathematical processing was also performed in Matlab, COMSOL, Ansys Lumerical, GPSS World, etc., mathematical modelling software.

The scientific experiments described in the Doctoral Thesis were carried out at The Institute of Photonics, Electronics and Telecommunications (IPET) of Riga Technical University (RTU) and at the Dynamics of Nanostructures' Laboratory at Tel Aviv University (TAU) in Israel.

1.6. Scientific novelty and main results

Novel achievements of the Doctoral Thesis are as follows:

1. The novelty of the dissertation is the developed methods of building highly reliable networks based on fiber optic access means and using optical sensors.

2. A new approach has been developed and tested to ensure traffic transmission from subscribers of the onboard network.

3. The concept of the coherent perfect absorption lasing associated with the quasibound state in the continuum or asymmetric non-Hermitian epsilon-near-zero-containing layered structures was proposed.

4. All new design of full and static pressure sensors with high accuracy in determining the deformation, high speed, and optical interface was developed.

Practical value of the Doctoral Thesis:

1. Highly reliable networks: The developed methods for building high-reliability networks based on fiber optic access means and using optical sensors provide a robust and efficient infrastructure for communication systems. This can improve network performance, increase reliability, and enhance data security.

2. At the Institute of Photonics, Electronics and Telecommunications (IPET) of RTU Faculty of Computer Science, Information Technology and Energy, an optical telecommunication onboard system with ARINC-818 interface capable of transmission

in HIRF environment and capable of changing FEC on the channel (*proposed for further experimental research*) has been experimentally developed and evaluated in mathematical simulation.

3. Transmission of traffic from subscribers: The new approach developed and tested to ensure the transmission of traffic from subscribers of the onboard network offers a solution for efficient data transfer within networks, especially in scenarios involving multiple subscribers. This can optimize network resources and improve data transfer speeds.

4. At the Institute of Photonics, Electronics and Telecommunications (IPET) of RTU Faculty of Computer Science, Information Technology and Energy FCSITE, a gigabit-capable passive optical network (GPON)-based high-potential setup with multiple subscribers for guaranteed traffic delivery checks for highly reliable networks has been created *(and is proposed for further experimental research)*.

5. Coherent perfect absorption lasing concept: The proposed concept of coherent perfect absorption lasing associated with the quasibound state in the continuum or asymmetric non-Hermitian ENZ-containing layered structures introduces a novel approach to lasing technology. This concept can potentially enhance the efficiency and performance of lasing devices, leading to advancements in laser technology.

6. Full and static pressure sensor design: The new design of a full and static pressure sensor with high accuracy in determining deformation, high speed, and optical interface offers a significant advancement in sensor technology. This sensor can be utilized in various applications, such as industrial monitoring, medical devices, and structural health monitoring, providing precise and reliable measurements.

7. At the Institute of Photonics, Electronics and Telecommunications (IPET) of RTU Faculty of Computer Science, Information Technology and Energy, a practical setup for verification of the functioning and assessment of the metrological characteristics of the developed design of the static and total pressure sensor according to the criterion of increasing the accuracy and speed has been experimentally developed and evaluated.

8. Overall, the practical value of this Doctoral Thesis lies in its innovative contributions to optical communication systems, sensor technology, and lasing concepts, which can potentially drive advancements in various industries and applications.

The results obtained in the Thesis were used in the following projects:

- LZP project "*Novel complex approach to the optical manipulation of nanoparticles (PHOTON)*" No. lzp-2022/1-0579
- LZP project "*Dynamics of non-scattering states in nanophotonic (DNSSN)*" No. lzp-2021/1-0048
- LZP project "*Novel non-Hermitian singularities in all-dielectric nanostructures (NEO-NATE)*" No. lzp-2022/1-0553

1.7. Structure of the Thesis

The Thesis is prepared as a thematically unified set of publications on the development of optical communication systems with highly reliable optical sensors and optical networks.

Chapter 1: Overview. This chapter describes the scope of the research, formulates the main research hypotheses, and discusses the importance of the novelty of research related to onboard access systems. It also presents a brief description of the Thesis structure and displays the list of publications and presentations at international conferences.

Chapter 2: Methodology. This chapter describes the fundamental factors necessary for successful quality of service improvement and basic approaches for the development contents of high-reliability networks. Three main stages are outlined.

2.1. Data Collection. The procedure is discussed in detail, which could be divided into three sub-stages.

2.2. Data Analysis. This subchapter considers different ways to get high-reliability optical networks according to collected data.

2.3. Methodology development. This subchapter presents the algorithms for forward error correction, methods of coherent perfect absorption and approaches for optical sensors for inclusion in information systems, including fundamental solid principles for robust light enhancement systems

Chapter 3: Main results. This chapter represents publications that reflect the main results obtained during the research and application of fiber optics communications and sensors onboard. The results are published in five cited sources in journals indexed in Scopus.

Chapter 4: Final remarks. This chapter represents the main conclusions and discussion of the challenges and their solutions concerning the practical application of optical communication systems with highly reliable optical sensors and broadband access.

1.8. Publications and approbation of the Thesis

The results of the Doctoral Thesis are presented in eight scientific articles and publications in conference proceedings indexed in SCOPUS, Web of Science (WoS), and Institute of Electrical and Electronics Engineers (IEEE) databases. The author has eight publications altogether. The main results of the Thesis were summarised in three scientific journals. The results of the research were presented at three conferences.

The results of the Doctoral Thesis have been presented at theer international scientific conferences.

1. **A. Krotov**, M. Krotov, S. Matsenko, T. Salgals, V. Bobrovs, "*Aircraft Optical Video Transmission Communication based on the Forward Error Correction Codes,*" 2023 Photonics & Electromagnetics Research Symposium (PIERS), Prague, Czech Republic, (**2023**), DOI: 10.1109/PIERS59004.2023.10221478

2. **A. Krotov**, S. Tarasov, A. Lunev, R. Borisov, D. Kushevarova, "*Data Acquisition and Processing Algorithm for Total and Static Pressure Measurement System,*" Engineering Proceedings*, (**2022**), 27(1):23, DOI: 10.3390/ecsa-9-13332

3. S. Matsenko, S. Spolitis, O. Borysenko, M. Pudzs, **A. Krotov**, V. Bobrovs, "*LDPC Code with Fractal Decoder Device for 100 Gbps PAM-M Optical Interconnect*," 2021 Photonics & Electromagnetics Research Symposium (PIERS), Hangzhou, China, (**2021**), DOI: 10.1109/PIERS53385.2021.9695128

The <u>results of the author's Doctoral Thesis are presented in</u> eight scientific articles and conference proceedings indexed in SCOPUS, WoS, and IEEE databases:

1. **A. Krotov**, M. Krotov, S. Matsenko, T. Salgals, V. Bobrovs, "*Aircraft Optical Video Transmission Communication based on the Forward Error Correction Codes,*" 2023 Photonics & Electromagnetics Research Symposium (PIERS), Prague, Czech Republic, (**2023**), DOI: 10.1109/PIERS59004.2023.10221478

2. D. Novitsky, A.C. Valero, **A. Krotov**, T. Salgals, A.S. Shalin, A. Novitsky "*CPA-Lasing Associated with the Quasibound States in the Continuum in Asymmetric Non-Hermitian Structures*, " ACS Photonics. 9., (**2022**), DOI: 10.1021/acsphotonics.2c00790

3. **A. Krotov**, S. Tarasov, A. Lunev, R. Borisov, D. Kushevarova, "*Data Acquisition and Processing Algorithm for Total and Static Pressure Measurement System*," Engineering Proceedings*, (**2022**), 27(1):23, DOI: 10.3390/ecsa-9-13332

4. R. Borisov, I. Antonec, **A. Krotov**, S. Tarasov, V. Bobrovs, "*Methodology for the Static and Total Pressure Sensor Development Based on Elastic Sensing Elements and Linear CCD Matrices*," International Review of Mechanical Engineering (IREME), (**2022**), Vol. 16, No. 1, DOI: 10.15866/ireme.v16i1.21118

5. S. Matsenko, O. Borysenko, S. Spolitis, A. Udalcovs, L. Gegere, **A. Krotov**, O. Ozolins, V. Bobrovs, "*FPGA-Implemented Fractal Decoder with Forward Error Correction in Short-Reach Optical Interconnects*," Entropy, (**2022**), 24(1):122, DOI:10.3390/e24010122

6. S. Matsenko, S. Spolitis, O. Borysenko, M. Pudzs, **A. Krotov**, V. Bobrovs, "*LDPC Code with Fractal Decoder Device for 100 Gbps PAM-M Optical Interconnect*," 2021 Photonics & Electromagnetics Research Symposium (PIERS), Hangzhou, China, (**2021**), DOI: 10.1109/PIERS53385.2021.9695128

7. **A. Krotov**, S. Artamonov, K. Kuprenyuk, V. Nikitina, N. Romanov, E. Sosnov, "*Possibilities for Increasing the Signal-To-Noise Ratio in Technical Vision Systems of Robotic Complexes Using Laser Structured Lighting*," International Review of Mechanical Engineering (IREME), (**2018**) 12. 328., DOI: 10.15866/ireme.v12i4.14583

8. **A. Krotov**, D. Volkov, N. Romanov, N. Gryaznov, E. Sosnov, D. Goryachkin, "*Method for measuring distortion in wide-angle video channels*," Journal of Applied Engineering Science, (**2018**), 16. DOI: 10.5937/jaes16-17344

CHAPTER 2: METHODOLOGY

2.1. Development of a mathematical model in the simulation environment of an information and telecommunication network

The main approaches to assessing the quality of service of Internet Protocol (IP) networks are specified in recommendation Y.1541 [**32**], according to which the leading indicators of the quality of service of multimedia traffic are the average network delay of the packet (frame) transmission of IP packet transfer delay (IPTD) and its variation (jitter) IP delay variation (IPDV).
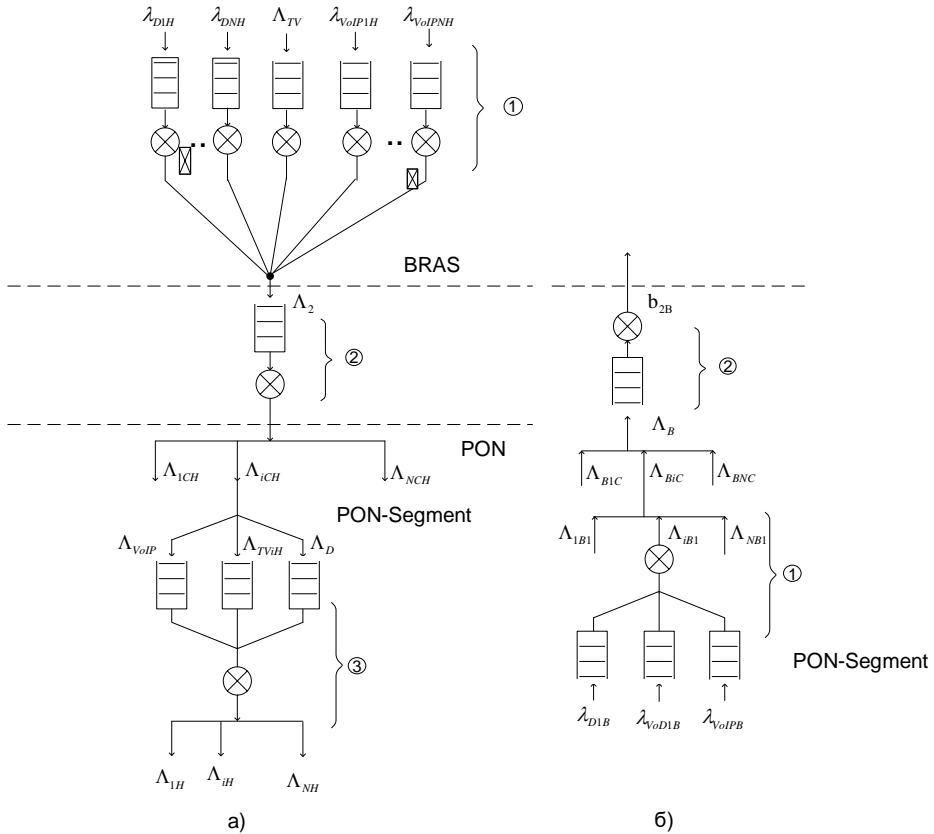
Fig. 2.1. Structure of the analytical model.

There is a GPON-based access network segment that is affected by three classes of subscriber traffic [**33**]:

- o <u>In the downstream branch</u>: traffic (highest service priority), with an average intensity $\lambda_{1HI} \ldots \lambda_{NHI}$ to all NN subscribers of the considered section of the access network, traffic (average service priority), with an average intensity Λ_{MI}, traffic of data transfer services to NN subscribers (lowest priority), with average intensity $\lambda_{1LI} \ldots \lambda_{DNI}$.

    o In the ascending branch: traffic of the highest priority, with an average intensity λ_{EH}, traffic of requests from one subscriber (medium priority) with an average intensity of λ_{1EM}, traffic of data transfer services from one subscriber (lowest priority) with an average intensity of λ_{1EM}. There are Nc segments operating in the broadband segment, each of which has N subscribers. It is required to determine the average IPTD packet (frame) delay for all types of traffic and the IPDV delay deviation [**34**] for traffic in the downstream and upstream branches. VoIP and IPTV.

It is assumed that:
- o The network is homogeneous and is in a steady state;
- o The intervals between the arrival of requests in the input flow of the descending branch are subject to the classical (two-parameter) Pareto distribution [**35**], [**36**], and the Poisson flow [**37**] acts on the ascending branch.
- o Service in both branches is multi-phase, in the first phase of the descending branch the duration of service intervals is subject to the classical Pareto distribution, and in the ascending branch the service is of a general type with three priority classes, as in the last phase of the descending branch;
- o In the upstream branch of GPON, each ONT transmits one Ethernet frame per access cycle;
- o The GPON segment is in operating mode;
- o The network is reliable.

The structure of the analytical model of the broadband access network under consideration in terms of queuing theory is shown in Fig. 2.1.

In the downstream branch (Fig. 2.1), flows of requests (Ethernet frames) are serviced in three phases: 1 - service in broadband remote access server (BRAS), 2 - service of the total traffic of the access node when it is transmitted over the broadband remote access server optical line terminal (BRAS-OLT) line, 3 - service in the GPON segment.

In the upstream branch (see Fig. 2.1), there are two phases of service: 1 - service of three classes of traffic coming from the subscriber in the GPON segment, 2 - service of the combined (total) access node traffic (from Nc GPON segments) when transmitted over the optical line terminal (OLT) line -BRAS. The phase numbers are shown in Fig. 2.1 in numbers in circles.

In the first phase (see Fig. 2.1), the average delay is calculated from the well-known Kraemer and Langenbach-Belz [**38**], [**39**] approximation for a G/G/1 type QoS.

For the classical Pareto distribution of intervals between requests in the input flow and service intervals in the first phase of the descending branch, the following expressions were used:

$$M = \frac{\alpha k}{\alpha-1} \ (1); \ \ D = \frac{\alpha k^2}{(\alpha-1)(\alpha-2)} \ (2); \ \ \upsilon^2 = \frac{1}{\alpha(\alpha-2)} \ (1),$$

where M is the average value, D is the dispersion, is the quadratic coefficient of variation, k is the lower limit of the distribution, and is a parameter of the distribution shape.

The IPDV delay deviation is calculated [37] as follows:

$IPDV = IPTD_{upper} - IPTD_{min}$, where $IPTD_{upper}$ calculated as the rank 0.999 quantile of the IPTD distribution function or approximately as the difference:

$$IPDV = IPTD_{max} - IPTD_{min} \ (2).$$

Considering expression (2) and the "three-sigma rule", for most types of delay time distributions, we can approximately estimate the delay deviation in a network section as $IPDV \approx 6\sigma_W$, where σ_W - standard deviation of the delay interval in this section, and $\sigma_W = \sqrt{\sum_{i=1}^n \sigma_i^2}$ (3), where n is the number of service phases, and σ_i - standard deviation in i - phase.

For phases 2 and 3 of the downstream branch and both phases of the upstream branch, we will calculate IPTD as the delay in the M/G/1 QoS with three classes of relative service priorities [**40**].

The total average intensity of the IPTV traffic flow affecting the last two phases of the downstream branch can be determined as follows:

$$\Lambda_{TV} = k_{mk}\lambda_{iTV} + N_0\lambda_{VoD} \text{ (4)},$$

where Λ_{TV} - total traffic intensity IPTV, k_{mk} - number of channels in a multicast group IPTV, λ_{iTV} - average flow intensity of one IPTV broadcasting channel, λ_{VoD} - the intensity of the "video on demand" stream per subscriber, N_0 - the total number of subscribers in the network (or in the GPON segment) who have subscribed to the Video on demand (VoD) service.

The average service time for the phases of the downstream branch is determined from the sum:

$$\bar{b}_{ijн} = \bar{t}_{ascijн} + \bar{t}_{desijн} \bar{b}_{ijн} = \bar{t}_{ascijн} + \bar{t}_{desijн} \text{ (5)},$$

where: $\bar{b}_{ijн}$ - average service time in i phase of the downward branch of requests j type (frames j – type of traffic), $\bar{t}_{desijн}$ - average processing time in i phase of the descending branch of requests j type, $\bar{t}_{ascijн}$ - average transmission time in i phase of the ascending branch of requests j type.

For the first phase of the ascending branch:

$$\bar{b}_{1jв} = \bar{t}_a + \bar{t}_{asc1jв} + \bar{t}_{des1jв} \text{ (6)},$$

where: $\bar{b}_{1jв}$ - average service time in the first phase of the ascending branch of j requests type, $\bar{t}_a$ - average access interval, $\bar{t}_{asc1jв}$ - average processing time in the first phase of the ascending branch of j-type requests.

$$\bar{t}_Д = \sum_{i=1}^{N-1} \Delta l_i \, t_P + \sum_{i=1}^{N-1} \bar{t}_{asc1jвi} \text{ (7)},$$

where Δl_i - increment of line length of the i subscriber, t_p - propagation delay per unit length of line used, $\bar{t}_{asc}$ - average time for transferring i-type requests.

The Δl_i parameter is defined as the difference between the maximum length of the OLT-optical network terminal (ONT) line in the GPON segment and the length of the line of the th-subscriber. To simplify the analysis, the value of this parameter averaged for the GPON segment was used.

Simulation models of the downstream and upstream branches of the GPON segment was developed in the GPSS World simulation environment.

To achieve this goal, a network structure can be used, which includes:
1. central device for switching and routing packets (CDSRP);
2. transmitting and receiving duplex optical replaceable modules configured for the used wavelengths $\lambda_1 ... \lambda_n$ (installed in special sockets of the CDSRP);

3.   the network end of the central OLT node, equipped with a wavelength division multiplexed (WDM) multiplexer and separation devices (passive fiber optic devices);
4.   single-fiber optical backbone up to 30 km;
5.   passive node, which is a WDM multiplexer (MUX);
6.   subscriber optical lines λ 1… λ N up to 3 km long;
7.   splitters 1x2 $P_1…P_N$;
8.   small Form-factor Pluggable (SFP) modules tuned to the corresponding wavelengths $λ_1... λ_N$;
9.   switching and packet routing devices (terminals $DSRP_1... DSRP_N$).

Any Ethernet switch or router that can install SFP modules in each port can be used as a CDSRP. Any of the modules available on the market can be used as SFP modules. For example, from inexpensive Coarse Wavelength Division Multiplexing (CWDM) lines [41] up to 16 wavelengths.

Modules should be selected with a significant excess of the maximum overlapped line length declared by the manufacturer in relation to the used length of the main line to ensure that the attenuation of elements of the passive path of the network is covered [42]. Thus, with an estimated length of the main line of 30 km (with subsequent testing on a laboratory test line of 40 km with a positive result), SPF modules were selected, designed for a point-to-point line length of up to 80 km, type TBSF15d-80-12g-LC-3c, to the corresponding CWDM grid wavelengths used.

Available coarse wavelength division multiplexing multiplexers (CWDM-MUX) were used as the network end of the central OLT node (CWDM-MUX 1x4 1550-1610 3.0 LC/APC 1.5 m were used for the four-port laboratory prototype). Devices for dividing propagation directions are connected to each of the divided ports of the multiplexer. These devices are made based on 1×2 planar splitters, which provide significant attenuation of the opposite direction of propagation (up to 30 - 40 dB) [43].

The single-fiber optical line used in the laboratory prototype tested was a 40 km line (4 reels of Fujikura fiber, 10 km each, connected in series). It is important to note here that all line connections in the network, especially the trunk line, except for the SFP module ports, must be made using a Subscriber Connector (SC) with Angled Physical Contact (APC) t.i. (green mark), which ensures minimal reflections. This is especially critical for the proposed technology.

The passive node uses a multiplexer like that used in OLT (without separating devices). The ONT used SFP modules like those used in the OLT. Splitters like those in OLT were used to separate transmission directions in ONT. Ethernet switches with one port equipped with sockets for installing SFP modules were used as the terminal DSRP. It was assumed that the proposed technology would be used in fiber-to-the-building (FTTB) class solutions, and subscriber wiring inside the building should be carried out using a standard category 5 network cable based on twisted pairs [Koonen, T. (2006). Fiber to the home/fiber to the premises: what, where, and when?. Proceedings of the IEEE, 94(5), 911-934.]. During laboratory tests, sets of subscriber equipment were connected to the end ports of network segments: video broadcasters, Session Initiation Protocol (SIP) telephones, personal computers (PC), and others.

Since the difference of the proposed network is the application in its segments of the principle of separating transmission directions according to the directions of propagation of the

light flux [**44**], [**45**], in such a network, the manifestation of mutual influence (interference) of transmission directions is inevitable, which is an additional source of specific interference and restrictions.

The main advantages of the proposed wavelength division multiplexed passive optical network (WDM-PON) are as follows.

1. Each end node of the proposed network monopolizes the entire channel resource of the bandwidth of the channel allocated at its wavelength, which significantly improves the quality-of-service QoS indicators for traffic in the proposed network.

2. In the proposed network, a doubling of the capacity (the number of connected nodes) is achieved compared to the use of traditional wave multiplex technologies due to the division of transmission directions not by wavelengths (as in traditional systems) but by the directions of propagation of the light flux. In the case of the proposed network, connecting each node will require only one wavelength, and not two, as in traditional WDM systems.

3. The proposed passive optical network (PON) provides complete logical transparency in dedicated channels and does not require any additional headers to be attached to the information packets (frames), such as in GPON. In addition, there is no dependence on throughput at the node level on the number of nodes included in the network segment or on the variation in the lengths of subscriber lines.

4. The proposed passive network uses wave division, and commercially produced domestic elements of fiber optic communication (FOC) can be used - optical transceivers SFPs, optical multiplexers / demultiplexers (DEMUX), optical circulators and splitters, as well as domestic information packet switches, including those with special certificates of conformity that have passed special checks and special studies. This eliminates the possibility (or reduces the likelihood of these events to a minimum) of the presence of undeclared functionality in the equipment of the proposed network, which ensures increased information security in the proposed network, performed based on imported, very large-scale integrated circuits.

Simulation modeling made it possible to obtain complete ideas about the process and estimates not only at the average values level but also standard deviations and histograms of distributions. Priority service mechanisms allow us to provide the best conditions for transmitting delay-sensitive traffic, even with identical service intervals for all types of traffic.

Increased energy saving, as well as the absence of the need to use switches, was achieved through the implementation of a synchronous, conflict-free method of access for network subscribers to a standard distribution medium (mono-channel), the use of acknowledgement of information frames during their transmission, the use of a fiber-optic physical distribution medium with one optical fiber, with separation of transmission directions optical signals by the method of separating the directions of propagation of the light flux.

As a prototype, a block of random multiple access to a monochannel using the carrier-sense multiple access with collision detection (CSMA/CD) method [**46**], described in was chosen. The random-access method with conflict resolution using the CSMA/CD method; it is a multiple access block with asynchronous random access to a monochannel that allows conflicts (collisions) of information frames transmitted over the network. The advantage of such systems is the ease of implementation of access blocks.

An obvious disadvantage of the prototype is the possibility of loss of information packet when transmitted through the network. Losses occur when frames received with errors are discarded in the receiving part of the access blocks [**47**], [**48**]. This disadvantage persists in modern networks that work with similar access units using Ethernet technology. This circumstance significantly limits the use of networks with access units, such as the prototype, in real-time data transmission systems that require guaranteed transmission of messages within a given limited time interval [**49**]. In systems using such an access method as in the prototype, data confirmation and auto-request of frames received with errors (discarded at the access level) are carried out by software protocols of the upper levels of the network hierarchy, which requires a period of time depending on the performance of computing devices, and the CSMA/CD access protocol used in the prototype does not provide a guaranteed frame transmission time in the event of errors and conflicts (in heavy load and interference modes). All these shortcomings limit the use of such widespread systems in conditions where strict requirements are imposed on the reliability (absence of losses and errors) of message transmission and the delay in transmitting frames through the network. Such requirements are imposed, for example, when transmitting control commands and other information in distributed real-time control systems [**50**].

Network operation in conditions of high-intensity fields involves the creation of such an optical local network access unit with guaranteed message delivery, which will ensure guaranteed delivery and low latency of information frames transmitted in the local network at the access level over the entire load range, will allow the implementation of a conflict-free access method, and will provide protection from errors that occur when transmitting frames through a common channel [**51**], [**52**], as well as low susceptibility to the effects of electromagnetic interference, interference and complete electrical isolation of the terminals included in the network, which creates additional noise immunity due to the lack of possibility of stray currents flowing [**53**, **54**], in addition, a network built based on the proposed access devices, assumes passive nodes and an economical single-fiber infrastructure, that is, it should ensure energy saving and resource conservation.

To achieve this goal, it is proposed to supplement the prototype with an optical transmitter, an optical receiver, a separating device, a transmitter and receiver of commands, a reference generator, an address setter, an analyzer, a switch S1 "central/peripheral" ("C/P"), an interface unit, and also use methods of traffic analysis discussed by including in the on-board computer an application for analyzing traffic from network devices.

It is proposed that an optical local network access block with guaranteed message delivery be configured as follows: a separating device, an optical transmitter, an optical receiver, a command transmitter and receiver, a reference oscillator, an address setter, an analyzer, an interface block, and the separating device has an optical interface towards a passive local splitter network and is connected by optical lines to an optical transmitter (Tx) and an optical receiver (Rx), and the optical transmitter and optical receiver are also connected to a linear encoder/decoder, which is also connected to the output of the "or" circuit, to the reception Random-access memory (RAM), to an error detector, a frame selector, and a synchronization unit and control, a command receiver, a reference generator, and the reference generator is also connected to a frame selector, an interface block, a command transmitter Tx and receiver Rx, a synchronization and control block, which is connected to the analyzer and switch S1, also

connected to the analyzer, with a readiness trigger , also connected to the transmission RAM, command receiver and transmitter, with an error detector, with the transmission RAM, while the address setter is connected to the command receiver and transmitter, frame selector, interface unit, the first input of the "OR" circuit is connected to the transmission RAM, and the second its input is connected to the command transmitter, the error detector is connected to the command transmitter, the second input of the "AND" circuit, the first input is connected to the frame selector, and the output is connected to the interface block to which the transmit and receive RAM is connected.

2.2. Development of approaches for optical pressure sensors for the information and telecommunication networks in aircraft

The proposed sensor (Fig. 2.2). for static and total pressure contains a housing (1) with two holes, respectively, for measuring static Pst and total Ptot pressure, and the holes are located above and below the gap formed by membranes (2) and (3).
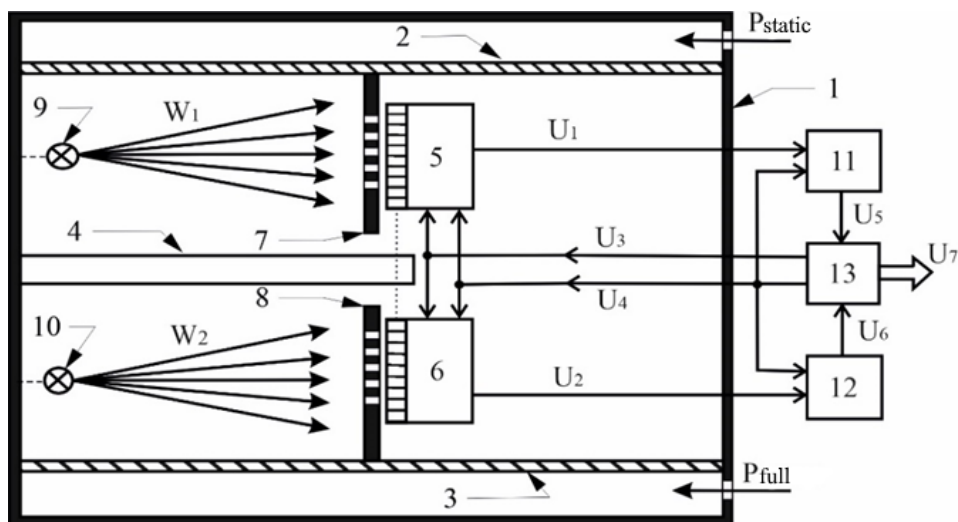
Fig. 2.2. Pressure sensor:
1 – housing with two holes; 2 and 3 – membranes; 4 – stand, 5 and 6 – photodetectors; 7 and 8 - curtains with slits (slots); 9 and 10 - radiation sources; 11 and 12 analog-to-digital converter (ADC); 13 - microcontroller.

Membranes 2 and 3 of the aneroid-sensitive elements are spaced apart in height, forming a gap from which air is pumped out, and are sealed around the perimeter of the body. Inside the airless gap, symmetrically relative to membranes 2 and 3, there is a stand 4, rigidly fixed to the side wall of housing 1. Above and below relative to stand 4, optical radiation sources 9 and 10 (for example, LEDs or optical fiber) are rigidly fixed to the side wall of the housing 1. Opposite the radiation sources 9 and 10 there are photodetection lines 5 and 6, rigidly fixed to the stand 4. Curtains 7 and 8 containing n slits are rigidly attached to the rigid centers of the membranes 2 and 3, which perceive static and total pressure, respectively. Photosensitive areas of the rulers are located along

the direction of movement of the curtains when the measured pressure changes. In this case, shutter 7 is in front of the photosensitive area of line 5, and shutter 8 is in front of the photosensitive area of line 6. The output of line 5 is connected to the input of ADC 11, and the output of line 6 is connected to the input of ADC 12. The outputs of ADC 11 and ADC 12 are connected to the first and the second inputs of microcontroller 13, the first and second control outputs of which are connected to two control inputs of both photodetector (PD) lines, and the second control input is also connected to the control inputs of both ADCs. The output of the microcontroller is connected to the input of the aerometric pressure recording device 14.

The operation of the device when measuring static pressure is as follows. In the initial state, membrane 2 of the aneroid-sensitive element occupies a certain position. Optical radiation W_1 from source 9 falls on curtain 7 and, passing through n slits, forms n light spots the size of several elements (pixels) of the line on the photosensitive surface of the photodetection line 5. As a result of the operation of the photodetection array, a periodic electrical signal is formed at its output (with a period equal to the time required for sequential interrogation of all pixels of the array), in which the distribution of optical power incident on its surface is reflected in the change in the amplitude of the signal U_1 (Fig. 2.3).

The operation of photodetector line 5 is ensured by supplying control signals U_3 and U_4 from the microcontroller. The control signal U_3 determines the beginning (the first pixel) when sequentially polling all pixels of the line. The second signal U_4 sets the polling period for each individual pixel of the line. The amplitude of the electrical signal U1 at the output of line 5 at each moment of time is proportional to the optical power incident on the pixel currently being interrogated. As a result, a periodic electrical signal U_1 is generated at the output of the line of photoelectronic receivers (5), in which the spatial distribution of optical power within the photosensitive surface of line 5 is matched with the time distribution of the amplitude of the electrical signal within the period of the signal U_3. Thus, n local maxima will be observed in the output signal of the photodetector array, corresponding to signals from the pixels that receive radiation passing through n slits in curtain 7.
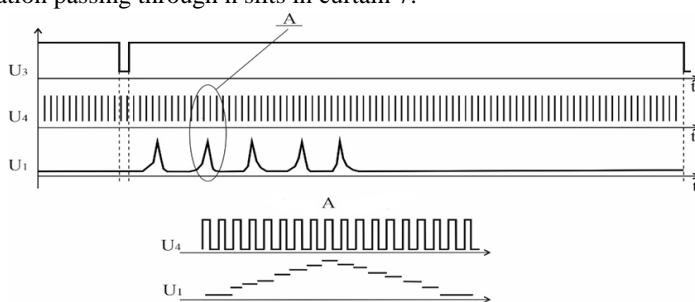
Fig. 2.3. Signal distribution on elements of a line of photoelectronic receivers.

Further processing of the output signal of the photodetector array occurs in digital form. For this, an ADC 11 is used, which converts the signal amplitude from each pixel of the line into a digital code corresponding to the amplitude. To synchronize the sampling moments [54] of the ADC with the operation of the photodetector line, signal U4 is supplied to the control input of the ADC. An array of signal amplitude values from the pixels of the line from the output of the

ADC 11 in the form of a signal U_5 is supplied to the input of the microcontroller 13. The microcontroller software processes the array of data received during one period of the signal U_3. The processing task is to calculate the coordinates of n light spots on the surface of the photodetector array. Coordinate values are expressed in pixel numbers.

To calculate the coordinates of the light spot, you can use the so-called centroid method [**55** - **57**], which provides the calculation of the coordinates of the "center of gravity" of the image of the light spot. The algorithm for this calculation can be implemented as follows: first, the numbers of n pixels Nmax_n are determined, the signal amplitude from which corresponds to local maxima within each of the n light spots on the photosensitive surface of the ruler, then an area of M/2 pixels up to and M/2 pixels is selected after the maximum. And for this area, the coordinates of the maximum signal are calculated, expressed in pixel number using the formula:

$$MAX_n = \frac{\sum_{i=N_{max\_n}-M/2}^{N_{max\_n}+M/2} A_i i}{\sum_{i=N_{max\_n}-M/2}^{N_{max\_n}+M/2} A_i}, \tag{8}$$

where is MAX_n – coordinate of the maximum of the n-th light spot on the line of photoelectronic detectors, Ai is the amplitude of the signal from the i-th pixel in the vicinity of the n-th spot, Nmax_n is the number of the pixel whose amplitude is maximum within the n-th spot. The number of pixels M/2 is selected in such a way as to cover all pixels around the local maximum, the signal amplitude from which noticeably exceeds the initial (dark) level.

The measurement algorithm represents two infinite parallel loops:

1. Cycle
    1.1. Launching a regular ADC channel by a trigger from a timer with values stored in a data array using direct memory access (DMA).
    1.2. After each conversion, the ADC interrupt handler changes the clock (CLK) level to the opposite one. This approach of generating CLK pulses for a line consisting of 2087 pixels allows us to obtain a data array of 4174 values.
    1.3. After half of the data array is filled, the DMA interrupt handler sets the readiness flag for the results of polling the first half of the pixels of the line.
    1.4. After filling the entire data array, the DMA interrupt handler sets the readiness flag for polling results of the second half of the pixels of the line. In addition, an reset signal is generated, and a new line polling cycle begins.

2. Cycle
    2.1. Tracking the polling status of the first half of the pixels of the line. If the data array readiness flag is set, the data is copied to another memory area and mathematical processing is performed.
    2.2. If averaging is not performed, the resulting result is output via the universal asynchronous receiver / transmitter (UART) interface.
    2.3. Monitoring the polling status of all pixels in the line. If the readiness flag of the entire array is set, then the data is copied to another memory area and mathematically processed.
    2.4. If averaging is not performed, the resulting result is output via the UART interface.

2.5. If averaging of results is used, then either the average value of the results obtained after mathematical processing of the first and second half of the data array is calculated or the averaging of the results of several cycles of polling the ruler.

2.6. Output of the obtained result via the UART interface.

It is important to note that with this approach to signal processing, it is necessary to structurally ensure the movement of optical spots only on its half of the photodetector array [58–60].

The mathematical processing is as follows:
$$\Delta\omega_0 = k_x(MAX_n(t) - MAX_n(0)), \qquad (9)$$
where k_x is a coefficient, the value of which depends on the geometric dimensions of the pixels and their relative position in the line.

Thus, for a charge-coupled device (CCD) line ILX554B with a pixel size of 14x56 μm, the coefficient kx = 0.007. $x_i = \frac{\Delta\omega_0(t)}{n}$. $\qquad (10)$

During the experiment, the sample was taken as the value of the deflection of the rigid center of the membrane ω0, obtained because of digitization and mathematical processing of the signal of the photodetector line after interrogating half of the line, as the measured value x, transmitted via the universal synchronous/asynchronous receiver/transmitter (USART) interface to the PC.

To confirm the statistical stability of the measurement results, whether they belong to the normal distribution law was checked. Since the value of m > 50, K. Pearson's χ2 criterion was used for verification [61], [62]. As a result of analyzing the results obtained, the null hypothesis of normal distribution is accepted for all four experiments. Figire 2.4 shows a histogram of the probability density and a histogram with an overlay of the theoretical normal distribution function.
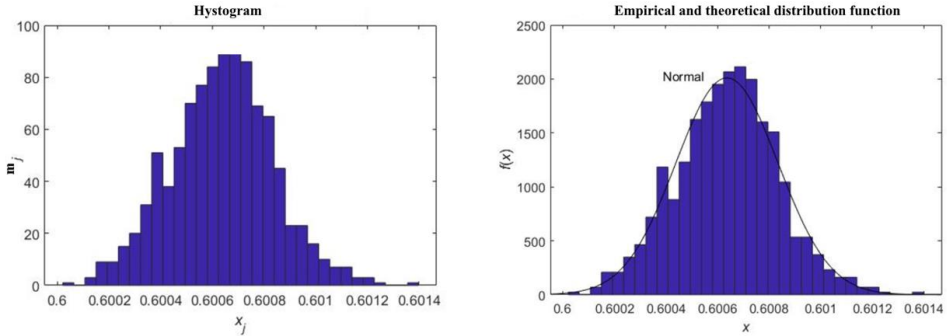
Fig. 2.4. Histogram and functions of empirical and theoretical distributions.

2.3. Development of a methodology for optimal noise-resistant coding for onboard computer networks in aircraft

Like any linear block code [63], a low-density parity check (LDPC) code can be described using a $k \times n$ generator matrix G, where k is the length of the information sequence and n is the length of the code block. Then the code vector **C** will be obtained by multiplying the information sequence m by the generating matrix G:

$$C = m\ G. \tag{11}$$

For a systematic LDPC code, the generator matrix can be represented as $G = [I, P]$, where I — unit size matrix $k \times k$ [**64**], [**65**]. Then the code will be described by the check matrix $H = [P^T, I]$, and:

$$C\ H^T = 0. \tag{12}$$

For any linear (N, K) code there is a bipartite graph incident to the matrix H. The Tanner graph consists of N code vertices and M=N–K control vertices. The code and verification vertices are connected by edges according to the parity matrix H.

The elements of such a matrix are the coefficients of the test equations, from which the test symbols are calculated. For efficient LDPC codes, the check matrix H must be sparse [**66**], [**67**], and the density of units in it, as a rule, is several tens or hundreds of thousands of elements.

For any linear (N, K) code, there is a bipartite graph incident to the matrix H. This graph is known as the Tanner graph, named after its discoverer. The Tanner graph consists of N code vertices and M = N–K control vertices. The code and verification vertices are connected by edges in accordance with the parity matrix H.

Generalized positional numeral systems (GPNS) can have very useful properties, such as noise immunity and ease of creating permutations [**68–70**]. When generating and numbering combinatorial objects, special development methods are used for each individual task, which can be characterized as a fundamental drawback of this approach [**70**], [**71**]. Binomial number systems and the homogeneous binomial numbers generated by them are a new result in the field of generalized positional number systems [**72**], [**73**]. The first seminal manuscript that gave rise to binomial systems was a paper published more than 30 years ago.

The binomial number system is finite and efficient [**74**]. A numbering algorithm converts the codeword Ai to its quantitative equivalent QAi after a finite number of steps. The binomial system is well-defined because two different coding combinations cannot be equivalent to the same numerical value.

Table 1 contains binomial combinations and their quantitative equivalents for a k-binomial system with n registers, where n = 6 and k = 4. They are generated using the following algorithm:

Step 1. An initial combination A_0 is composed, consisting of (n k) zeros, which is called a keyword.

Step 2. The number 1 is placed in the right end register, and a zero is added to the right of it.

Step 3. As long as the number of units in the codeword is less than k - 1, step 2 is repeated. If the number of units is equal to k - 1, then go to step 4.

Step 4. If the right end position contains a zero, it is replaced with a 1. Go to step 5.

Step 5. Check the number of ones in the code combination: if it is equal to k, but the ones do not occupy the first k registers, counting from left to right, go to step 6. Otherwise, i.e., if the ones occupy the first k registers, counting from left to right, then STOP: all combinations are generated.

Step 6. Updates keyword A_0 by taking 1 as a prefix before the start of the keyword (i.e. its left end). If the total number of units in the keyword is less than k, go to step 2.

Another method is based on the fact that the range of binomial numbers of length n and with parameter k (k < n) coincides with the range of constant weight encoding combinations with k ones among n registers [75]. Thus, the formal description of the algorithm is as follows:

Step 1. Select an arbitrary combination of non-uniform binomial coding.

Step 2. If the code combination ends with the number 1, then zeros are inserted into all registers up to the right end (register n), which is considered auxiliary. The resulting combination ending in 0 will be a combination with constant weight.

Step 3. If the code combination ends with the number 0, then set ones (units) in all registers to the right end (register n or auxiliary register). Thus, a created combination ending in 1 will be a constant weight combination.

Step 4. Check that the combination thus obtained actually has a constant weight by counting the total number of units(s). If this number is equal to k, then the combination is indeed desirable. Select another non-uniform binomial coding combination and go to step 2. If all non-uniform binomial coding combinations are already selected, then STOP: all constant weight combinations of that range are generated.

2.4. Asymmetric non-Hermitian ENZ-containing layered structures for advanced optical devices and systems

Asymmetric non-Hermitian epsilon-near-zero-containing layered structures are a type of composite materials that exhibit unique optical properties due to their specific design and composition. These structures are characterized by having layers with different permittivity values, where at least one layer contains an ENZ material [76,] [77].

One of the key advantages of asymmetric non-Hermitian ENZ-containing layered structures is their ability to control light propagation in unconventional ways. For example, these structures can exhibit unidirectional light propagation, where light waves only travel in one direction while being completely blocked in the opposite direction. This property is particularly [78–80] useful for designing optical isolators and circulators, which are essential components in optical communication systems to prevent signal interference and ensure signal integrity [81–83].

Moreover, the non-reciprocal nature of these structures enables the realization of topologically protected photonic states, where light waves are immune to backscattering or disorder-induced losses [84], [85]. This feature is crucial for developing robust photonic devices that are resilient to external perturbations and imperfections.

Asymmetric non-Hermitian ENZ-containing layered structures also offer opportunities for enhancing light-matter interactions and enabling efficient light confinement and manipulation at the nanoscale. These structures can be tailored to support surface plasmon polaritons[86], surface waves, or other exotic modes that can be utilized for sensing applications, subwavelength imaging, and energy harvesting [87–89].

Furthermore, the tunable optical properties of these structures make them promising candidates for developing reconfigurable and adaptive optical devices. By adjusting the parameters of the layers or introducing external stimuli, such as electric or magnetic fields, the

optical response of the structure can be dynamically controlled, opening up possibilities for on-demand modulation of light transmission, reflection, and absorption [**90**], [**91**].

Overall, asymmetric non-Hermitian ENZ-containing layered structures represent a rich platform for exploring novel optical phenomena and designing next-generation photonic devices with enhanced functionalities and performance characteristics. Continued research in this field is expected to lead to exciting advancements in photonics, metamaterials, and optoelectronics. **<u>Therefore, it will provide a new level of telecommunication solutions!</u>**

ENZ materials have a permittivity value close to zero at a certain frequency range, leading to interesting optical phenomena such as enhanced light-matter interactions, extreme wave manipulation, and tunable optical properties. **By incorporating ENZ materials into layered structures, novel optical devices with unconventional functionalities could be engineered!**

The asymmetry in the structure refers to the non-reciprocal nature of the material, meaning that its response to light propagation is different depending on the direction of the incident light. This asymmetry can be achieved through various means, such as introducing gain or loss in the structure, breaking time-reversal symmetry, or utilizing nonlinear effects [**92**], [**93**].

These asymmetric non-Hermitian ENZ-containing layered structures have attracted significant interest in the field of photonics and metamaterials due to their potential applications in areas such as waveguiding, sensing, cloaking, and nonlinear optics. **Explore and optimization of those structures to harness their unique optical properties for advanced optical devices and systems**.

CHAPTER 3: MAIN RESULTS

3.1. High-reliability network

The network can be in three modes:
- o in phasing mode (clock synchronization);
- o in the mode of polling databases in the "P" mode by a unit in the "C" mode and assigning access intervals;
- o in data transfer mode.
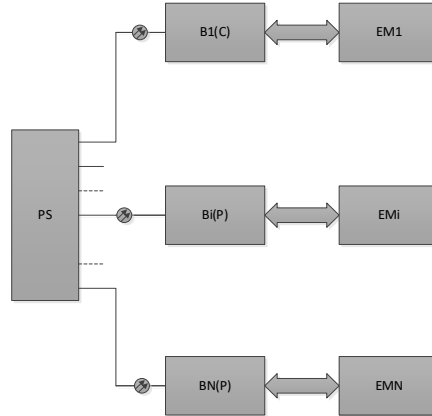
Fig. 3.1. Considered organization of the local network. PS – passive splitter; B, Bi, BN – access devices; EM - electronic module.

Figure 3.1 shows the variant of local network organization based on the proposed protocol 3. In this figure, the access device B1 is in the "C" mode, and the access devices Bi ÷ BN are in the "P" mode. All Bs are connected by optical lines to the passive optical splitter (PS) and are connected through interfaces, each with its electronic module (EM). Thus, the optical signal is branched between all Bs, and a passive bus optical mono channel is created (where all access units "hear" everyone). The network can be in three modes:
1. in phasing mode (clock synchronization);
2. in the polling mode, the T base stations in the "P" mode are polled by the B in the "C" mode and assign access intervals;
3. in data transfer mode.

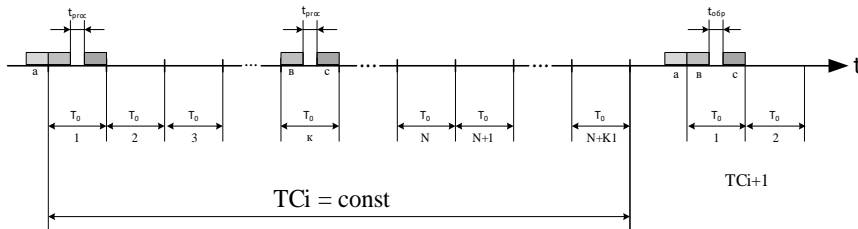**Fig. 3.2.** The protocol time chart: a – the phasing interval; b – polling cycle; c – window assignment cycle; t_{proc} – query processing interval by the analyzer; T_0 - the transmission window interval; TCi – i-th transmission cycle; TCi+1 – next i+1 transmission cycle (beginning).

The integration of fiber optic access networks and optical sensors offers a powerful solution for building highly reliable and efficient communication systems. By leveraging the advantages of fiber optic technology, such as high bandwidth, low latency, and immunity to electromagnetic interference, these networks provide a robust infrastructure for transmitting data over long distances with minimal signal degradation.

By combining fiber-optic access means with optical sensors, operators can create a smart network that delivers high-speed connectivity and ensures continuous operation, resilience to disruptions, and improved overall system performance. **This integrated approach paves the way for the development of advanced applications in diverse fields, including telecommunications, smart cities, industrial automation, and environmental monitoring**.

The development and testing of this new approach for ensuring the transmission of traffic from subscribers of the on-board network represents a significant advancement in the field of communication technology. By implementing innovative solutions and leveraging cutting-edge techniques, this approach has demonstrated its ability to enhance onboard networks' reliability, efficiency, and performance.

The successful integration of this new approach not only addresses the challenges associated with transmitting traffic from subscribers but also opens up new possibilities for optimizing network operations, improving user experience, and enabling the seamless delivery of services [**94**], [**95**]. Through rigorous testing and validation, the effectiveness and robustness of this approach have been confirmed, paving the way for its adoption in real-world scenarios.
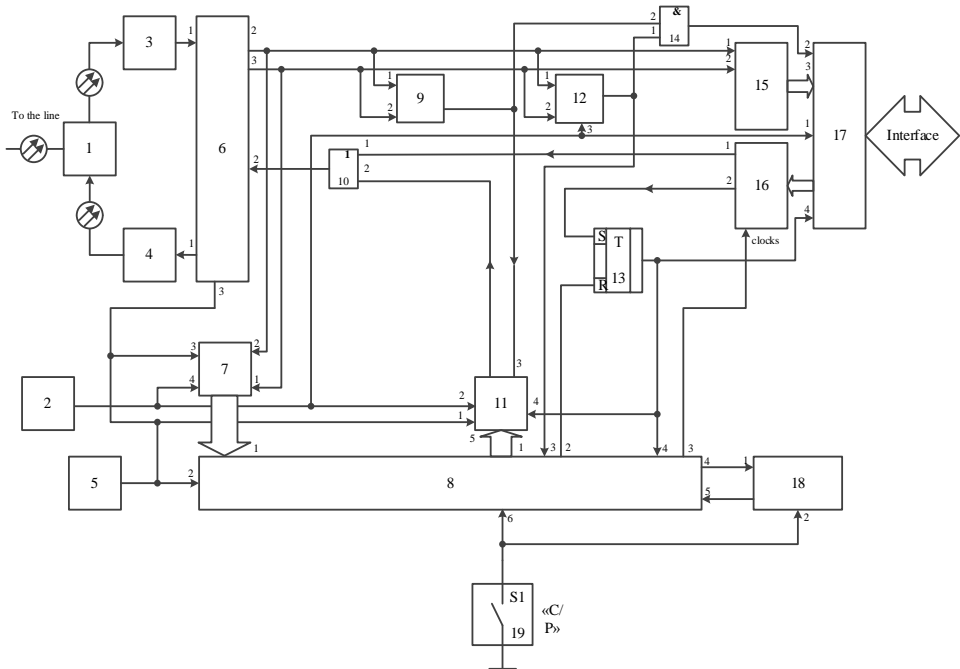
3.2. High-reliability network components

Fig. 3.3. Local network access block with guaranteed message delivery.

Figure 3.3 shows a possible implementation of a local network access block with guaranteed message delivery, where: 1 - separating device; 2 - address setter; 3 - optical receiver; 4 - optical transmitter; 5 - reference generator; 6 - linear encoder/decoder; 7 - command receiver; 8 - synchronization and control unit; 9 - error detector; 10 – "OR" circuit; 11 - command transmitter; 12 - frame selector; 13 – "ready" trigger; 14 - "AND" circuit; 15 - receive RAM; 16 - transmission RAM; 17 - interface block; 18 – analyzer; 19 - switch S1 "C/P".

The development and implementation of a local network access block with guaranteed message delivery for aircraft represents a critical advancement in aviation communication technology. **By introducing a robust and reliable solution to manage network access and ensure the transmission of messages, this approach enhances the safety, efficiency, and performance of communication systems on board aircraft.**

Through rigorous testing and validation, the effectiveness and reliability of this solution have been demonstrated, providing assurance that critical messages can be delivered promptly and securely within the aircraft's local network. This capability is essential for maintaining seamless communication among crew members, passengers, and ground control, thereby enhancing situational awareness and operational efficiency during flights [**96**].

The successful deployment of this local network access block with guaranteed message delivery not only addresses the challenges associated with managing network traffic on aircraft but also **sets a new standard for connectivity and communication in the aviation industry**! By leveraging innovative technologies and best practices, organizations can optimize network operations, improve data transmission, and ensure the timely delivery of critical information in a highly dynamic and demanding environment.

The continued development and utilization of this solution hold immense potential for transforming communication systems on aircraft, enabling enhanced connectivity, real-time data exchange, and improved collaboration among stakeholders. By embracing this innovative approach, aviation industry stakeholders can unlock new opportunities for enhancing safety, efficiency, and passenger experience, ushering in a new era of connectivity and innovation in air travel.

In summary, the development and use of a local network access block with guaranteed message delivery for aircraft represent a significant milestone in advancing aviation communication technology, paving the way for enhanced communication capabilities and improved operational performance in the skies.

3.3. Optical sensors for aircraft applications

Fig. 3.4. 3D model of the developed pressure sensor.

The proposed design of the aerometric pressure sensor is highly accurate in determining the deformation (the value of which is reduced to a minimum) of the elastic sensing element and high speed. The high performance of the measuring system will in the future, make it possible to use algorithms that take into account and compensate for various types of destabilizing factors (interference, vibrations, shock effects, etc.) that arise during the operation of aircraft.

The low power consumption, dimensions, and weight of the proposed design make it possible to use the sensor as part of integrated systems of aircraft backup devices.

Considering the general trend in the development of unmanned aerial vehicles (UAVs) with an electric power plant, the use of pressure sensors based on lines of photoelectronic elements to determine altitude and speed parameters will increase energy survivability and reduce the overall dimensions and weight of the UAV.

The successful development of a pressure sensor based on a deformable CuBe2Ni(Co) bronze membrane of a sinusoidal profile with a rigid center, an LED with a wavelength of 625 nm, a charged coupled device (CCD) matrix with a Photo response non-uniformity of 5 %, and a pixel size of 14 μm represents a significant advancement in sensor technology. This innovative sensor design offers a range of benefits that can significantly enhance pressure measurement systems' accuracy, efficiency, and performance.

This pressure sensor can effectively measure membrane shift with precision and reliability by utilizing a deformable membrane with a unique sinusoidal profile and a rigid center. Integrating an LED with a specific wavelength and a CCD matrix with high photo response uniformity and small pixel size further enhances the sensor's ability to capture and analyze data accurately.

One of the key advantages of this pressure sensor is its ability to increase measurement accuracy for both absolute and static pressure sensors by at least 50 %. This improvement in accuracy is crucial for applications where precise pressure measurements are essential for safety, performance, and regulatory compliance.

Moreover, the development of this sensor also leads to a significant reduction in energy consumption by no less than 70 %. This reduction in energy usage contributes to cost savings and promotes sustainability by minimizing the environmental impact of sensor operations.

In addition, the innovative design of this pressure sensor enables a reduction in the time required to maintain order and the weight of the final sensor by no less than 25 % compared to traditional frequency absolute and static pressure sensors. Streamlining of sensor maintenance and weight reduction can positively impact overall system efficiency and performance.

Overall, **the successful development of this pressure sensor represents a significant breakthrough in sensor technology, offering improved accuracy, energy efficiency, and weight reduction compared to existing pressure sensor solutions**. By leveraging this innovative sensor design's unique features and capabilities, industries and applications requiring precise pressure measurements can benefit from enhanced performance, reliability, and cost-effectiveness.

Table 3.1

The Main Characteristics of the Developed Pressure Sensor

Parameter	Prototype (used in Honeywell AirDC)	Prospective pressure sensor	Efficiency increase, %
Data transmission interval, s	0.31	0.25	19
Reduced supply voltage, V	15	3.3	78
Reduced energy consumption, mW	1000	280.708	72
Measurement error, Pa	32	13.14	59
Reception time, s	30	1	96
Weight loss, g	400	213	46.75

3.4. Theory of asymmetric non-Hermitian ENZ-containing layered structures

An example of non-Hermitian asymmetry at various angles is shown in Fig. 3.5. Let us take two angles: the first angle $\theta = 22.7°$ below 0, "bound states in the continuum" (BIC), and the second angle $\theta = 25.0°$ above it. The position of the resonant frequency shifts to the values of $\omega = 0.999\,\omega$ and $\omega = 1.001\,\omega$, respectively. The pole condition $\text{Re}M_{11}\,\theta$ is achieved at $\beta_0 = 1.03263$ (Fig. 3.5 (a)) and $\beta_0 = 1.03$ (Fig. 3.5 (c)), and the zero condition ($\text{Re}M_{12} \ll 1$) at these b 0.

The phenomenon of coherent perfect absorption (CPA) is a fascinating area of study in optics and photonics, where the complete absorption of incident light waves is achieved through interference effects. In the context of the case under consideration, it is noted that the conditions for CPA generation are not fully met, indicating an incomplete state of CPA. Despite

this partial fulfilment, an intriguing observation emerges – a notable enhancement of reflection occurs near the critical parameter β_0.

This enhancement in reflection, as depicted in Fig. 3.5 (b) and (d), showcases the significant impact of the incomplete condition of CPA generation on the behavior of light waves interacting with the system. The strong reflection observed near β_0 highlights the intricate interplay between the incident light waves, the material properties, and the specific conditions present in the system.

The results presented in these figures underscore the complex and nuanced nature of optical phenomena, where even partial adherence to certain conditions can lead to pronounced effects and outcomes. This enhancement of reflection near β_0 serves as a compelling illustration of the intricate dynamics at play in the interaction between light and matter, prompting further exploration and analysis to unravel the underlying mechanisms driving this phenomenon.

The study's gain analysis further solidifies the effect's precise nature at various frequencies and underscores its robustness against parameter variations. The findings demonstrate that the effect remains consistent and reliable across different frequency ranges, reaffirming its inherent characteristics. Moreover, the resistance of the effect to parameter changes highlights its stability and resilience, indicating that it can maintain its properties even under varying conditions. Overall, the examination of gain provides additional evidence of the effect's exact nature and ability to withstand alterations, further enhancing our understanding of this phenomenon.
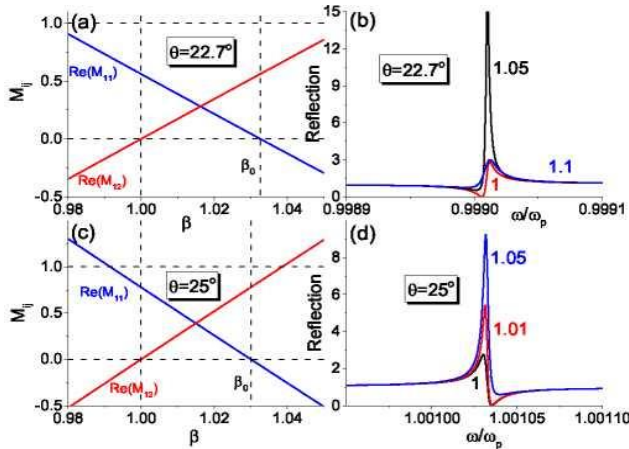
Fig. 3.5. (a), (c) – Dependence of transfer matrix elements on the asymmetry parameter b at angles of incidence $\theta = 22.7°$ (at frequency $\omega = 0.999\ \omega$) and $\theta = 25.0°$ (at frequency $\omega = 1.001\ \omega$); (b), (d) – the corresponding reflection spectra for various parameters of non-Hermitian asymmetry b, marked with numbers next to the curves. The amount of loss $\gamma + = 0.001$.

Nevertheless, the case of plasma frequency [**96**] can be distinguished for two reasons. The case of plasma frequency [**89**] stands out for two distinct reasons. Firstly, a notable asymmetry is observed in the profiles of the Fano spectra depicted in Figure 3.5, setting them apart from the symmetrical profiles seen in Figure 3.5. This asymmetry indicates a deviation from the expected uniformity or balance in the spectral data, suggesting underlying complexities or

unique characteristics in the system under study. The pronounced asymmetry in the plasma frequency case signals a departure from conventional patterns, prompting further investigation into the factors driving this distinctive behavior. This deviation in spectral profiles hints at potentially novel insights or phenomena at play, warranting a closer examination to unravel the underlying mechanisms and implications of this intriguing observation. Secondly, another striking feature of this case is the observation that $\beta_0 > 1$ is both below and above θBIC. This finding contradicts the conventional expectation of $\beta_0 < 1$ at the angle of incidence $\theta = \theta BIC$. The fact that β_0 exceeds 1 in these instances, contrary to the anticipated behavior at θBIC, highlights a counterintuitive aspect of the plasma frequency case. This unexpected discrepancy raises questions about the underlying mechanisms driving this unusual behavior and underscores the need for further investigation to elucidate the implications and significance of this contradiction. Such counterintuitive results challenge existing assumptions and call for a deeper understanding of the complex dynamics at play in this particular scenario. These facts confirm the specificity and unusualness of the response close to BIC at the plasma frequency.

3.5. Aircraft optical video transmission communication based on the forward error correction codes
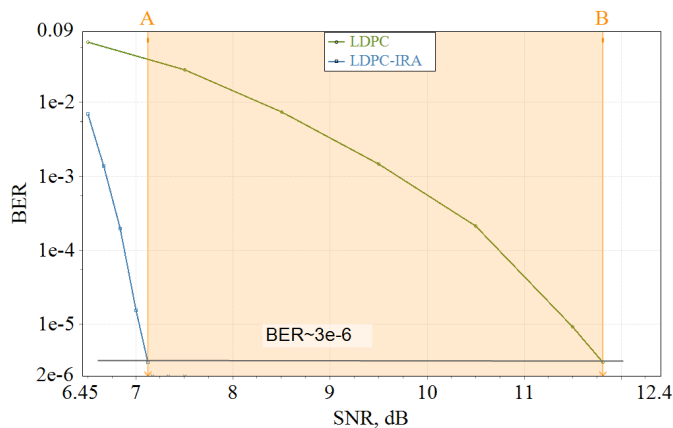
Fig. 3.6. Bit error ratio (BER) versus Signal-noise ratio (SNR) for LDPC and LDPC-IRA.

LDPC-IRA's superior performance is attributed to its ability to effectively mitigate errors in the transmission process, especially in the presence of noise and interference. By combining LDPC codes with iterative decoding techniques, LDPC-IRA can achieve remarkable error correction capabilities while maintaining low latency and high throughput.

The simulation results clearly demonstrate that LDPC-IRA outperforms traditional LDPC coding in terms of BER at various SNR levels. This significant improvement in error correction efficiency translates to enhanced reliability and robustness in data transmission, making LDPC-IRA a valuable solution for mission-critical applications such as ARINC-818 communication systems.

Overall, the adoption of LDPC-IRA coding in ARINC-818 systems promises to revolutionize the way data is transmitted and received, offering a more resilient and efficient communication framework that can withstand challenging operating conditions and ensure

seamless connectivity in aerospace and defense environments.

According to the simulation results, we obtained a significant advantage of LDPC-IRA over LDPC. Modeling on 16-QPAM modulation shows that LDPC-IRA provides a BER of 2×10^{-6} at SNR 7.2 dB. The addition of LDPC-IRA coding to ARINC-818 improves transmission efficiency more than three times. Within problem-solving, this makes it possible to increase the system's stability under the influence of HIRF.

This improvement in efficiency plays a crucial role in problem-solving scenarios, particularly in enhancing the system's stability against High-Intensity Radiated Fields HIRF. By leveraging the benefits of LDPC-IRA, the system can better withstand external interference and ensure reliable communication. This breakthrough underscores the importance of advanced coding techniques in optimizing system performance and resilience in challenging environments.

Figure 3.7 shows BER versus normalized Generalized mutual information (GMI) for LDPC and LDPC-IRA FEC codes.
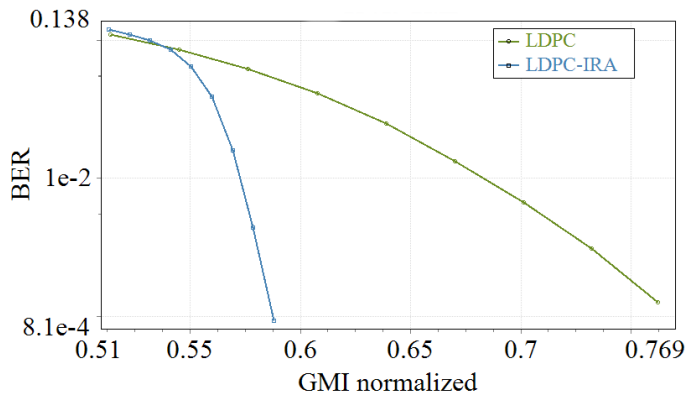
Fig. 3.7. Bit error ratio (BER) vs normalized Generalized mutual information (GMI) for LDPC and LDPC-IRA.

The integration of LDPC-IRA coding into the system under consideration represents a significant advancement in data transmission efficiency, particularly evident in scenarios such as video transmission. By leveraging the advanced error correction capabilities of LDPC-IRA, the dispersion of information is substantially reduced, resulting in a more reliable and seamless communication process.

In practical terms, implementing LDPC-IRA in the system can reduce information dispersion by more than 1.3 times compared to traditional coding methods. This means that even when working with challenging initial data conditions, such as high noise or interference levels, LDPC-IRA can effectively mitigate errors and ensure the accurate and timely delivery of information.

The enhanced error correction performance of LDPC-IRA not only improves the quality and reliability of video transmission but also contributes to overall system efficiency by minimizing retransmissions and latency issues. As a result, users can experience smoother and more consistent data delivery, making LDPC-IRA a valuable asset for applications where data integrity and timeliness are critical, such as in aerospace, defense, and multimedia

communications.

Additionally, the integration of LDPC-IRA coding can also lead to improved spectral efficiency, allowing for higher data rates within the same bandwidth. This is particularly beneficial in scenarios where spectrum resources are limited or expensive, as LDPC-IRA can help maximize the utilization of available bandwidth while maintaining robust error correction capabilities.

Furthermore, LDPC-IRA coding is known for its flexibility and adaptability to different communication environments. Its iterative decoding process allows for efficient error correction even in challenging conditions, such as fading channels or varying signal-to-noise ratios. This adaptability makes LDPC-IRA well-suited for dynamic and unpredictable communication scenarios where traditional coding schemes may struggle to maintain performance.

Overall, the integration of LDPC-IRA coding into the system not only enhances data transmission efficiency and reliability but also opens up new possibilities for high-performance communication systems in a wide range of applications. Its combination of advanced error correction capabilities, spectral efficiency, and adaptability make LDPC-IRA a powerful tool for improving data transmission quality and system performance in demanding communication environments.

LDPC-IRA in the system under consideration will reduce the dispersion of information when working with certain initial data, for example, during video transmission, by more than 1.3 times.

CHAPTER 4: FINAL REMARKS

Analysis of trends in the development of onboard information and telecommunication networks and sensors in conditions of high-intensity electromagnetic fields made it possible to establish that today, there is an urgent need for significant improvements in the resistance of information networks to high-intensity electromagnetic fields.

As a result of the analysis, of means of increasing resistance, methods for organizing networks and noise-resistant coding were identified, and sensors onboard aircraft were considered. Systemic methodological problems and contradictions were identified in building networks, organizing coding, and using pressure sensors.

The analysis of existing scientific works in this area of research showed that in order to build a secure network with guaranteed message delivery under conditions of increased electromagnetic load, modernization of the scientific and methodological apparatus used is required. For these purposes, the prospects for the application of mainline noise-resistant coding methods and the application of optical sensors to a new area of research are substantiated. This will allow us to solve methodological problems caused by the impact of electromagnetic fields on the onboard information and telecommunications network.

The disadvantages of existing networks include the use of fiber channel cables, which have high weight and relatively low throughput, low resistance of transceivers to the effects of fields, as well as high susceptibility of electronic static and total pressure sensors to the effects of EMV.

The hypothesis of the research is formulated, according to which the use of fiber optics as the main line for data transmission with hybrid noise-resistant coding, as well as the use of optical sensors for measuring static and total pressure, will significantly increase the resistance of the system to electromagnetic radiation, reduce the weight of transmitting and receiving devices and ensure flight safety.

The Thesis incorporates three interlinked models that are designed to facilitate the research process and assess the validity of the hypothesis. These interconnected models serve as a comprehensive foundation for conducting a thorough and systematic study in accordance with the specified scientific objective.

Based on mathematical modelling, the simulation model of the information and telecommunications network allows the onboard network processes to estimate the network's delays and jitter under the influence of electromagnetic interference. The developed methodology ensures reliable reproduction of the behavior of a service network using the example of an optical access network based on passive optical networks.

The methodology for developing optical pressure sensors for the information and telecommunications network of aircraft makes it possible to design a more resistant electromagnetic interference sensor of static and total pressure. A distinctive feature of this technique is the use of optical methods for collecting information.

The method of optimal noise-resistant coding for aircraft onboard computer networks based on noise-resistant direct correction LDPC codes increases line resistance to interference.

The mechanism developed in the dissertation allows for further development and application to a new field of research in the construction of fiber optic broadband networks for use on aircraft.

4.1. Main conclusions

1. The organization of a fiber optic access network is proposed. Each end node of the proposed network monopolizes the entire channel resource of the bandwidth of the channel allocated at its wavelength, which significantly improves the quality-of-service (QoS) indicators for traffic in the proposed network. The proposed network achieves doubling the capacity (the number of connected nodes) compared to the use of traditional wave multiplex technologies. The proposed passive network provides complete logical transparency in dedicated channels and does not require any additional headers to be attached to packets (frames) of information, such as in GPON. In addition, there is no dependence on throughput at the node level on the number of nodes included in the network segment or on the variation in the lengths of subscriber lines. An optical network access unit is proposed. The use of the proposed access block makes it possible to organize the guaranteed transmission of information frames at the access network level due to the implementation of a synchronous conflict-free access method with frame acknowledgement at the access level. The use of an access protocol with load polling and assignment of access intervals in the proposed access blocks will ensure, in addition to guaranteed delivery of messages, also a low delay in their transmission, which will increase proportionally as the network load increases, but even at maximum load, the delay at the access level will not exceed the interval time equal to the full cycle of polling and transmission. The use of an access protocol with guaranteed message delivery will allow the proposed access block to be used in real-time networks, which is especially important when building control systems and distributed real-time computing systems. The use of a physical propagation medium based on optical fiber in the network makes it possible to ensure high noise immunity under conditions of exposure to powerful electromagnetic fields, and also significantly complicates the interception of information through spurious electromagnetic radiation and interference, which will ensure high noise immunity and protection of information in a local network built on the basis of the proposed access units, and the complete electrical isolation of the terminals created will create additional noise immunity due to the absence of "stray" currents.

These advantages are especially important when building object systems saturated with radio-electronic equipment (REE), such as radio stations, radar stations (RLS) and others, where, in addition, protection of transmitted information is required, as well as the absence of susceptibility of network equipment to lightning discharges.

2. The simulation results highlight a notable advantage of LDPC-IRA (low-density Parity-check with irregular repeat-accumulate) coding over traditional LDPC coding schemes. Through modeling using 16-QPAM modulation, it was observed that LDPC-IRA offers a superior bit error rate (BER) performance, achieving a BER of 2×10^{-6} at a signal-to-noise ratio (SNR) of 7.2 dB. This signifies a substantial improvement in error correction capabilities compared to standard LDPC coding techniques.

Furthermore, the integration of LDPC-IRA coding into the ARINC-818 communication protocol demonstrates a significant enhancement in transmission efficiency, surpassing traditional methods by more than threefold. This advancement in coding efficiency plays a crucial role in addressing challenges related to high-intensity radiated fields (HIRF) interference, thereby bolstering the overall stability and reliability of the system.

By leveraging the benefits of LDPC-IRA coding within the context of ARINC-818 communication systems, the solution not only improves data transmission performance but also fortifies the system's resilience against external electromagnetic disturbances. This breakthrough underscores the potential of LDPC-IRA as a key enabler for enhancing communication systems' robustness and effectiveness in demanding operational environments.

Additionally, the simulation results illustrate that **LDPC-IRA coding offers a more efficient bandwidth utilisation than traditional LDPC codes**. This increased spectral efficiency is crucial in aerospace and avionics applications where bandwidth is often limited and costly. By achieving a lower BER at a given SNR, LDPC-IRA coding enables more reliable data transmission with fewer errors, ultimately leading to improved system performance and reduced retransmission rates.

Moreover, the **robust error correction capabilities of LDPC-IRA coding make it well-suited for high-speed data communication systems, such as those used in aircraft avionics and aerospace applications**. The ability of LDPC-IRA to effectively correct errors in noisy and interference-prone environments enhances the overall reliability and integrity of data transmission, ensuring critical information is accurately conveyed without loss or corruption.

Overall, **the integration of LDPC-IRA coding into ARINC-818 communication systems represents a significant advancement in aerospace communication technology**. By leveraging the superior error correction performance and spectral efficiency of LDPC-IRA, aerospace and avionics systems can achieve higher data transmission reliability, improved signal quality, and enhanced resilience to external interference, ultimately enhancing airborne communication systems' safety, efficiency, and performance.

3. This research introduces a novel concept of coherent perfect absorber (CPA) generation linked to quasi-bound states in the continuum (BIC) discovered in asymmetric non-Hermitian layered structures containing exceptional points of non-conservation (ENC). The asymmetry present in these structures plays a crucial role in the evolution of quasi-BIC resonance into CPA lasing resonance. Delved into cases involving varying thicknesses of loss and gain layers (geometric asymmetry) as well as unequal levels of losses and gains (non-Hermitian asymmetry), a detailed analysis has been conducted of the effects of asymmetry through the examination of poles and zeros of the scattering matrix, uncovering intriguing characteristics.

Of particular note is the identification of the point at which the pole and zero of CPA generation merge, leading to a significant increase in outgoing intensity and a sharp rise in the quality factor associated with the adjacent quasi-BIC. Two key results have emerged from the study. Firstly, an unusual inverse linear relationship between the quality factor and the asymmetry parameter has been observed. Secondly, in systems exhibiting non-Hermitian asymmetry, a counterintuitive amplification due to losses has been detected at the plasma frequency.

It is believed that the findings presented in this work hold broad significance for the field of non-Hermitian photonics and have the potential for extension to 2D and 3D systems. The anticipated demand for the CPA generation effect linked to quasi-BIC in laser and nonlinear optical applications underscores the practical implications of this research. Further investigation into the interplay between asymmetry, quasi-BIC resonances, and CPA generation in non-Hermitian structures could lead to the d**evelopment of advanced photonic devices with enhanced performance characteristics**. By exploring different configurations

and tuning parameters, researchers may uncover novel ways to control light-matter interactions, manipulate wave propagation, and design efficient optical components.

Additionally, the discovery of the counterintuitive amplification effect due to losses at the plasma frequency in systems with non-Hermitian asymmetry opens new avenues for exploring unconventional optical phenomena and harnessing them for practical applications. Understanding and exploiting such unique behaviors could lead to the development of innovative devices for sensing, communication, and signal processing.

Overall, the insights gained from this research have the potential to inspire further studies in non-Hermitian photonics, offering new perspectives on how asymmetry can be leveraged to achieve desired optical functionalities. **By pushing the boundaries of current knowledge and exploring the rich landscape of non-Hermitian systems, researchers may unlock new opportunities for advancing photonics technology and addressing challenges in various domains**.

4. The development of a new pressure sensor intended for use in Honeywell AirDC systems has resulted in significant improvements across various key parameters compared to the prototype sensor currently in use. The prospective **pressure sensor demonstrates enhanced performance and efficiency gains in several critical aspects**:

4.1. ***Data transmission interval:*** The new sensor boasts a reduced data transmission interval of 0.25 seconds, representing a notable 19 % increase in efficiency over the existing prototype.

4.2. ***Reduced supply voltage:*** A substantial improvement is seen in the supply voltage requirement, with the prospective sensor operating at just 3.3 V compared to the 15 V needed by the prototype. This reduction of 78 % in supply voltage contributes to enhanced energy efficiency and overall system performance.

4.3. ***Reduced energy consumption:*** The prospective sensor achieves a significant decrease in energy consumption, consuming only 280.708 mW as opposed to the 1000 mW drawn by the prototype. This reduction of 72 % in energy consumption underscores the sensor's improved efficiency and sustainability.

4.4. ***Measurement error:*** The new sensor demonstrates a lower measurement error of 13.14 Pa, representing a 59 % improvement over the 32 Pa error associated with the prototype. This enhanced accuracy ensures more reliable and precise pressure readings.

4.5. ***Reception time:*** A substantial enhancement is observed in the reception time of the prospective sensor, with a swift response time of just one second compared to the 30-second reception time of the prototype. This remarkable 96 % reduction in reception time enhances real-time data processing capabilities and system responsiveness.

4.6. ***Weight loss:*** The prospective sensor also exhibits a reduction in weight, weighing only 213 g as opposed to the 400 g weight of the prototype. This weight loss of 46.75 % contributes to improved portability and ease of installation.

Overall, the **development of the prospective pressure sensor represents a significant advancement in pressure sensing technology. It offers increased efficiency, accuracy, energy savings, and reduced size and weight**. These improvements pave the way for enhanced performance and functionality in air pressure monitoring applications within Honeywell AirDC systems.

4.2. Further outlook

The culmination of research and development efforts to enhance the scientific and methodological apparatus and the practical tools has led to a significant milestone in addressing the scientific problem at hand. Through these endeavours, it can be inferred that the dissertation's primary objective has been successfully accomplished. The results obtained from these endeavours serve as a testament to the efficacy of the strategies employed in tackling the research challenges and achieving the desired outcomes.

There are several promising avenues for further exploration and advancement in the field. One such direction involves the continued refinement and innovation in the development of fiber pressure sensors. These sensors are crucial in various applications, including industrial monitoring, medical diagnostics, and environmental sensing. By enhancing fibre pressure sensors' sensitivity, accuracy, and reliability, researchers can unlock new possibilities for monitoring and control systems across diverse domains.

Another area ripe for future investigation pertains to the methods for constructing fiber optic access networks. As the demand for high-speed and reliable communication networks continues to grow, there is a pressing need to optimize the design, deployment, and management of fiber optic infrastructure. By exploring novel techniques and strategies for building efficient and scalable fiber optic access networks, researchers can enhance connectivity, bandwidth, and network performance in urban and rural settings.

Furthermore, the development of noise-resistant coding methods represents a critical frontier in ensuring the integrity and security of data transmission over fiber optic channels. With the proliferation of digital communication systems and the increasing susceptibility to external interference and noise sources, there is a growing imperative to devise robust and resilient coding schemes that can mitigate errors and enhance signal quality. By exploring innovative approaches to noise-resistant coding, researchers can bolster the reliability and efficiency of data transmission in fiber optic networks.

In conclusion, while the successful resolution of the scientific problem and the achievement of the dissertation's goal marks a significant milestone, there are ample opportunities for further research and innovation in the field. By focusing on areas such as fiber pressure sensors, fiber optic access networks, and noise-resistant coding methods, researchers can continue pushing the boundaries of knowledge and technology in advancing the fiber optics and communication systems.

BIBLIOGRAPHY

1. Rey Charlo, R. E. (2024). On-board radio communication and its development in a historical perspective. International Journal of Maritime History, 36(1), 140-152. https://doi.org/10.1177/08438714231202163

2. Ramanatt, P.R., Natarajan, K. and Shobha, K.R. (2018), "Challenges in implementing a wireless avionics network", Aircraft Engineering and Aerospace Technology, Vol. 92 No. 3, pp. 482-494. https://doi.org/10.1108/AEAT-07-2019-0144

3. M. Cenk Ertürk, N. Hosseini, H. Jamal, A. Şahin, D. Matolak and J. Haque, "Requirements And Technologies Towards Uam: Communication, Navigation, And Surveillance," 2020 Integrated Communications Navigation and Surveillance Conference (ICNS), Herndon, VA, USA, 2020, pp. 2C2-1-2C2-15, doi: 10.1109/ICNS50378.2020.9223003.

4. D. Liu, J. Cui, J. Zhang, C. Yang and L. Hanzo, "Deep Reinforcement Learning Aided Packet-Routing for Aeronautical Ad-Hoc Networks Formed by Passenger Planes," in *IEEE Transactions on Vehicular Technology*, vol. 70, no. 5, pp. 5166-5171, May 2021, doi: 10.1109/TVT.2021

5. Dashkiiev, V.; Povstenko, Y. Advanced Architecture of On-Board Multiplex Information Exchange System to Increase Flight Safety. Entropy 2022, 24, 1582. https://doi.org/10.3390/e24111582

6. Sekera, Jakub, Novak, Andrej. (2021). The future of data communication in Aviation 4.0 environment. INCAS BULLETIN. 13. 165-178. 10.13111/2066-8201.2021.13.3.14..3074015.

7. Ian Moir , Allan Seabridge and Malcolm Jukes, Civil Avionics Systems, Second Edition, ISBN (print): 978-1-62410-228 Publication Date: September 25, 2013

8. Bieber, Pierre & Boniol, Frédééric & Boyer, Marc & Noulard, Eric & Pagetti, Claire. (2012). New Challenges for Future Avionic Architectures. Aeropsacelab Journal. 04.

9. D. He, S. Chan and M. Guizani, "Communication Security of Unmanned Aerial Vehicles," in IEEE Wireless Communications, vol. 24, no. 4, pp. 134-139, Aug. 2017, doi: 10.1109/MWC.2016.1600073WC.

10. L. Jianwei, L. Weiran, W. Qianhong, L. Dawei and C. Shigang, "Survey on Key Security Technologies for Space Information Networks," in Journal of Communications and Information Networks, vol. 1, no. 1, pp. 72-85, June 2016, doi: 10.11959/j.issn.2096-1081.2016.006.

11. Maxim Solkin, Electromagnetic interference hazards in flight and the 5G mobile phone: Review of critical issues in aviation security, Transportation Research Procedia, Volume 59, 2021, Pages 310-318, ISSN 2352-1465, https://doi.org/10.1016/j.trpro.2021.11.123

12. Zatuchny, D.A., Negreskul, G.G., Sauta, O.I., Shatrakov, A.Y., Shatrakov, Y.G. (2022). Methods for Evaluating the Electromagnetic Compatibility of Integrated Ground Systems and On-Board Systems. In: Aerospace Radionavigation Systems. Springer Aerospace Technology. Springer, Singapore. https://doi.org/10.1007/978-981-19-6341-4_1

13. A. Maouloud, M. Klingler and P. Besnier, "A Test Setup to Assess the Impact of EMI Produced by On-Board Electronics on the Quality of Radio Reception in Vehicles," in IEEE Transactions on Electromagnetic Compatibility, vol. 63, no. 6, pp. 1844-1855, Dec. 2021, doi: 10.1109/TEMC.2021.3072558.

14. Jr, E.R. & Daughtry, Craig & Walthall, Charlie & III, J.E. & Dulaney, Wayne. (2003). Agricultural Remote Sensing using Radio-Controlled Model Aircraft. 197-205. 10.2134/asaspecpub66.c15.

15. Kerczewski, Bob. (2013). Spectrum for UAS control and Non-Payload Communications. 1-21. 10.1109/ICNSurv.2013.6548666.

16. Nicola, M.; Falco, G.; Morales Ferre, R.; Lohan, E.-S.; de la Fuente, A.; Falletti, E. Collaborative Solutions for Interference Management in GNSS-Based Aircraft Navigation. Sensors 2020, 20, 4085. https://doi.org/10.3390/s20154085

17. Borgstrom, E., "An Overview of the EMC Requirements in RTCA/DO-160G," SAE Int. J. Aerosp. 5(2):300-310, 2012, https://doi.org/10.4271/2012-01-2147.

18. Serrano-Mira, L.; Pérez Maroto, M.; Ayra, E.S.; Pérez-Castán, J.A.; Liang-Cheng, S.Z.Y.; Gordo Arias, V.; Pérez-Sanz, L. Identification and Quantification of Contributing Factors to the Criticality of Aircraft Loss of Separation. Aerospace 2022, 9, 513. https://doi.org/10.3390/aerospace9090513

19. Osunwusi, A. O. (2020). Occupational Radiation Exposures in Aviation: Air Traffic Safety Systems Considerations. International Journal of Aviation, Aeronautics, and Aerospace, 7(2). DOI: https://doi.org/10.15394/ijaaa.2020.1476

20. Michałowska, J.; Pytka, J.; Tofil, A.; Krupski, P.; Puzio, Ł. Assessment of Training Aircraft Crew Exposure to Electromagnetic Fields Caused by Radio Navigation Devices. Energies 2021, 14, 254. https://doi.org/10.3390/en14010254

21. I. W. Damaj, J. K. Yousafzai and H. T. Mouftah, "Future Trends in Connected and Autonomous Vehicles: Enabling Communications and Processing Technologies," in IEEE Access, vol. 10, pp. 42334-42345, 2022, doi: 10.1109/ACCESS.2022.3168320.

22. A. Baltaci, E. Dinc, M. Ozger, A. Alabbasi, C. Cavdar and D. Schupke, "A Survey of Wireless Networks for Future Aerial Communications (FACOM)," in IEEE Communications Surveys & Tutorials, vol. 23, no. 4, pp. 2833-2884, Fourthquarter 2021, doi: 10.1109/COMST.2021.3103044.

23. Hamza Saadaoui, Alexandre Bacou, Yoann Rebiere, Bruno Fracasso, and Michel Morvan, "Broadband optical network design for the future aircraft cabin," Opt. Continuum 1, 719-737 (2022)

24. Alireza Behbahani, Mehrdad Pakmehr, William A. Stange, Optical Communications and Sensing for Avionics, Springer Handbook of Optical Networks, 2020, ISBN : 978-3-030-16249-8

25. Marques, C.; Leal-Júnior, A.; Kumar, S. Multifunctional Integration of Optical Fibers and Nanomaterials for Aircraft Systems. Materials 2023, 16, 1433. https://doi.org/10.3390/ma16041433

26. M. Z. Hasan, H. Al-Rizzo and F. Al-Turjman, "A Survey on Multipath Routing Protocols for QoS Assurances in Real-Time Wireless Multimedia Sensor Networks," in IEEE Communications Surveys & Tutorials, vol. 19, no. 3, pp. 1424-1456, thirdquarter 2017, doi: 10.1109/COMST.2017.2661201.

27. X. Wang and P. Yi, "Security Framework for Wireless Communications in Smart Distribution Grid," in IEEE Transactions on Smart Grid, vol. 2, no. 4, pp. 809-818, Dec. 2011, doi: 10.1109/TSG.2011.2167354.

28. Iasechko, Maksym & Gnusov, Yurii. (2019). Determination of Requirements for the Protection of Radio-Electronic Equipment from the Terroristic Influence by

Electromagnetic Radiation, International Journal of Emerging Trends in Engineering Research. 7. 772-777. 10.30534/ijeter/2019/077122019.

29. Michałowska, J.; Tofil, A.; Józwik, J.; Pytka, J.; Legutko, S.; Siemiątkowski, Z.; Łukaszewicz, A. Monitoring the Risk of the Electric Component Imposed on a Pilot During Light Aircraft Operations in a High-Frequency Electromagnetic Field. Sensors 2019, 19, 5537. https://doi.org/10.3390/s19245537

30. E. L. Portnov, K. Vyacheslav, I. Sergey and A. B. Semenov, "Cupper and fiber-optic cables in moving objects," 2018 Systems of Signals Generating and Processing in the Field of on Board Communications, Moscow, Russia, 2018, pp. 1-4, doi: 10.1109/SOSG.2018.8350626.

31. Khatimi, Husnul & Wijaya, Eka & Baskara, Andreyan & Sari, Yuslena. (2019). Performance Comparison Between Copper Cables and Fiber Optic in Data Transfer on Banjarmasin Weather Temperature Conditions. MATEC Web of Conferences. 280. 05022. 10.1051/matecconf/201928005022.

32. ITU-T Recommendation Y.1541 (12/11) Internet protocol aspects – Quality of service and network performance; Network performance objectives for IP-based services.

33. X. Wang and P. Yi, "Security Framework for Wireless Communications in Smart Distribution Grid," in IEEE Transactions on Smart Grid, vol. 2, no. 4, pp. 809-818, Dec. 2011, doi: 10.1109/TSG.2011.2167354.

34. Zouhaira, Abdellaoui & Dieudonne, Yiyi & Aleya, Anoir. (2021). Design, implementation and evaluation of a Fiber To The Home (FTTH) access network based on a Giga Passive Optical Network GPON. Array. 10. 100058. 10.1016/j.array.2021.100058.'

35. ITU-T Recommendation Y.1541 (12/11) Internet protocol aspects – Quality of service and network performance; Network performance objectives for IP-based services.

36. Cao, Xiaojing & Jin, Longxing & Huang, Fuquan & Liu, Zijun & Xiu, Rongkun. (2022). Application of Smart Grid Communication Service Flow Modeling Based on Poisson Model in Grid Operation. Journal of Cases on Information Technology. 24. 1-12. 10.4018/JCIT.302243.

37. X. Li, H. Yang, Q. Yao, B. Bao, J. Zhang and M. Cheriet, "Enhancing Time-Critical Communication for Industrial Applications with Deep Q-Network and Policy Reuse based TDM-PON," 2023 Opto-Electronics and Communications Conference (OECC), Shanghai, China, 2023, pp. 1-3, doi: 10.1109/OECC56963.2023.10209704.

38. Tsai, Eline & Demirtas, Derya & Tintu, Andrei & Jonge, Robert & Rijke, Yolanda & Boucherie, R.J.. (2023). Design of fork-join networks of First-In-First-Out and infinite-server queues applied to clinical chemistry laboratories. European Journal of Operational Research. 310. 10.1016/j.ejor.2023.04.003.

39. Zhang, Jian & Lee, Tony & Ye, Tong & Huang, Liang. (2019). An approximate mean queue length formula for queueing systems with varying service rate. Journal of Industrial and Management Optimization. 13. 10.3934/jimo.2019106.

40. Cocchi, R., Estrin, D., Shenker, S., & Zhang, L. (1991). A study of priority pricing in multiple service class networks. ACM SIGCOMM Computer Communication Review, 21(4), 123-130.

41. ITU-T Recommendation Y.1541 (12/11) Internet protocol aspects – Quality of service and network performance; Network performance objectives for IP-based services.

42. Sanaei, N., & Fatemi, A. (2021). Defects in additive manufactured metals and their effect on fatigue performance: A state-of-the-art review. Progress in Materials Science, 117, 100724.

43. Marcon, L. & Scarcella, C. & Detraz, S. & Lalovic, Milana & Olantera, L. & Prousalidi, Thenia & Sandven, U. & Sigaud, C. & Soós, C. & Troska, J.. (2023). High speed radiation tolerant optical links based on coarse wavelength division multiplexing. Journal of Instrumentation. 18. C02055. 10.1088/1748-0221/18/02/C02055.

44. Dorrah, A.H., Rubin, N.A., Tamagnone, M. et al. Structuring total angular momentum of light along the propagation direction with polarization-controlled meta-optics. Nat Commun 12, 6249 (2021). https://doi.org/10.1038/s41467-021-26253-4

45. Van Der Schaar, M., Krishnamachari, S., Choi, S., & Xu, X. (2003). Adaptive cross-layer protection strategies for robust scalable video transmission over 802.11 WLANs. IEEE Journal on selected areas in communications, 21(10), 1752-1763.

46. A. Tobagi and V.B. Hunt, "Performance Analysis of Carrier Sense Multiple Access with Collision Detection", Computer Networks, Vol. 4, pp. 245–259, 1980

47. Wu, Chien-Jang & Rau, Yu-Nian & Han, Wei-Hsieh. (2010). Enhancement of Photonic Band Gap in a Disordered Quarter-Wave Dielectric Photonic Crystal. Progress In Electromagnetics Research. 100. 10.2528/PIER09111610.

48. Yu, N., Capasso, F. Flat optics with designer metasurfaces. Nature Mater 13, 139–150 (2014). https://doi.org/10.1038/nmat3839

49. S. Norden, G. Manimaran and C. S. R. Murthy, "New protocols for hard real-time communication in the switched LAN environment," Proceedings 23rd Annual Conference on Local Computer Networks. LCN'98 (Cat. No.98TB100260), Lowell, MA, USA, 1998, pp. 364-373, doi: 10.1109/LCN.1998.727677.

50. Kisner, Roger & Manges, Wayne & Macintyre, Lawrence & Nutaro, James & Munro, Jr, John & Ewing, Paul & Howlader, Mostofa & Kuruganti, Teja & Wallace, Richard & Olama, Mohammed. (2010). Cybersecurity through Real-Time Distributed Control Systems. 10.2172/978289.

51. I. B. Djordjevic, "Channel coding for optical transmission systems," 2017 Opto-Electronics and Communications Conference (OECC) and Photonics Global Conference (PGC), Singapore, 2017, pp. 1-2, doi: 10.1109/OECC.2017.8114842.

52. Djordjevic, Ivan & Ryan, William & Vasic, Bane. (2010). Coding for Optical Channels. 10.1007/978-1-4419-5569-2.

53. Mariscotti, A. Stray Current Protection and Monitoring Systems: Characteristic Quantities, Assessment of Performance and Verification. Sensors 2020, 20, 6610. https://doi.org/10.3390/s20226610

54. H. Zhang, Q. Wu and J. Ji, "Synchronization of Discretely Coupled Harmonic Oscillators Using Sampled Position States Only," in IEEE Transactions on Automatic Control, vol. 63, no. 11, pp. 3994-3999, Nov. 2018, doi: 10.1109/TAC.2018.2814678

55. Choulakian, V. The optimality of the centroid method. Psychometrika 68, 473–475 (2003). https://doi.org/10.1007/BF02294738

56. Llopis, Eva & Micheli, Mario. (2014). Implementation of the Centroid Method for the Correction of Turbulence. Image Processing On Line. 4. 187-195. 10.5201/ipol.2014.105.

57. Matsuoka, Ryuji & Shirai, Naoki & Asonuma, Kazuyoshi & Sone, Mitsuo & Sudo, Noboru & Yokotsuka, Hideyo. (2011). Measurement Accuracy of Center Location of a Circle by Centroid Method. 6952. 297-308. 10.1007/978-3-642-24393-6_25.

58. Anne-Isabelle Henry, Julia M. Bingham, Emilie Ringe, Laurence D. Marks, George C. Schatz, and Richard P. Van Duyne, Correlated Structure and Optical Property Studies of Plasmonic Nanoparticles, The Journal of Physical Chemistry C 2011 115 (19), 9291-9305, DOI: 10.1021/jp201030

59. Lou, Zheng & Shen, Guozhen. (2016). Flexible Electronics: Flexible Photodetectors Based on 1D Inorganic Nanostructures (Adv. Sci. 6/2016). Advanced Science. 3. 10.1002/advs.201670030.\

60. Wang, Wenhui & Qi, Limin. (2019). Light Management with Patterned Micro- and Nanostructure Arrays for Photocatalysis, Photovoltaics, and Optoelectronic and Optical Devices. Advanced Functional Materials. 29. 1807275. 10.1002/adfm.201807275.

61. Bolboacă, S.D.; Jäntschi, L.; Sestraș, A.F.; Sestraș, R.E.; Pamfil, D.C. Pearson-Fisher Chi-Square Statistic Revisited. Information 2011, 2, 528-545. https://doi.org/10.3390/info2030528

62. Llopis, Eva & Micheli, Mario. (2014). Implementation of the Centroid Method for the Correction of Turbulence. Image Processing On Line. 4. 187-195. 10.5201/ipol.2014.105.

63. J. Wolf, "Efficient maximum likelihood decoding of linear block codes using a trellis," in IEEE Transactions on Information Theory, vol. 24, no. 1, pp. 76-80, January 1978, doi: 10.1109/TIT.1978.10558

64. Panteleev, Pavel & Kalachev, Gleb. (2021). Degenerate Quantum LDPC Codes With Good Finite Length Performance. Quantum. 5. 585. 10.22331/q-2021-11-22-585.

65. S. Cai, W. Lin, X. Yao, B. Wei and X. Ma, "Systematic Convolutional Low Density Generator Matrix Code," in IEEE Transactions on Information Theory, vol. 67, no. 6, pp. 3752-3764, June 2021, doi: 10.1109/TIT.2021.3064922.

66. Borysenko, Oleksiy & Kulyk, Igor & Matsenko, Svitlana & Berezhna, Olga & Matsenko, Oleksandr. (2016). Optimal synthesis of digital counters in the Fibonacci codes with the minimal form of representation. Eastern-European Journal of Enterprise Technologies. 4. 4. 10.15587/1729-4061.2016.75596.

67. Cai, Zhaohui & Hao, Jianzhong & Tan, P.H. & Sun, Sumei & Chin, P.S.. (2006). Efficient encoding of IEEE 802.11n LDPC codes. Electronics Letters. 42. 1471 - 1472. 10.1049/el:20063126.

68. Borysenko, Oleksiy & Matsenko, Svitlana & Novhorodtsev, Anatolii & Kobiakov, Oleksandr & Spolitis, Sandis & Bobrovs, Vjaceslavs. (2020). Estimating the Indivisible Error Detecting Codes Based on an Average Probability Method. Eastern-European Journal of Enterprise Technologies. 6/9. 25-33. 10.15587/1729-4061.2020.218076.

69. Matsenko, Svitlana & Borysenko, O. & Spolitis, Sandis & Bobrovs, Vjaceslavs. (2019). Noise Immunity of the Fibonacci Counter with the Fractal Decoder Device for Telecommunication Systems. Latvian Journal of Physics and Technical Sciences. 56. 12-21. 10.2478/lpts-2019-0027.

70. Ruskey, F. (2003). Combinatorial generation. Preliminary working draft. University of Victoria, Victoria, BC, Canada, 11, 20.

71. Herzog, J., Hibi, T., & Ohsugi, H. (2018). Binomial ideals (Vol. 279). Cham: Springer

72. Vilcane, K. & Matsenko, Svitlana & Parfjonovs, M. & Murnieks, Rihards & Aleksejeva, M. & Spolitis, Sandis. (2020). Implementation of Multi-Wavelength Source for DWDM-PON Fiber Optical Transmission Systems. Latvian Journal of Physics and Technical Sciences. 57. 24-33. 10.2478/lpts-2020-0019.

73. Borysenko, O.; Matsenko, S.; Bobrovs, V. Binomial Number System. Appl. Sci. 2021, 11, 11110. https://doi.org/10.3390/app112311110

74. V. Skachek and K. A. S. Immink, "Constant Weight Codes: An Approach Based on Knuth's Balancing Method," in IEEE Journal on Selected Areas in Communications, vol. 32, no. 5, pp. 909-918, May 2014, doi: 10.1109/JSAC.2014.140511.

75. Novitsky, Denis & Shalin, Alexander & Redka, Dmitrii & Bobrovs, Vjaceslavs & Novitsky, Andrey. (2021). Quasibound states in the continuum induced by PT symmetry breaking. Physical Review B. 104. 085126. 10.1103/PhysRevB.104.085126.

76. Thio, Tineke & Pellerin, K & Linke, Richard & Lezec, Henri & Ebbesen, T. (2002). Enhanced light transmission through a single subwavelength aperture. Optics letters. 26. 1972-4. 10.1364/OL.26.001972.

77. Denis V. Novitsky, Alina Karabchevsky, Andrei V. Lavrinenko, Alexander S. Shalin, Andrey Novitsky, PT symmetry breaking in multilayers with resonant loss and gain locks light propagation direction // Physical Review B, 98, 125102, 2018.

78. Hadi K. Shamkhi, Andrey Sayanskiy, Adria Canos Valero, Anton S. Kupriianov, Polina Kapitanova, Yuri S. Kivshar, Alexander S. Shalin, and Vladimir R. Tuz, Transparency and perfect absorption of all-dielectric resonant metasurfaces governed by the transverse Kerker effect // Phys. Rev. Materials, 3, 085201, (2019). DOI: 10.1103/PhysRevMaterials.3.085201

79. Pavel D. Terekhov, Kseniia V. Baryshnikova, Yakov Galutin, Yuan Hsing Fu, Andrey B. Evlyukhin, Alexander S. Shalin, and Alina Karabchevsky, Enhanced absorption in all-dielectric metasurfaces due to magnetic dipole excitation // Scientific Reports, V. 9:3438 (2019). https://doi.org/10.1038/s41598-019-40226-0

80. Adrià Canós Valero, Denis Kislov, Egor A. Gurvitz, Hadi K. Shamkhi, Alexander. A. Pavlov, Dmitrii Redka, Sergey Yankin, Pavel Zemánek and Alexander S. Shalin, Nanovortex-driven all-dielectric optical diffusion boosting and sorting concept for lab-on-a-chip platforms // Advanced Science, 2020, 1903049. https://doi.org/10.1002/advs.201903049

81. Hani Barhom, Andrey Machnev, Roman E. Noskov, Alexander A Goncharenko, Egor Gurvitz, Alexander S. Timin, Vitaliy A. Shkoldin, Sergei V. Koniakhin, Olga Yu. Koval, Mikhail Zyuzin, Alexander Sergeevich Shalin, Ivan Shishkin, and Pavel Ginzburg, Biological Kerker effect boosts light collection efficiency in plants // Nano Lett. 2019, 19, 10, 7062-7071, DOI: 10.1021/acs.nanolett.9b02540

82. Pavel D. Terekhov, Andrey B. Evlyukhin, Dmitrii Redka, Valentin S. Volkov, Alexander S. Shalin, Alina Karabchevsky, Magnetic Octupole Response of Dielectric Oligomers // Laser and Photonics Reviews, 2020, 1900331.

83. Seunghwi Kim, Jacob M. Taylor, and Gaurav Bahl, "Dynamic suppression of Rayleigh backscattering in dielectric resonators," Optica 6, 1016-1022 (2019)

84. Liu, C, Gao, W, Yang, B & Zhang, S 2017, 'Disorder-Induced Topological State Transition in Photonic Metamaterials', Physical Review Letters, vol. 119, no. 18, 183901. https://doi.org/10.1103/PhysRevLett.119.183901

85. Pitarke, J.M. & Silkin, V. & Chulkov, E.V. & Echenique, P.M.. (2006). Theory of surface plasmons and surface-plasmon polaritons. Reports on Progress in Physics. 70. 10.1088/0034-4885/70/1/R01.

86. Zhang, J., Zhang, L., & Xu, W. (2012). Surface plasmon polaritons: physics and applications. Journal of Physics D: Applied Physics, 45(11), 113001

87. Worthing, P. & Barnes, W.. (2001). Efficient coupling of surface plasmon polaritons to radiation using a bi-grating. Applied Physics Letters. 79. 3035-3037. 10.1063/1.1414294.

88. Zhang, Junxi & Zhang, Lide & Xu, Wei. (2012). Surface plasmon polaritons: Physics and applications. Journal of Physics D-applied Physics - J PHYS-D-APPL PHYS. 45. 10.1088/0022-3727/45/11/113001.

89. Han, Song & Rybin, Mikhail & Pitchappa, Prakash & Srivastava, Yogesh & Kivshar, Yuri & Singh, Ranjan. (2019). Guided-Mode Resonances in All-Dielectric Terahertz Metasurfaces. Advanced Optical Materials. 8. 10.1002/adom.201900959.

90. Niu, Xinxiang & Hu, Xiaoyong & Chu, Saisai & Gong, Qihuang. (2018). Epsilon-Near-Zero Photonics: A New Platform for Integrated Devices. Advanced Optical Materials. 6. 1701292. 10.1002/adom.201701292.

91. Li, Ying & Argyropoulos, Christos. (2018). Exceptional points and spectral singularities in active epsilon-near-zero plasmonic waveguides.

92. Solís, Diego & Engheta, Nader. (2022). Nonreciprocal Epsilon-Near-Zero-Dielectric Bilayers: Enhancement of Nonreciprocity from a Nonlinear Transparent Conducting Oxide Thin Film at Epsilon-Near-Zero Frequency. Physical Review Applied. 17. 10.1103/PhysRevApplied.17.034053.

93. L. Schares et al., "A Throughput-Optimized Optical Network for Data-Intensive Computing," in IEEE Micro, vol. 34, no. 5, pp. 52-63, Sept.-Oct. 2014, doi: 10.1109/MM.2014.77.

94. P. Papanikolaou, K. Christodoulopoulos, and E. Varvarigos, "Optimization Techniques for Incremental Planning of Multilayer Elastic Optical Networks," J. Opt. Commun. Netw. 10, 183-194 (2018)

95. Yongli Zhao, Boyuan Yan, Dongmei Liu, Yongqi He, Dajiang Wang, and Jie Zhang, "SOON: self-optimizing optical networks with machine learning," Opt. Express 26, 28713-28726 (2018)

96. Endsley, Mica. (2016). Situation awareness in aviation systems.

97. K. S. O'Brien & D. O'Hare (2007) Situational awareness ability and cognitive skills training in a complex real-world task, Ergonomics, 50:7, 1064-1091, DOI: 10.1080/00140130701276640

98. Kim, Jung-Hyung & Seong, Dae-Jin & Lim, Jong & Chung, Kwang-Hwa. (2004). Plasma frequency measurements for absolute plasma density by means of wave cutoff method. Applied Physics Letters. 83. 4725 - 4727. 10.1063/1.1632026

99. Taylor & Francis Group, "Optical Fiber Sensors – Advances Techniques and Applications",CRC Press, 2015.

100. Dandy G.C., Daniell, T.M., Foley, B.A. and Warner R.F, Planning and Design of EngineeringSystems. Third Edition, 2017.

101. Avraham Shtub, Yuval Cohen, Introduction to Industrial Engineering 2nd Edition, 2017

SUPPLEMENTS

1-PAPER: Aircraft Optical Video Transmission Communication based on the Forward Error Correction Codes

A. Krotov, M. Krotov, S. Matsenko, T. Salgals, V. Bobrovs, "*Aircraft Optical Video Transmission Communication based on the Forward Error Correction Codes,*" 2023 Photonics & Electromagnetics Research Symposium (PIERS), Prague, Czech Republic, (**2023**), DOI: 10.1109/PIERS59004.2023.10221478

Aircraft Optical Video Transmission Communication based on the Forward Error Correction Codes

Aleksandr Krotov[1], **Mihail Krotov**[1], **Svitlana Matsenko**[1],
Toms Salgals[1, 2], **and Vjaceslavs Bobrovs**[1]

[1]Institute of Telecommunications, Riga Technical University, Riga, Latvia
[2]Communication Technologies Research Center, Riga Technical University, Riga, Latvia

Abstract— Modern aircraft information and telecommunication systems are segmented into two separate networks: data transmission and video networks. This differs from the typical approach for modern telecommunications in which all types of traffic are transmitted through one network (for example, access NGN-IMS networks). The external aircraft electromagnetic environment is constantly becoming more complicated: the high intensity of the electromagnetic field (E_{mf}) due to the increase of radio frequencies quantity and their frequencies spectrum expansion, which occupies a band from $10\,\mathrm{kHz}$ to $3\,\mathrm{GHz}$ that affects the quality of service of electronic devices on board. A new method of image representation with forward error correction (FEC) codes was developed and considered. The method decreases the Bit Error Ratio (BER) for asymmetric data transmission via fiber optics and computational complexity for video correction. The paper investigates the superior performance of Low-Density Parity-Check (LDPC-) based on Irregular Repeat-Accumulate (IRA) codes over regular LDPC codes for the same code rate with Gaussian noise to match a certain signal-to-noise ratio (SNR). The LDPC FEC codes are simulated with code rates $R_c \in \{1/2\}$ from the digital video broadcasting by satellite — second-generation (DVB-S2) standard. This setup has 17 low-data network subscribers and one highly loaded network section for video transmission. This approach makes it possible to increase the load in the asymmetric networks for aircraft onboard electronic systems and to ensure the quality of video images in the pickup environment to avionics during operation, for example, radar devices.

1. INTRODUCTION

With the current technology level for optical data transmission networks, error minimization in the information received is one of the most critical tasks. The effective use of forward correction codes makes it possible to reduce the power consumption of transmitters or increase the transmission distance of information with a given error level. This lets us maintain the quality of the transmitted signal at a sufficient level. In aviation, the object of electromagnetic compatibility research is an aircraft and its onboard equipment capable of generating electromagnetic interference or being susceptible to it [1]. According to the degree of impact of failure on flight safety, aircraft systems are divided into four levels: A, B, C, and D [2]. Level A includes systems that perform so-called "critical" functions. Their violation leads to disastrous consequences. Examples include onboard telecommunications systems, electrical control, engine control, etc. The appearance of new high-speed digital communication interface lines on the aircraft, including fiber-optic ones, forces EMC specialists to change the widespread opinion that at frequencies above $300\,\mathrm{MHz}$, interference induced in the communication interface lines from HIRF quickly weakens with increasing frequency and can be ignored [3]. According to the development of quantum computer technologies it becomes possible to increase the speed of computer calculations, increase the communication channels security level and the ability to increase the density of data storage, which will help to deal with this problem. However, along with the presented advantages a number of problems arise: the occurrence of errors associated with the nature of quantum particles, the high cost of constructing quantum computers; the complexity of testing the effectiveness of quantum algorithms. Thus, at the moment, the introduction of optical methods of information transmission with proper noise-immune coding is still an urgent task. Figure 1 shows the aircraft network circuit diagram. Low-Density Parity Check (LDPC) codes are a case of linear block codes with parity check, the feature of which is a relatively low density of elements of the parity check matrix. In regular LDPC codes, the check matrix contains a constant number of ones in each column and each row (in irregular codes, it may vary from row to row and from column to column). Moreover, with an increase in the length of the code block, the total number of units of the check matrix increases linearly. Two principles for constructing a check matrix are used: using a pseudo-random generator (random, random-like

codes) and based on finite fields or groups-structured. Practice shows the qualitative superiority of random check matrices over structured ones. However, structured matrices make it possible to apply optimization methods (storage, encoding, and decoding).

Many proposed LDPC code designs are cyclic or quasi-cyclic, which allows fast decoding and efficient coding procedures. Moreover, even for non-cyclic LDPC codes, efficient coding techniques have been proposed [4, 5]. LDPC codes are preferred in channels with less error probability [6]. It must be said that LDPC is probably one of the optimal ones for quantum computers and networks [7]. Among the modern foreign standards for building the IMA information and telecommunications infrastructure, the two most promising standards can be distinguished:

- ARINC 664 Aircraft Information Networks;
- ARINC 818 High Data Rate Aircraft Digital Video Interface.

The ARINC 664 standard is based on the ADFX (Asynchronous Full Duplex Switched Ethernet) protocol, standardized by the ARINC working group, and based on the well-known IEEE 802.3 standard.
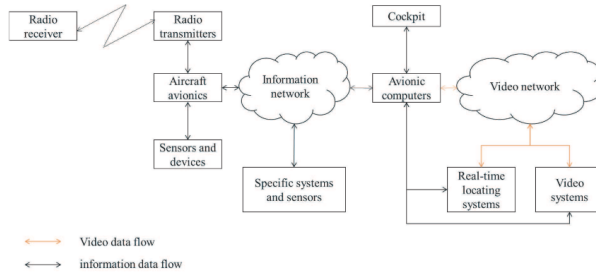

Figure 1: Aircraft network circuit diagram.

2. DEVELOPMENT METHODS

Low-speed (1.0625 Gb/s) ARINC 818 implementations can use twisted-pair physical distribution media or fiber optics. At speeds above 2 Gbit/s, specialized fiber optic transceivers of various modifications are used. For example, with network coverage < 500 m, onboard cables based on multimode fiber operating in a transparency window of 0.85 μm can be used. Large objects and networks with a coverage radius of up to 10 km are assumed to use single-mode fiber in the 1.3 μm range. It is assumed to use a specialized range of rates in the future, where the FC-AV rate of 1.0625 Gb/s is selected as the primary rate. The resulting value is formed by multiplying this value by the appropriate coefficient. The use of speeds of 1x, 2x, 4x, 8x (up to 8.5 Gbit/s), and later up to 12x, 16x, and 32x is envisaged.

In the case of ARINC-818, the transfer includes the following steps:

1. Video packed into special frames (ADVB), with the addition of downtime for timing;
2. Serialization and 8-bit/10-bit (8b/10b) encoding;
3. Serial transmission;
4. 8b/10b decoding;
5. Reconstruction, including clearing of aggregates (idles).

The container structure is shown in Figure 2, where 1 is the padding byte, 2 is the available byte, 3 is the frame header, 4 is the payload, 5 is the checksum, and 6 is the close byte. Eight-bit/10-bit (8b/10b) encoding allows data to be transmitted over long distances. For every 8 bits (every 1 byte) of information sent over the physical channel, 10 bits are transmitted, which increases the load on the physical channel by 25 percent. For example, to transmit 32 bits (4 bytes), 8b/10b encoding

52

would physically transmit 40 bits over the channel. Upon receipt, 4 bytes will be reduced to 32 bits. Bytes are designated as data or special characters such as the start of frame (2 in Figure 2 — SoF), end of frame (6 in Figure 2 EoF). A special fill character (1 in Figure 2). When data is not being transmitted over the physical channel, blank characters will be inserted to maintain continuous transmission.

The first frame of the ADVB container data sequence includes the container header and object 0 ancillary data as payload data. Subsequent frames of the container sequence Object 2's video pixel data. Each is limited to 2112 bytes, which may require splitting one video line into multiple ADVB frames. In the XGA example, each of the 1024 RGB pixels in a line requires three bytes (3072 bytes per line), so the video line must be split between two 2112-byte ADVB frames.

After t transmitting the video frame, a 4-byte CRC follows to check the error box. It uses the following 32-bit polynomial:

$$X^{32} + X^{26} + X^{23} + X^{22} + X^{16} + X^{12} + X^{11} + X^{10} + X^8 + X^7 + X^5 + X^4 + X^2 + X + 1 \quad (1)$$

All frames except the last frame of the ADVB container data transmission sequence use an end-of-frame (EOFn) ordered set, starting with a negative or positive RD. The last frame of the FC-AV container data transfer sequence uses an ordered set of End of Frame Terminate (EOFt), starting with RD Negative or RD Positive.

The basic protocol unit of the considered network is the Ethernet frames s, star-shaped or tree-like topology network nodes are used as passive devices — optical splitters that do not require a power supply. A, single fiber is used as a physical distribution medium in network. The proposed network uses only one wavelength for bidirectional transmission, which provides a practical application in systems with wave separation.

3. SIMULATION

An optical local network protocol, which will ensure guaranteed delivery and low latency of information frames transmitted in the local network at the access level over the entire range of loads, allows to implement of a conflict-free access method and protists against errors that occur when frames are transmitted through a common channel as well as low susceptibility to electromagnetic interference, interference and complete electrical isolation of the terminals included in the network, which creates additional noise immunity due to the lack of the possibility of stray currents.

Access devices (B) have two modes of operation: peripheral — "P" and central — "C". Moreover, if one B in the network is in the "C" mode, all other Bs are in the "P" mode.
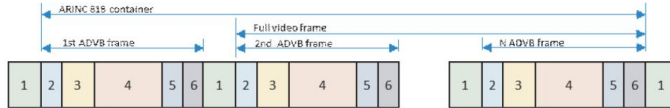

Figure 2: ARINC-818 container structure.

Figure shows the variant of local network organization based on the proposed protocol 3. In this figure, the access device B1 is in the "C" mode, and the access devices Bi ÷ BN are in the "P" mode. All Bs are connected by optical lines to the passive splitter PS and are connected through interfaces, each with its electronic module (EM). Thus, the optical signal is branched between all Bs, and a passive bus optical mono channel is created (where all access units "hear" everyone). The network can be in three modes:

1. In phasing mode (clock synchronization).
2. In the polling mode. The T base stations in the "P" mode are polled by the B in the "C" mode and assigning access intervals.
3. In data transfer mode.

In the phasing mode, the process of phasing the B in the "P" mode is based on the periodic transmission to the line from the B in the "C" mode of phasing combinations. Phasing patterns are

transmitted at fixed time intervals equal to the duration of the transmission cycles (TC), always at the same time positions. Data transmission, polling, and assignment of access time intervals at phasing intervals "a" are blocked.

After the end of interval "a" in the polling mode, the first cycle of polling and assignment of access windows begins (the first interval T_0 in Figure 4), which fits into one or more intervals of the transmission window T_0.

Next, the network switches to the data transfer mode, and information frames and receipts transmission starts in the assigned access windows until the end of the transfering sett the cycle of polling and assigning access windows resumes. Additional time windows are provided to accommodate the polling cycles and assign windows in the transmission cycle. Additional time windows are provided to accommodate the polling cycles and assign windows in the transmission cycle. In this case, if only one access unit sent a positive signal in the current cycle that it has a frame transmission (i.e., the presence of a single state of the ready trigger, then it will be assigned the first transmission window, after which a second poll will be performed. If, during the next survey, two Bs are detected in the network with ready triggers set to a single state, then the first B will be assigned the first window, the second — the second, and so on. If all Bs polled in the next cycle have triggers set to single states, then corresponding windows will be assigned to all blocks in turn, and all Bs are guaranteed to be able to transmit their information frames once in one cycle. In this case, each frame, in case of its error-free transmission, will be acknowledged by a positive receipt transmitted in the transmission time window of this frame, after which the next B operating in the "P" mode will send its frame and so on until the end of the cycle. If errors are detected during frame transmission by at least one B (its error detector) and a negative receipt is transmitted by this B (which happens very rarely due to the high quality of the optical channel and the absence of collisions), all other access units will accept these receipts and the transmission cycles of all B except the sender B will be suspended. In this case, the sender will continue to send its frame in the following time windows until it receives a positive receipt from the recipient. B will again collect information from the Bs in the "P" mode and assign them time windows of access. The transmitter will transmit information to all B that is in the "P" mode about the assignment of the corresponding access windows, and the transmission cycle will resume.

In phasing mode, data transmission, polling cycles, and window assignments are disabled. The B, which is in the "C" mode, synchronizes (phasing) to the B, which is in the "P" mode, a special protocol.

In this case, a synchro pattern is transmitted to the line from the B, which is in the "C" mode. From the output of the encoder-decoder, the synchro pattern encoded with a linear code is fed to the input of the optical transmitter, from the output of which the optical signal is transmitted through the separation device to the optical line and through the PS (see Figure 3) to optical interfaces of other B that are in the "P" mode. In each of these Bs, the optical signal is fed to the line input of the separating device. The command receiver decodes the sync pattern and outputs a "sync pattern identification" signal via one of its output group line wires with a pulse corresponding to the moment of decoding the phasing pattern. After the completion of the transmission of the phasing combination by the B in the "C" mode and the end of the phasing of Bs in the "P" mode, the network switches to the polling mode and assigning access windows.

When transmitting the "load request" commands, the B, which is in the "C" mode, alternately outputs the addresses of the interrogated Bs "P" entered the "load request" commands broadcast in the direction of the corresponding Bs in the "P" mode as well as the control signal "transmission of commands load request." Load request commands are transmitted through the optical network in the same way as phasing patterns as described above.

We simulated a network using a given protocol based on ARINC-818 with an AWGN channel.

4. RESULTS

Figure 5 shows Bit error ratio (BER) vs. Signal-noise ratio (SNR) as the result of simulation for LDPC and LDPC-IRA FEC codes.
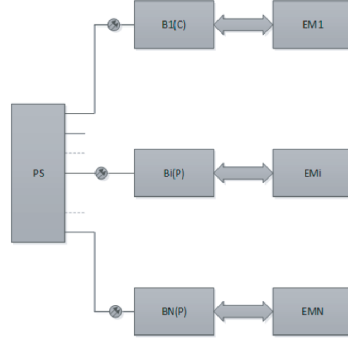
Figure 3: Considered organization of the local network. PS — passive splitter; B, Bi, BN — access devices; EM — electronic module.
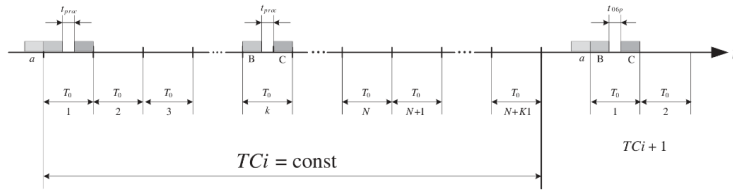

Figure 4: The protocol time chart. a — is the phasing interval; b — polling cycle; c — window assignment cycle; t_{proc} — query processing interval by the analyzer; T_0 is the transmission window interval; TCi — i-th transmission cycle; $TCi + 1$ — next $i + 1$ transmission cycle (beginning).
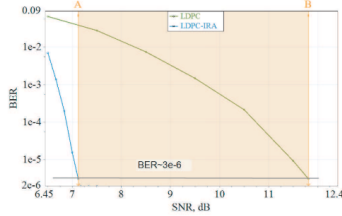

Figure 5: Bit error ratio (BER) vs. Signal-noise ratio (SNR) for LDPC and LDPC-IRA.
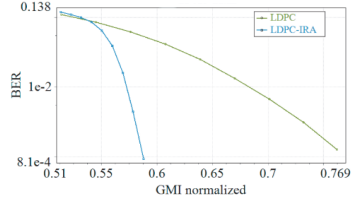
Figure 6: Bit error ratio (BER) vs. normalized Generalized mutual information (GMI) for LDPC and LDPC-IRA.

According to the simulation results, we obtained a significant advantage of LDPC-IRA over LDPC. Modeling on 16-QPAM modulation shows that LDPC-IRA provides a BER of $2 \cdot 10^{-6}$ at SNR 7.2 dB. The addition of LDPC-IRA coding to ARINC-818 improves transmission efficiency more than three times. Within of problem solving, this makes it possible to increase the stability of the system under the influence of HIRF.

Figure 6 shows Bit error ratio (BER) vs. normalized Generalized mutual information (GMI) for LDPC and LDPC-IRA FEC codes.

LDPC-IRA in the system under consideration will reduce the dispersion of information when working with certain initial data, for example, during video transmission by more than 1.3 times.

5. CONCLUSION

Thus, we have obtained a new image transmission method based on the standard ARINC 818 protocols, suitable for use in onboard optical communication systems, which does not reduce network speed and does not increase the load on onboard computers while providing increased BER suitable for streaming video broadcasting under conditions exposure to High-intensity Radiated Field. Simulation for LDPC and LDPC-IRA $R_c \in \{1/2\}$ FEC codes showed Bit error ratio (BER) vs. Signal-noise ratio (SNR) and Bit error ratio (BER) vs normalized Generalized mutual information (GMI) that performes efficiency of LDPC-IRA FEC code vs LDPC. Thus, LDPC-IRA provides more than 20% efficiency for aircraft optical video networks in HIRF environment.

REFERENCES

1. Dementyev, A. N., D. S. Klyuev, A. N. Novikov, A. S. Mezhnov, Y. A. Piterskova, E. V. Zakharova, and L. A. Dementyev, "Model of the process of assessing the electromagnetic compatibility of the onboard equipment of the aircraft," *Trudy MAI*, No. 123, 2022.
2. DO-160G: 2011, "Environmental conditions and test procedures for airborne equipment," 438, USA, 2011.
3. Schroder, A., et al., "Analysis of high-intensity radiated field coupling into aircraft using the method of moments," *IEEE Transactions on Electromagnetic Compatibility*, Vol. 56, 113–122, 2014.
4. Haddadi, S., M. Farhang, and M. Derakhtian, "Low-complexity decoding of LDPC codes using reduced-set WBF-based algo-rithms," *J. Wireless Com. Network 2020*, 180, 2020.
5. Vatta, F., A. Soranzo, M. Comisso, G. Buttazzoni, and F. Babich, "A survey on old and new approximations to the function $\phi(x)$ involved in LDPC codes density evolution analysis using a gaussian approximation," *Information*, Vol. 12, No. 5, 212, 2021.
6. Tamrazian, G. M., A. A. Gladkikh, and D. V. Ganin, "Hardware implementation of the optimal LDPC decoder," *Automation of control Processes*, Vol. 3, No. 41, 2015.
7. Breuckmann, N. P. and J. Eberhardt, "LDPC quantum codes," 2021.

2-PAPER: CPA-Lasing Associated with the Quasibound States in the Continuum in Asymmetric Non-Hermitian Structures

D. Novitsky, A.C. Valero, **A. Krotov**, T. Salgals, A.S. Shalin, A. Novitsky
"*CPA-Lasing Associated with the Quasibound States in the Continuum in Asymmetric Non-Hermitian Structures*, " ACS Photonics. 9., (**2022**), DOI: 10.1021/acsphotonics.2c00790

CPA-Lasing Associated with the Quasibound States in the Continuum in Asymmetric Non-Hermitian Structures

Denis V. Novitsky,* Adrià Canós Valero, Aleksandr Krotov, Toms Salgals, Alexander S. Shalin, and Andrey V. Novitsky

Cite This: *ACS Photonics* 2022, 9, 3035−3042

Read Online

ACCESS | Metrics & More | Article Recommendations | Supporting Information

ABSTRACT: Non-Hermitian photonic systems with loss and gain attract much attention due to their exceptional abilities in molding the flow of light. Introducing asymmetry to the $\mathcal{PT}$-symmetric system with perfectly balanced loss and gain, we reveal the mechanism of transition from the quasibound state in the continuum (quasi-BIC) to the simultaneous coherent perfect absorption (CPA) and lasing in a layered structure comprising epsilon-near-zero media. Two types of asymmetry (geometric and non-Hermitian) are analyzed with the scattering matrix technique. The effect of the CPA-lasing associated with the quasi-BIC is characterized with the unusual linear dependence of the quality factor on the inverse of the asymmetry parameter. Moreover, the counter-intuitive loss-induced-lasing-like behavior is found at the CPA-lasing point under the non-Hermitian asymmetry. The reported features of non-Hermitian structures are perspective for sensing and lasing applications.

KEYWORDS: *bound states in the continuum, coherent perfect absorption, lasing, scattering matrix, multilayer structure*
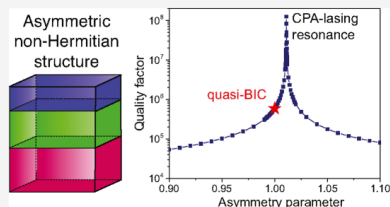
■ INTRODUCTION

Since the pioneering work of $\mathcal{PT}$-symmetric quantum mechanics,[1] non-Hermitian physics became an extremely wide field of research concerning not only quantum effects but also branches of classical physics including photonics, mechanics, electrical engineering, and even biophysics.[2] Principles of the non-Hermitian photonics have stimulated an especially fruitful design of novel optical systems with loss and gain elements. $\mathcal{PT}$-symmetric structures with balanced loss and gain as a particular case of non-Hermitian systems have attracted most attention due to their ability to implement basic effects of both $\mathcal{PT}$-symmetric response and symmetry breaking.[3−6] Applications of $\mathcal{PT}$ symmetry in optics and photonics are diverse and include sensing with enhanced sensitivity,[7−9] slowing of light,[10] effective single-mode lasing,[11−14] coherent perfect absorption (CPA),[15−17] topological-protection of surface states,[18] and even training of optical neural networks.[19]

There are two basic geometries widely employed in the studies on non-Hermitian photonics.[3] Longitudinal geometry is used in single-mode[20] and multimode coupled waveguides,[21−23] one-[24] and two-dimensional photonic lattices,[25] and coupled microcavities.[26] The most popular transverse geometry is a multilayer structure with alternating loss and gain media. Being a non-Hermitian generalization of the photonic crystal concept, such a multilayer attracts much attention due

to its simplicity for analysis and availability for unusual optical responses, such as anisotropic transmission resonances,[27] resonant scattering,[28] nonlinear saturation effects,[29−32] non-locality,[33] pulse-propagation effects,[34,35] effects of disorder,[36] and so forth. From the more general perspective, many of these effects can be treated as "anomalies" in light scattering[37,38] being described by means of scattering matrix technique.[27,39] The features of light scattering on dielectric structures were deeply studied in recent years.[40−44]

A special type of "anomaly" is a singular optical response in media with permittivity close to zero, which are called epsilon-near-zero (ENZ) media. The ENZ media demonstrate a number of unique properties such as wavelength expansion, field enhancement, light tunneling, light velocity manipulation, and strong nonlinear and nonlocal effects.[45−47] Here, we are interested in the so-called bound states in the continuum (BICs)—trapped modes of open cavities with perfect localization of radiation and resonances of infinite quality (Q)
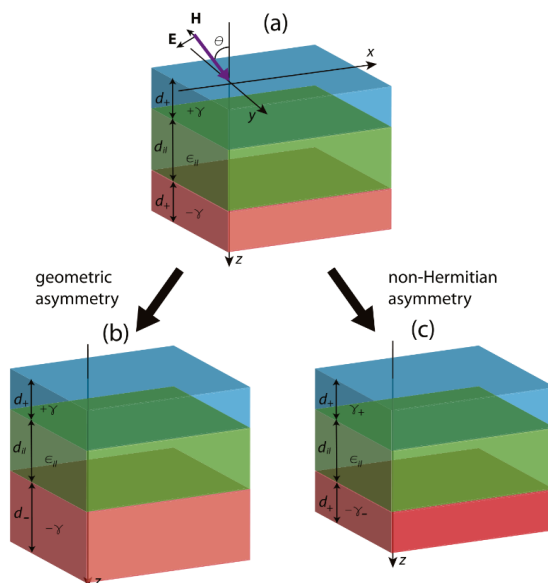
Figure 1. Schematic of an asymmetric trilayer consisting of the outer layers with loss and gain ENZ media, respectively, and the dielectric spacer. The outer layers are initially of the same thicknesses d_+ and non-Hermiticity parameters γ (a). Asymmetry has either (b) geometric ($d_- = \alpha d_+$) or (c) non-Hermitian ($\gamma_- = \beta \gamma_+$) origin as shown in the lower part of the figure. The spacer has the thickness $d_{il} = 10d_+$ and permittivity $\varepsilon_{il} = 5$.
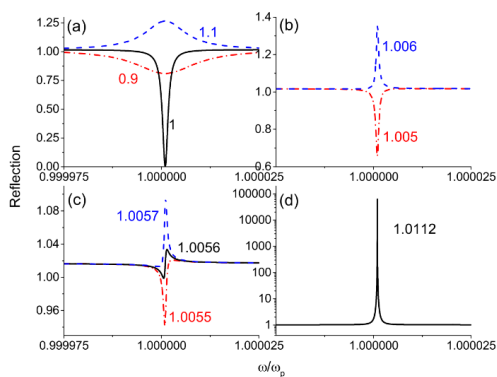

Figure 2. Spectra of reflection for different geometric asymmetry parameters α marked as numbers near the curves: (a) $\alpha = 0.9$, 1, and 1.1; (b) $\alpha = 1.005$ and 1.006; (c) $\alpha = 1.0055$, 1.0056, and 1.0057; and (d) $\alpha = 1.0112$. The angle of incidence is $\theta = 23.881°$, the non-Hermiticity magnitude $\gamma = 0.001$.
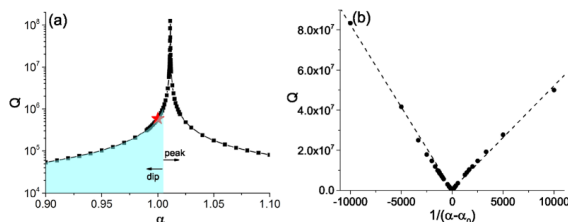
59

Figure 3. Dependence of the Q factor (a) on the geometric asymmetry parameter α and (b) on the value $1/(\alpha - \alpha_0)$. The angle of incidence is $\theta = 23.881°$, the non-Hermiticity magnitude $\gamma = 0.001$. The red star shows the quasi-BIC position at $\alpha = 1$, whereas the filled area marks the transition between the dip and peak.

factor.[48−50] ENZ-containing structures can support BICs both in waveguide[51] and layered geometries.[52−56]

In this paper, we study a non-Hermitian generalization of the ENZ-containing layered structures supporting bound states in the continuum. It has been recently shown[57] that $\mathcal{PT}$-symmetry breaking in the structures with balanced loss and gain results in transformation of a BIC into quasi-BIC, which is the resonance with the finite Q factor. Here, we make a further step introducing asymmetry in the distribution of loss and gain. The asymmetry (either in the thicknesses of layers or in the non-Hermiticity value itself, see Figure 1) serves as an additional degree of freedom for transferring from the quasi-BIC to another "anomaly" effect—the CPA-lasing point—as is demonstrated using the analysis of the scattering-matrix poles and zeros. The CPA-lasing in this case is directly associated with the quasi-BIC providing strong light amplification, linear dependence of the Q factor on the inverse asymmetry parameter, and loss-induced-like lasing effect.

RESULTS AND DISCUSSION

Geometric Asymmetry. We start with the non-Hermitian trilayer system having outer loss and gain layers of different thicknesses and the spacer (interlayer) between them (Figure 1). This case is characterized by violation of the gain-loss balance due to dimensions and, therefore, is called the geometric asymmetry. To be consistent with ref 57, we take the permittivity of the loss and gain media $\varepsilon_{\pm}(\omega) = 1 \pm i\gamma - \omega_p^2/\omega^2$, where ω_p is the plasma frequency and γ is the non-Hermiticity magnitude. Exploitation of the classical Drude-Lorentz model does not spoil the conclusions we make further. The loss layer has the thickness $d_+ = \lambda_p/2\pi$ (i.e., $\omega_p d_+/c = 1$, where c is the speed of light), whereas the gain layer has different thickness $d_- = \alpha d_+$, where α is the geometric asymmetry parameter. The parameters of the spacer are $d_{il} = 10d_+$ and $\varepsilon_{il} = 5$.

In our previous paper,[57] the symmetric case ($\alpha = 1$) has been already studied. In the Hermitian limit ($\gamma = 0$), the symmetric system possesses an unobservable infinitely narrow resonance (BIC) due to destructive interference of the Fabry-Perot mode and the volume plasmon excited by TM-polarized waves at the plasma frequency. When $\gamma > 0$, the non-Hermiticity drives the transition of perfect BIC to the quasi-BIC through the mechanism of $\mathcal{PT}$ symmetry breaking. This quasi-BIC, which can be reached at the incidence angle

$$\theta_{BIC} = \arcsin\sqrt{\varepsilon_{il} - \left(\frac{\pi c n}{\omega_p d_{il}}\right)^2}$$ (n is the integer), shows up in

spectra as a finite-width resonance, see the solid line in Figure 2a.

Let us fix the angle of incidence ($\theta = \theta_{BIC} \approx 23.881°$ at $n = 7$) and the non-Hermiticity magnitude ($\gamma = 0.001$) and start changing the geometric asymmetry parameter α. Reflection spectra calculated within the transfer-matrix method[57] are shown in Figure 2. For $\alpha < 1$, the thickness of the gain layer gets smaller than the thickness of the loss layer, $d_- < d_+$, so that the quasi-BIC resonance dip just becomes broader and shallower [see the line at $\alpha = 0.9$ in Figure 2a]. The case of $\alpha > 1$, when $d_- > d_+$, is much more interesting due to its richer physics connected to competition between loss and gain. As shown in Figure 2a, there is a broad resonance peak at $\alpha = 1.1$, so that the transfer from the dip to the peak happens somewhere between $\alpha = 1$ and 1.1. Analysis shows that this transition happens at $\alpha_t \approx 1.0056$, when the system contains slightly more gain than loss. There is no paradox that $\alpha_t \neq 1$ because for $0 < \alpha < \alpha_t$, the gain results in the overall (wideband) reflection with intensity coefficient $R > 1$, while the dip appears on this background. The resonance keeps symmetric line quite close to α_t [Figure 2b] and becomes asymmetric only in the very vicinity of the transition. The line at α_t clearly has the Fano profile [Figure 2c] stemming from the interplay between wide Fabry-Perot and narrow plasmonic resonances. Finally, close to some intermediate asymmetry parameter $\alpha_0 = 1.0112$, the reflection peak reaches maximum [Figure 2d] and then gradually diminishes. The transition point α_t corresponds to the middle between the deepest dip at $\alpha = 1$ and highest peak at $\alpha = 1.0112$ in agreement with expected linearity of the response on small perturbation.

As a quantitative characteristic of the observed resonances, we calculate the quality (Q) factor. Due to the symmetry of lineshapes outside the immediate vicinity of the transition from the dip to peak, it can be estimated with the simple relation $Q = \omega_0/\Delta\omega$, where ω_0 is the frequency of the resonance peak or dip and $\Delta\omega$ is the full width of the resonance. Such a consideration is in accordance with the modern treatment of non-Hermitian resonances using the quasi-normal modes characterized by complex frequencies.[58] We apply the same definition of the Q factor to the stationary spectra with both overall loss and gain because it gives reasonable results consistent with each other (only close to the maximum one can expect manifestation of instability). In addition, the large Q factor implies strong localization of radiation whether output intensity gets attenuated or amplified. Dependence of the Q factor on the parameter α calculated with this expression is
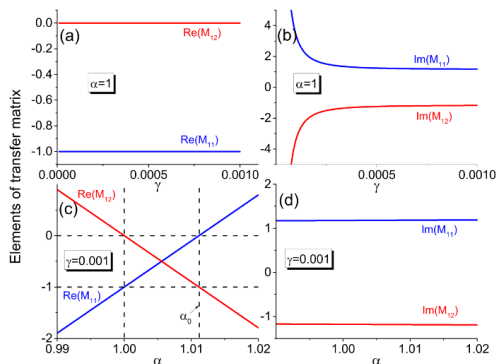
60

Figure 4. Dependence of the real and imaginary parts of the transfer-matrix elements (a)–(b) on the non-Hermiticity parameter γ for the symmetric structure and (c)–(d) on the asymmetry parameter α for $\gamma = 0.001$. The angle of incidence is $\theta = 23.881°$, the frequency is $\omega = \omega_p$.

shown in Figure 3. One can see that the powerful peak at $\alpha \approx \alpha_0$ in Figure 2d corresponds to the sharp increase of the Q factor exceeding 10^8. This amplification of the reflection and transmission are linked to strong localization of radiation inside the structure.

Figure 3b shows that the Q factor is inversely proportional to the geometric asymmetry parameter α. This result is in contrast to what is observed in usual BICs, which demonstrate the inverse behavior of Q as a function of the square of the asymmetry factor.[59] On the other hand, the recently introduced non-Hermitian BICs (so-called pt-BICs) reported in ref 60 have precisely such an inverse behavior of Q as a function of the longitudinal wavenumber playing the role of the asymmetry parameter. The fundamental difference with that case is that our system is not $\mathcal{PT}$ symmetric due to the asymmetry between loss and gain layers, so that the maximal Q factor is reached at some $\alpha_0 > 1$.

What is the nature of the Q factor enhancement at α_0? To address this question, let us consider poles and zeros of the scattering matrix of our system. The scattering matrix gives the equivalent results as the effective Hamiltonian approach,[39] but is more convenient to analyze the multilayer structures. In general, the scattering matrix of a multilayered structure has the form $\hat{S} = \begin{pmatrix} t & r_R \\ r_L & t \end{pmatrix}$.[39] Here, $t = 1/M_{11}$ is the transmission coefficient and $r_L = M_{21}/M_{11}$ and $r_R = -M_{12}/M_{11}$ are the reflection coefficients for the left- and right-incident waves which can be determined through the corresponding elements of the transfer matrix M.[57,61] A pole of the scattering matrix can be determined from the condition of the mode self-excitation arising at $t = \infty$ or, equivalently, $M_{11} = 0$. According to ref 37, the condition for a scattering matrix zero is $t \pm r = 0$ resulting in $M_{12} = \pm 1$ or $M_{21} = \pm 1$. The conditions for poles and zeros are generally fulfilled at complex frequencies. A BIC appears in Hermitian systems when pole and zero meet at the real axis of the complex-frequency plane.[37] One can directly confirm that this happens in the symmetric trilayer at $\gamma = 0$, $\omega = \omega_p$ and $\theta = \theta_{BIC}$, where the elements of the transfer matrix become real with $M_{11} = 0$, $|M_{12}| = |M_{21}| = 1$. Introduction of

non-Hermiticity breaks this exact BIC down as reported in ref 57. Figure 4a,b shows how this looks like from the viewpoint of poles and zeros. One can see that both elements of the transfer matrix are complex for $\gamma \neq 0$, with real parts $\mathrm{Re}M_{11} = -1 \neq 0$ and $\mathrm{Re}M_{12} = 0 \neq \pm 1$, so that the condition for the coalescence of pole and zero is not fulfilled anymore (because $M_{21} = M_{12}^*$, further we consider only M_{12}).

Influence of the geometric asymmetry on the components of the transfer matrix is shown in Figure 4c,d. Whereas their imaginary parts change only slightly, the real parts demonstrate clear linear dependence on α, so that $\mathrm{Re}M_{11} \approx 0$ and $\mathrm{Re}M_{12} \approx -1$ at $\alpha = \alpha_0$. Although the imaginary parts do not vanish, the values of the real parts allow us to suggest that we effectively reach both the pole and zero at $\alpha = \alpha_0$. Nonzero imaginary parts can be considered as an almost constant background which only limits possible values of the Q factor making it finite. Thus, the asymmetry can be used to compensate the mismatch between pole and zero induced by non-Hermiticity. Moreover, one can estimate the change of the transfer-matrix elements with α by using the analytical expression for M. Because this expression is very cumbersome, it is more convenient for the illustration to substitute all the parameters, except α and obtain the numerical dependence $M(\alpha)$. For example, we result in $M_{11}(\alpha) \approx (-93.17 + 0.58i)\cosh[(0.40 + 0.0012i)\alpha] + (240.18 + 0.67i)\sinh[(0.40 + 0.0012i)\alpha] \approx -(1 - 1.18i) + (89.62 + 0.66i)(\alpha - 1)$, which gives a very good linear approximation for $M_{11}(\alpha)$ shown in Figure 4c and allows us to estimate α_0.

It is known that in non-Hermitian systems, the coincidence of pole and zero heralds an intriguing effect of simultaneous CPA and lasing.[37] In our case, the lasing can be immediately associated with the sharp growth of the Q factor at $\alpha = \alpha_0$. To further corroborate this interpretation, in the Supporting Information, we demonstrate the CPA effect in our structure for the same conditions as lasing.

Thus, the peak of the Q factor reported above has the nature of the CPA-lasing point. However, the appearance of this point in the asymmetric structure is closely related to that of the quasi-BIC in the symmetric one. The sharp increase of the Q

61

factor and the lasing at α_0 are achievable for the gain layer which is only 1.12% thicker than the loss layer. Such a small difference in thickness matters because light intensity is localized under the conditions close to the quasi-BIC resonance. Therefore, we call the observed effect the CPA-lasing associated with the quasi-BIC.

The previous consideration was performed at the specific value of loss and gain parameter γ. The same approach based on the pole and zero dynamics and allowing us to estimate the CPA-lasing asymmetry parameter α_0 can be applied to any level of non-Hermiticity. As a result, we obtain the dependence $\alpha_0(\gamma)$ shown in Figure 5. The BIC is observed in the Hermitian
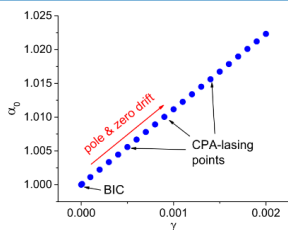

Figure 5. Change of the geometric asymmetry parameter α_0 corresponding to the pole and zero coincidence with the non-Hermiticity parameter γ.

case ($\gamma = 0$) and in the symmetric structure with $\alpha_0 = 1$. Increasing γ leads to the drift of pole and zero coincidence to the nonunitary asymmetry, $\alpha_0 > 1$. As a result, we obtain the line of CPA-lasing points in the plane (γ, α_0). It is interesting to note that this line is clearly straight, indicating the linear dependence between non-Hermiticity and asymmetry in the analyzed system.

If the condition for the incidence angle ($\theta = \theta_{\mathrm{BIC}}$) is relaxed (e.g., we deal with the normal incidence of light), the much thicker gain medium should be used to reach the lasing. In that case, however, lasing is due to the pole dynamics only, in contrast to our case. Thus, the use of the CPA-lasing point associated with the quasi-BIC provides a different mechanism and allows us to optimize the lasing structures, in particular lower the lasing threshold.

The CPA-lasing phenomenon associated with the quasi-BIC can be compared with the similar effect reported by Song et al.[60] In that paper, it is shown that a $\mathcal{PT}$-symmetric perturbation splits the BIC into the pt-BIC and lasing threshold modes. Song et al.'s pt-BIC is characterized by the Q factor having the linear dependence on the inverse asymmetry parameter in contrast to the usual for BICs' inverse dependence on the squared asymmetry parameter. In our case, the dependence is also linear, but the situation is fundamentally different: the asymmetry perturbation violates existing $\mathcal{PT}$ symmetry of the loss-gain distribution and transforms the quasi-BIC into the CPA-lasing point. We emphasize the role of asymmetry which distinguishes our results also from the CPA-lasing arising from the BIC under the $\mathcal{PT}$-symmetric perturbation in electronic circuits.[62]

Non-Hermitian Asymmetry. In this section, we consider a geometrically symmetric ($d_+ = d_-$) trilayer structure with violated balance between loss and gain. We introduce another asymmetry parameter $\beta = \gamma_-/\gamma_+$, where γ_+ and γ_- are the loss and gain magnitudes, respectively. The asymmetry realized through parameter β can be called non-Hermitian asymmetry. Condition $\beta > 1$ implies the dominating impact of gain in the system's response. One can expect that $\beta > 1$ has a similar effect as the increase of the gain layer thickness ($\alpha > 1$) discussed above. However, this is not the case.

As shown in Figure 6a, the elements of the transfer matrix approach the CPA-lasing condition (simultaneous $\mathrm{Re}M_{11} \approx 0$ and $\mathrm{Re}M_{12} \approx -1$) at $\beta = 0.99$, that is, in the overall lossy system. This results in an increase of reflection with the

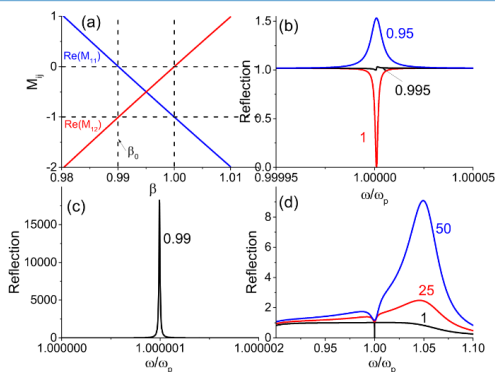**Figure 6.** (a) Dependence of the transfer-matrix elements on the asymmetry parameter β at the plasma frequency. (b)−(d) Spectra of reflection for different non-Hermitian asymmetry parameters β marked as numbers near the curves: (b) $\beta = 0.95$, 0.995, and 1; (c) $\beta = 0.99$; (d) $\beta = 1$, 25, and 50. The angle of incidence is $\theta = 23.881°$, the loss magnitude $\gamma_+ = 0.001$.

62

decrease in β as corroborated with the spectra shown in Figure 6b with the dip-to-peak transition at $\beta_t \approx 0.995$. The CPA-lasing condition at $\beta = 0.99$ corresponds to the extremely amplified reflection [Figure 6c] and the strongly enhanced Q factor (Figure 7). As in the case of geometric asymmetry, the Q
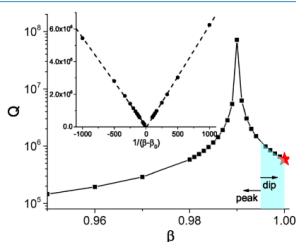

Figure 7. Dependence of the Q factor on the non-Hermitian asymmetry parameter β and on the value $1/(\beta - \beta_0)$ (inset). The angle of incidence is $\theta = 23.881°$, the loss magnitude $\gamma_+ = 0.001$. The red star shows the quasi-BIC position at $\alpha = 1$, whereas the filled area marks the transition between the dip and peak.

factor linearly depends on inverse of the non-Hermitian asymmetry parameter (see the inset in Figure 7), although the peak value of Q is somewhat lower due to the lossy character of the structure.

On the contrary, for the systems with overall gain, we do not see any significant increase of the reflected (and transmitted) radiation in vicinity of the plasma frequency even for as great asymmetry parameter as $\beta = 50$ [Figure 6d]. Formation of the dip for $\beta > 1$ can be explained as the quasi-BIC in the symmetric case ($\beta = 1$) broadened and elevated by the overall gain in the asymmetric structure. Amplification of the reflection (as well as transmission) happens mostly above the plasma frequency where the outer layers are dielectric-like. We should also emphasize the narrowband nature of CPA-lasing [Figure 6c] as opposed to the strongly wideband usual amplification [Figure 6d] which can be of interest for possible applications.

Our analysis demonstrates that the CPA-lasing point associated with the quasi-BIC can be reached using the non-Hermitian asymmetry either. Its behavior is caused by the interplay of loss and gain and provides one more piece of evidence of loss-induced effects in addition to the loss-induced transparency[63] and loss-induced lasing[64] in non-Hermitian systems. Although the loss-induced lasing is well-known in distributed-feedback lasers,[65] the feature of our loss-induced CPA-lasing is that we use the asymmetry as a driver for such an unusual response possible due to the quasi-BIC proximity.

The above considerations have been performed at the plasma frequency where the true BIC exists in the Hermitian limit and the non-Hermiticity-induced quasi-BIC resonance has a symmetric lineshape. At the nearby frequencies, the asymmetric Fano resonances appear at the angles different from θ_{BIC} and can be used to realize the amplified response (although, strictly speaking, not CPA-lasing) in asymmetric structures as well. The corresponding examples are discussed in the Supporting Information.

CONCLUSIONS

To sum up, we have introduced the concept of the CPA-lasing associated with the quasi-BIC unveiled in asymmetric non-Hermitian ENZ-containing layered structures. One can say that asymmetry in these structures supports transformation of the quasi-BIC resonance into the CPA-lasing resonance. The cases of different thicknesses of loss and gain layers (geometric asymmetry) and unequal levels of loss and gain (non-Hermitian asymmetry) have been studied. The effects of asymmetry have been analyzed in the framework of poles and zeros of the scattering matrix revealing intriguing features. We have determined a CPA-lasing point of merging pole and zero characterized by strong amplification of the outcoming intensity and sharp increase of the Q factor associated with the nearby quasi-BIC. We would like to highlight two important results found out in this paper. First, the Q factor has unusual inverse linear dependence on the asymmetry parameter. Second, the counter-intuitive loss-induced amplification is discovered in the system with non-Hermitian asymmetry at the plasma frequency. In contrast to the CPA-lasing in usual $\mathcal{PT}$-symmetric structures,[17] the CPA-lasing associated with the quasi-BIC can be reached at much lower values of loss and gain due to the strong localization of light inside the structure. Our approach also allows us to relax the requirements to the precise symmetry of system's parameters which is often difficult to meet. We believe that the results reported here are of general interest for non-Hermitian photonics and can be extended to two- and three-dimensional systems. The CPA-lasing effect associated with the quasi-BIC is envisaged to be demanded in laser and nonlinear-optics systems based on strong light enhancement.

ASSOCIATED CONTENT

Supporting Information

The Supporting Information is available free of charge at https://pubs.acs.org/doi/10.1021/acsphotonics.2c00790.

> Demonstration of the CPA-lasing effect via counter-propagating wave interaction and discussion of CPA-lasing at Fano resonances (PDF)

AUTHOR INFORMATION

Corresponding Author

Denis V. Novitsky − B. I. Stepanov Institute of Physics, National Academy of Sciences of Belarus, 220072 Minsk, Belarus; ● orcid.org/0000-0003-2210-7135; Email: dvnovitsky@gmail.com

Authors

Adrià Canós Valero − Institute of Telecommunications, Riga Technical University, 1048 Riga, Latvia

Aleksandr Krotov − Institute of Telecommunications, Riga Technical University, 1048 Riga, Latvia; Saint Petersburg Electrotechnical University "LETI" (ETU), 197376 St. Petersburg, Russia

Toms Salgals − Institute of Telecommunications, Riga Technical University, 1048 Riga, Latvia

Alexander S. Shalin − Institute of Telecommunications, Riga Technical University, 1048 Riga, Latvia; Faculty of Physics, M.V. Lomonosov Moscow State University, 119991 Moscow, Russia; Center for Photonics and 2D Materials, Moscow Institute of Physics and Technology, 141700 Dolgoprudny, Russia; School of Optical and Electronic Information, Suzhou

City University, 215104 Suzhou, China; Kotelnikov Institute of Radio Engineering and Electronics, 432000 Ulyanovsk, Russia

Andrey V. Novitsky − *Department of Theoretical Physics and Astrophysics, Belarusian State University, 220030 Minsk, Belarus; ITMO University, 197101 St. Petersburg, Russia;* ⊙ orcid.org/0000-0001-9553-7318

Complete contact information is available at:
https://pubs.acs.org/10.1021/acsphotonics.2c00790

◼ REFERENCES

(1) Bender, C. M.; Boettcher, S. Real Spectra in Non-Hermitian Hamiltonians Having PT Symmetry. *Phys. Rev. Lett.* **1998**, *80*, 5243−5246.

(2) Ashida, Y.; Gong, Z.; Ueda, M. Non-Hermitian physics. *Adv. Phys.* **2020**, *69*, 249−435.

(3) Zyablovsky, A. A.; Vinogradov, A. P.; Pukhov, A. A.; Dorofeenko, A. V.; Lisyansky, A. A. PT-symmetry in optics. *Phys.-Usp.* **2014**, *57*, 1063−1082.

(4) Feng, L.; El-Ganainy, R.; Ge, L. Non-Hermitian photonics based on parity−time symmetry. *Nat. Photonics* **2017**, *11*, 752−762.

(5) El-Ganainy, R.; Makris, K. G.; Khajavikhan, M.; Musslimani, Z. H.; Rotter, S.; Christodoulides, D. N. Non-Hermitian physics and PT symmetry. *Nat. Phys.* **2018**, *14*, 11−19.

(6) Özdemir, S. K.; Rotter, S.; Nori, F.; Yang, L. Parity−time symmetry and exceptional points in photonics. *Nat. Mater.* **2019**, *18*, 783−798.

(7) Chen, W.; Kaya Özdemir, Ş.; Zhao, G.; Wiersig, J.; Yang, L. Exceptional points enhance sensing in an optical microcavity. *Nature* **2017**, *548*, 192−196.

(8) Hodaei, H.; Hassan, A. U.; Wittek, S.; Garcia-Gracia, H.; El-Ganainy, R.; Christodoulides, D. N.; Khajavikhan, M. Enhanced sensitivity at higher-order exceptional points. *Nature* **2017**, *548*, 187−191.

(9) Wiersig, J. Review of exceptional point-based sensors. *Photonics Res.* **2020**, *8*, 1457−1467.

(10) Goldzak, T.; Mailybaev, A. A.; Moiseyev, N. Light Stops at Exceptional Points. *Phys. Rev. Lett.* **2018**, *120*, 013901.

(11) Feng, L.; Wong, Z. J.; Ma, R.-M.; Wang, Y.; Zhang, X. Single-mode laser by parity time symmetry breaking. *Science* **2014**, *346*, 972−975.

(12) Hodaei, H.; Miri, M.-A.; Heinrich, M.; Christodoulides, D. N.; Khajavikhan, M. Parity-time-symmetric microring lasers. *Science* **2014**, *346*, 975−978.

(13) Qi, B.; Chen, H.-Z.; Ge, L.; Berini, P.; Ma, R.-M. Parity−Time Symmetry Synthetic Lasers: Physics and Devices. *Adv. Opt. Mater.* **2019**, *7*, 1900694.

(14) de la Perrière, V. B.; Gaimard, Q.; Benisty, H.; Ramdane, A.; Lupu, A. Electrically injected parity-time symmetric distributed feedback laser diodes (DFB) for telecom applications. *Nanophotonics* **2021**, *10*, 1309−1317.

(15) Longhi, S. PT-symmetric laser absorber. *Phys. Rev. A* **2010**, *82*, 031801.

(16) Wong, Z. J.; Xu, Y.-L.; Kim, J.; O'Brien, K.; Wang, Y.; Feng, L.; Zhang, X. Lasing and anti-lasing in a single cavity. *Nat. Photonics* **2016**, *10*, 796−801.

(17) Novitsky, D. V. CPA-laser effect and exceptional points in PT-symmetric multilayer structures. *J. Opt.* **2019**, *21*, 085101.

(18) Parto, M.; Liu, Y. G. N.; Bahari, B.; Khajavikhan, M.; Christodoulides, D. N. Non-Hermitian and topological photonics: optics at an exceptional point. *Nanophotonics* **2021**, *10*, 403−423.

(19) Deng, H.; Khajavikhan, M. Parity−time symmetric optical neural networks. *Optica* **2021**, *8*, 1328−1333.

(20) Rüter, C. E.; Makris, K. G.; El-Ganainy, R.; Christodoulides, D. N.; Segev, M.; Kip, D. Observation of Parity-Time Symmetry in Optics. *Nat. Phys.* **2010**, *6*, 192−195.

(21) Hlushchenko, A. V.; Shcherbinin, V. I.; Novitsky, D. V.; Tuz, V. R. Loss compensation symmetry in a multimode waveguide coupler. *Laser Phys. Lett.* **2020**, *17*, 116202.

(22) Hlushchenko, A. V.; Shcherbinin, V. I.; Novitsky, D. V.; Tuz, V. R. Multimode parity-time symmetry and loss compensation in coupled waveguides with loss and gain. *Phys. Rev. A* **2021**, *104*, 013507.

(23) Hlushchenko, A. V.; Novitsky, D. V.; Shcherbinin, V. I.; Tuz, V. R. Multimode PT-symmetry thresholds and third-order exceptional points in coupled dielectric waveguides with loss and gain. *J. Opt.* **2021**, *23*, 125002.

(24) Regensburger, A.; Bersch, C.; Miri, M.-A.; Onishchukov, G.; Christodoulides, D. N.; Peschel, U. Parity−time synthetic photonic lattices. *Nature* **2012**, *488*, 167−171.

(25) Kremer, M.; Biesenthal, T.; Maczewsky, L. J.; Heinrich, M.; Thomale, R.; Szameit, A. Demonstration of a two-dimensional PT-symmetric crystal. *Nat. Commun.* **2019**, *10*, 435.

(26) Wen, J.; Jiang, X.; Jiang, L.; Xiao, M. Parity-time symmetry in optical microcavity systems. *J. Phys. B: At., Mol. Opt. Phys.* **2018**, *51*, 222001.

(27) Ge, L.; Chong, Y. D.; Stone, A. D. Conservation relations and anisotropic transmission resonances in one-dimensional PT-symmetric photonic heterostructures. *Phys. Rev. A* **2012**, *85*, 023802.

(28) Shramkova, O. V.; Tsironis, G. P. Scattering properties of PT-symmetric layered periodic structures. *J. Opt.* **2016**, *18*, 105101.

(29) Witoński, P.; Mossakowska-Wyszyńska, A.; Szczepański, P. Effect of Nonlinear Loss and Gain in Multilayer PT-Symmetric Bragg Grating. *IEEE J. Quantum Electron.* **2017**, *53*, 2100111.

(30) Novitsky, D. V.; Karabchevsky, A.; Lavrinenko, A. V.; Shalin, A. S.; Novitsky, A. V. PT symmetry breaking in multilayers with resonant loss and gain locks light propagation direction. *Phys. Rev. B* **2018**, *98*, 125102.

(31) Shramkova, O. Loss-compensated active nonlinear layered structures with gain saturation. *J. Opt. Soc. Am. B* **2019**, *36*, 2038−2044.

(32) Shramkova, O. V.; Makris, K. G.; Christodoulides, D. N.; Tsironis, G. P. Nonlinear scattering by non-Hermitian multilayers with saturation effects. *Phys. Rev. E* **2021**, *103*, 052205.

(33) Novitsky, D. V.; Shalin, A. S.; Novitsky, A. Nonlocal homogenization of PT-symmetric multilayered structures. *Phys. Rev. A* **2019**, *99*, 043812.

(34) Tsvetkov, D. M.; Bushuev, V. A.; Mantsyzov, B. I. Optical-pulse dynamics under quasi-PT-symmetry. *Phys. Rev. A* **2019**, *99*, 023846.

(35) Shestakov, P. Y.; Komissarova, M. V.; Marchenko, V. F. Peculiarities of light pulse propagation in quasi-PT symmetric periodic structures. *J. Opt. Soc. Am. B* **2021**, *38*, 990−996.

(36) Novitsky, D. V.; Lyakhov, D.; Michels, D.; Redka, D.; Pavlov, A. A.; Shalin, A. S. Controlling wave fronts with tunable disordered non-Hermitian multilayers. *Sci. Rep.* **2021**, *11*, 4790.

(37) Krasnok, A.; Baranov, D.; Li, H.; Miri, M.-A.; Monticone, F.; Alú, A. Anomalies in light scattering. *Adv. Opt. Photonics* **2019**, *11*, 892−951.

(38) Krasnok, A.; Alu, A. Active Nanophotonics. *Proc. IEEE* **2020**, *108*, 628−654.

(39) Novitsky, A.; Lyakhov, D.; Michels, D.; Pavlov, A. A.; Shalin, A. S.; Novitsky, D. V. Unambiguous scattering matrix for non-Hermitian systems. *Phys. Rev. A* **2020**, *101*, 043834.

(40) Terekhov, P. D.; Baryshnikova, K. V.; Greenberg, Y.; Fu, Y. H.; Evlyukhin, A. B.; Shalin, A. S.; Karabchevsky, A. Enhanced absorption in all-dielectric metasurfaces due to magnetic dipole excitation. *Sci. Rep.* **2019**, *9*, 3438.

(41) Barhom, H.; Machnev, A. A.; Noskov, R. E.; Goncharenko, A.; Gurvitz, E. A.; Timin, A. S.; Shkoldin, V. A.; Koniakhin, S. V.; Koval, O. Y.; Zyuzin, M. V.; Shalin, A. S.; Shishkin, I. I.; Ginzburg, P. Biological Kerker Effect Boosts Light Collection Efficiency in Plants. *Nano Lett.* **2019**, *19*, 7062−7071.

(42) Canós Valero, A.; Kislov, D.; Gurvitz, E. A.; Shamkhi, H. K.; Pavlov, A. A.; Redka, D.; Yankin, S.; Zemánek, P.; Shalin, A. S. Nanovortex-Driven All-Dielectric Optical Diffusion Boosting and Sorting Concept for Lab-on-a-Chip Platforms. *Adv. Sci,* **2020**, *7*, 1903049.

(43) Terekhov, P. D.; Evlyukhin, A. B.; Redka, D.; Volkov, V. S.; Shalin, A. S.; Karabchevsky, A. Magnetic Octupole Response of Dielectric Quadrumers. *Laser Photonics Rev.* **2020**, *14*, 1900331.

(44) Shamkhi, H. K.; Sayanskiy, A.; Valero, A. C.; Kupriianov, A. S.; Kapitanova, P.; Kivshar, Y. S.; Shalin, A. S.; Tuz, V. R. Transparency and perfect absorption of all-dielectric resonant metasurfaces governed by the transverse Kerker effect. *Phys. Rev. Mater.* **2019**, *3*, 085201.

(45) Liberal, I.; Engheta, N. Near-zero refractive index photonics. *Nat. Photonics* **2017**, *11*, 149−158.

(46) Kinsey, N.; DeVault, C.; Boltasseva, A.; Shalaev, V. M. Near-zero-index materials for photonics. *Nat. Rev. Mater.* **2019**, *4*, 742−760.

(47) Reshef, O.; De Leon, I. D.; Alam, M. Z.; Boyd, R. W. Nonlinear optical effects in epsilon-near-zero media. *Nat. Rev. Mater.* **2019**, *4*, 535−551.

(48) Hsu, C. W.; Zhen, B.; Stone, A. D.; Joannopoulos, J. D.; Soljačić, M. Bound states in the continuum. *Nat. Rev. Mater.* **2016**, *1*, 16048.

(49) Azzam, S. I.; Kildishev, A. V. Photonic Bound States in the Continuum: From Basics to Applications. *Adv. Opt. Mater.* **2021**, *9*, 2001469.

(50) Sadreev, A. F. Interference traps waves in an open system: bound states in the continuum. *Rep. Prog. Phys.* **2021**, *84*, 055901.

(51) Liu, C.; Liu, S.; Liu, H.; Gao, R. Bound states in the continuum in a waveguide system of zero-index materials with a defect embedded. *J. Phys. D: Appl. Phys.* **2021**, *54*, 385101.

(52) Monticone, F.; Doeleman, H. M.; Den Hollander, W.; Koenderink, A. F.; Alù, A. Trapping Light in Plain Sight: Embedded Photonic Eigenstates in Zero-Index Metamaterials. *Laser Photonics Rev.* **2018**, *12*, 1700220.

(53) Duggan, R.; Ra'di, Y.; Alù, A. Temporally and Spatially Coherent Emission from Thermal Embedded Eigenstates. *ACS Photonics* **2019**, *6*, 2949−2956.

(54) Sakotic, Z.; Krasnok, A.; Cselyuszka, N.; Jankovic, N.; Alù, A. Berreman Embedded Eigenstates for Narrow-Band Absorption and Thermal Emission. *Phys. Rev. Appl.* **2020**, *13*, 064073.

(55) Sakotic, Z.; Krasnok, A.; Alú, A.; Jankovic, N. Topological scattering singularities and embedded eigenstates for polarization control and sensing applications. *Photonics Res.* **2021**, *9*, 1310−1323.

(56) Castaldi, G.; Moccia, M.; Galdi, V. Synthesizing quasi-bound states in the continuum in epsilon-near-zero layered materials. *Appl. Phys. Lett.* **2021**, *119*, 171110.

(57) Novitsky, D. V.; Shalin, A. S.; Redka, D.; Bobrovs, V.; Novitsky, A. V. Quasibound states in the continuum induced by PT symmetry breaking. *Phys. Rev. B* **2021**, *104*, 085126.

(58) Wu, T.; Gurioli, M.; Lalanne, P. Nanoscale Light Confinement: the Q's and V's. *ACS Photonics* **2021**, *8*, 1522−1538.

(59) Koshelev, K.; Lepeshov, S.; Liu, M.; Bogdanov, A.; Kivshar, Y. Asymmetric Metasurfaces with High-Q Resonances Governed by Bound States in the Continuum. *Phys. Rev. Lett.* **2018**, *121*, 193903.

(60) Song, Q.; Hu, J.; Dai, S.; Zheng, C.; Han, D.; Zi, J.; Zhang, Z. Q.; Chan, C. T. Coexistence of a new type of bound state in the

continuum and a lasing threshold mode induced by PT symmetry. *Sci. Adv.* **2020**, *6*, No. eabc1160.

(61) Novotny, L.; Hecht, B. *Principles of Nano-Optics*; Cambridge University Press: New York, 2006.

(62) Sakotic, Z.; Stankovic, P.; Bengin, V.; Krasnok, A.; Alú, A.; Jankovic, N. Unveiling Topological Charges and Their Manipulation in Electronic Circuits. 29 March 2022, arXiv:2203.15196 (accessed Aug 22, 2022).

(63) Guo, A.; Salamo, G. J.; Duchesne, D.; Morandotti, R.; Volatier-Ravat, M.; Aimez, V.; Siviloglou, G. A.; Christodoulides, D. N. Observation of PT-Symmetry Breaking in Complex Optical Potentials. *Phys. Rev. Lett.* **2009**, *103*, 093902.

(64) Peng, B.; Özdemir, S. K.; Rotter, S.; Yilmaz, H.; Liertzer, M.; Monifi, F.; Bender, C. M.; Nori, F.; Yang, L. Loss-induced suppression and revival of lasing. *Science* **2014**, *346*, 328−332.

(65) Longhi, S.; Della Valle, G. Loss-induced lasing: new findings in laser theory?. 12 May 2015, arXiv:1505.03028 (accessed 2022-08-22).

65

3-PAPER: Data Acquisition and Processing Algorithm for Total and Static Pressure Measurement System

Proceeding Paper

Data Acquisition and Processing Algorithm for Total and Static Pressure Measurement System [†]

Alexander Krotov [1,2,*], Sergey Tarasov [2], Andrey Lunev [2], Ruslan Borisov [3] and Darya Kushevarova [2]

[1] Institute of Telecommunications, Riga Technical University, LV-1048 Riga, Latvia
[2] Department of Photonics, Faculty of Electronics, St. Petersburg Electrotechnical University "LETI", 197022 St. Petersburg, Russia
[3] Department of Aviation Engineering, Faculty of Flight Operations and Air Traffic Control, Ulyanovsk Institute of Civil Aviation, 432071 Ulyanovsk, Russia
* Correspondence: alexan.krotov@gmail.com
† Presented at the 9th International Electronic Conference on Sensors and Applications, 1–15 November 2022; Available online: https://ecsa-9.sciforum.net/.

Abstract: In aviation measurement of static and total pressure is widely used to determine the flight conditions. Results of pressure measurements are used to monitor flight attitude, equivalent speed, Mach number, vertical velocity etc. The algorithm for data acquisition and processing for developed pressure measurement system is presented in this paper.

Keywords: pressure sensor; linear photodetector array; sensing element; centroid method

1. Introduction

A variety of systems for the monitoring of aircraft flight parameters based on different working principles exists today [1–10]. Perspective and existing systems show high measurement speed and efficiency of sensors based on optical methods of information conversion [6–8]. The working principle of optical pressure sensors is based on determination of the position of light spots on the surface of a Photodetector Array (PA). The light spots are formed by Light Emitting Diodes (LED). The LEDs are rigidly attached to the frame of the device. The PA is attached to a pressure sensitive element such as an elastic membrane. The membrane is strained by the change of pressure which leads to a displacement of the light spot. Thus, the change of measured value is proportional to the light spot displacement relative to the initial position.

One of the disadvantages of this type of device is that the information about the current optical spot coordinate is obtained discretely with a period equal to the time interval required for polling all the PA elements. The minimum time interval between PA polls is limited by the technical capabilities of the PA. In addition, if a detector is mounted to a membrane there is a decrease in the dynamic stability of the system.

The developed optical pressure sensor is devoid of these drawbacks. The shutters with n slots are attached to the membranes instead of the detector arrays. This allows n optical spots to form on the surface of the PA. All n optical spots are displaced when the static and (or) total pressure changes. The photodetectors of the PA are polled sequentially. An electrical signal is formed at the output of the PA during the polling cycle. The signal amplitude reflects the distribution of optical power along the PA. The maxima in the output signal from the PA correspond to the positions of the optical spots. By utilizing the shutter with n slots we are able measure pressure n times in one polling cycle. The sensor has a higher dynamic stability as the PA is rigidly fixed to the sensor body. The dimensions of the device are also reduced as the shutters are more compact than the PA.

2. Data Acquisition Algorithm

The conversion of the electrical signals (Vaut) from the PA into a digital code is performed by an analog-to-digital converter (ADC) built in the microcontroller. Acquired data are then processed by the microcontroller and the results are transmitted to a personal computer via the Universal Asynchronous Receiver-Transmitter (USART) interface. The sequence of control clock (CLK) pulses determines the appearance of a signal at the PA output (Figure 1). Therefore, the sampling rate of all pixels of the line is determined using the following condition: each subsequent control Read-Out Gate (ROG) pulse must appear after the passage of 2087 CLK pulses.
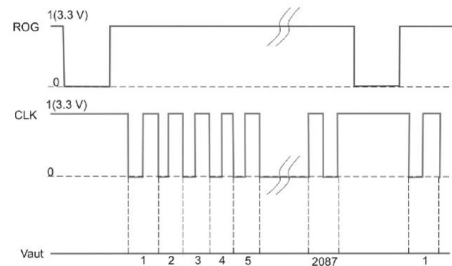
Figure 1. Diagram of control pulses.

The STM32 microcontroller algorithm can be divided into two infinite parallel loops.
Loop No 1:

1. The Startup of the ADC channel is performed by a trigger from the timer. The data are then saved in the array with the use of direct memory access (DMA).
2. The CLK signal is inverted by an ADC interrupt handler after each conversion. (This approach to forming CLK pulses allows acquisition of a data array of 4174 values for the PA consisting of 2087 pixels).
3. The flag of the completion of polling of the first half of the PD is set in the DMA interrupt handler after half of the data array is filled.
4. The flag of the PA polling completion is set in the DMA interrupt handler and the reset signal (ROG) is formed after the whole data array is filled.

Loop No 2:

1. Tracking the status of the polling of the first half of the PA. If the corresponding flag is set, data are copied to the other memory region and then processed.
2. If the averaging is not performed the results are transmitted via the USART interface.
3. Tracking the status of the polling of the whole PA. If the corresponding flag is set, the data are copied to the other memory region and then processed.
4. If the averaging is not performed the results are transmitted via the USART interface.
5. The results are averaged and then transmitted via USART.

3. Data Processing Algorithm

The algorithm for calculating the coordinates of the light spot uses the centroid-method and is implemented as follows. First, the positions of pixels $N_{\max\_n}$ corresponding to local signal maxima are determined. Then an area of M pixels around the local maxima is selected. The value of M is chosen in such a way as to include all pixels around the maximum signals

which are noticeably higher than the background noise level. The coordinate of the signal maximum is then calculated according to the following formula:

$$MAX_n = \frac{\sum_{i=N_{\max\_n}-\frac{M}{2}}^{N_{\max\_n}+\frac{M}{2}} A_i i}{\sum_{i=N_{\max\_n}-\frac{M}{2}}^{N_{\max\_n}+\frac{M}{2}} A_i} \tag{1}$$

where MAX_n—coordinate of the maximum of n-th light spot expressed in the pixel number, A_i—signal amplitude from i-th pixel in vicinity of n-th optical spot, $N_{\max\_n}$—number of pixels having a maximum amplitude around the n-th optical spot. The elastic membrane deforms as a result of pressure change. The deformation of the membrane leads to displacement of the optical spots. Computation of the new coordinates of the optical spots using (1) allows determination of the change of pressure relatively to some reference value according to the formula:

$$\Delta P_{stn}(t) = k_n (MAX_n(t) - MAX_n(0)) \tag{2}$$

where $\Delta P_{stn}(t)$—current value of pressure change, $MAX_n(t)$—coordinate of the n-th optical spot maximum at time t, $MAX_n(0)$—coordinate of the n-th optical spot maximum at reference pressure, k_n—calibration constant.

4. Conclusions

When using the presented algorithm for collecting and processing information, the measurement speed of the developed pressure sensor is determined using the repetition rate of the control pulses. The proposed solution provides reduced error values when calculating the altitude and speed parameters of the aircraft. Averaging of the results from one complete poll of PA (n spots) increases accuracy by $n^{1/2}$ times. On the other hand, when measurement speed is more important, the value of pressure can be obtained from the position of one optical spot.

The high speed of the measuring system in the future will make it possible to apply algorithms that provide compensation for various kinds of destabilizing factors (interference, vibrations, shock effects, etc.) that arise during the operation of an aircraft.

References

1. Fraden, J. *Handbook of Modern Sensors*; Springer: New York, NY, USA, 2003.
2. Auersvald, J.; Draxler, K.; Sipo, M. A Low-cost Aerometric Sensor system for Sport Aviation. *J. Electr. Eng.* **2019**, *4*, 295–302. [CrossRef]
3. Auersvald, J.; Draxler, K. Aerometric System for General Aviation. In Proceedings of the International Conference on Military Technologies (ICMT), Brno, Czech Republic, 19 May–21 May 2015; pp. 1–6.

4.   Almazov, V.V.; Makarov, N.N.; Sorokin, M.Y. Evaluation of Performance of Aerometric Systems. *Izv. Samara Sci. Cent. Russ. Acad. Sci.* **2017**, *1*, 385–390.
5.   Philippe, J.; De Paolis, M.V.; Arenas-Buendia, C.; Henry, D.; Coustou, A.; Rumeau, A.; Aubert, H.; Pons, P. Passive and Chipless Packaged Transducer for Wireless Pressure Measurement. In *Sensors and Actuators A: Physical*; Elsevier: Amsterdam, The Netherlands, 2018; pp. 753–762.
6.   Soldatkin, V.V.; Soldatkin, V.M.; Derevyankin, V.P. Models of Signals, Characteristics, and Errors of the Axisymmetric Multifunction Air Pressure Sensor for Aircraft Aerometric Systems. *Russ. Aeronaut* **2021**, *64*, 105–110. [CrossRef]
7.   Jena, S.; Gupta, A. Embedded Sensors for Health Monitoring of an Aircraft. In *Sensors for Automotive and Aerospace Applications. Energy, Environment, and Sustainability*; Bhattacharya, S., Agarwal, A., Prakash, O., Singh, S., Eds.; Springer: Berlin/Heidelberg, Germany, 2019.
8.   Leitzke, J.P.; Della Mea, A.; Faller, L.M.; Mühlbacher-Karrer, S.; Zangl, H. Wireless Differential Pressure Measurement for Aircraft. *Measurement* **2018**, *122*, 459–465. [CrossRef]
9.   Kwon, H.; Park, Y.; Shin, C.; Kim, J.H.; Kim, C.G. In-Flight Strain Monitoring of Aircraft Tail Boom Structure Using a Fiber Bragg Grating Sensor Based Health and Usage Monitoring System. *Int. J. Aeronaut. Space Sci.* **2021**, *22*, 567–577. [CrossRef]
10.   Antonets, I.V.; Gorshkov, G.M.; Borisov, R.A. Datchik Aerometricheskikh Davleniy (Aerometric Pressure Sensor). RU Patent 2653596, G01L7/00, 11 May 2018.

4-PAPER: Methodology for the Static and Total Pressure Sensor Development Based on Elastic Sensing Elements and Linear CCD Matrices

Methodology for the Static and Total Pressure Sensor Development Based on Elastic Sensing Elements and Linear CCD Matrices

Ruslan Borisov[1], Ivan Antonec[1], Aleksandr Krotov[2, 3], Sergey Tarasov[2], Vjaceslavs Bobrovs[3]

Abstract – *Based on the Airworthiness Standards requirements, accuracy of air pressures measurements is strict. The air flow static and total pressure measurement instrumental errors should not exceed 0.02% and 0.05% of the measurement range with 95% probability. These requirements are ensured by original aerometric pressure sensor based on one-dimensional high sensitivity charge-coupled device considered in this article. Non-contact reception of signal and sensor vacuum durability has significantly increased the efficiency of measurement processes. The algorithm for calculating elastic sensitive elements basic design parameters in the most of entire standard size range and technical secondary transducer capabilities is considered in the article. The results of the experiments conducted by the authors and the results of the authors experimental studies listed in the references have confirmed the adequacy of theoretical methods for calculating the parameters of elastic elements for pressure sensors.* **Copyright © 2022 Praise Worthy Prize S.r.l. - All rights reserved.**

Keywords: *Aerometric Pressure Sensors, Elastic Sensing Element, Incident Air Flow Pressure, Linear CCD*

Nomenclature

a,b	Coefficients depending on the membrane profile's shape and the material nature
c_i	Measured value of the flow speed at the i measurement step for full pressure [m/s]
c_{max}	Maximal flow speed
D_{ci}	Discreteness of the c_i measurement at the i measurement step
D_{Hi}	Discreteness of the H_i measurement at the i measurement step
E	Young's modulus [Pa]
h	Thickness of the membrane [mm]
H_i	Measured value of the height at the i measurement step for static pressure [Pa]
H_{min}	Minimal membrane's depth [mm]
i	Measurement step
k	Safety factor
$k1$	Geometrical membrane's coefficient
$k2$	Geometrical membrane's coefficient
P	Static pressure [Pa]
p	Pressure at a given center deflection of the membrane [Pa]
P^*	Total pressure [Pa]
P_0	Pressure at the reference height [Pa]
P_{dinmax}	Maximal dynamic pressure at c_{max} speed
P_i	Measured pressure at the i measurement step [Pa]
P_{max}	Limit pressure on the membrane [Pa]
R	Membrane's radius in mm
$r0$	Flat part membrane's radius
S	Secondary transducer sensitivity [mm]

T_0	Temperature at zero height [K]
z	Depth of the corrugation in mm
α	Parameter depending on the shape of the membrane
μ	Poisson's ratio
η, ξ	Coefficients depending on the profile shape and the rigid center radius
ρ	Dimensionless membrane radius
σ_{max}	Maximum membrane's stresses at the maximum working load
τ	the temperature gradient in [°C/m]
ω_0	Membrane's center deflection [mm]
ω_{0i}	Deflection of the membrane at the i measurement step [mm]
ω_{0max}	Maximum deflection of the membrane's rigid center [mm]
ω_{max}	maximum deflection of the membrane [mm]
ADC	Air Data Computer
CCD	Photodetector line (Charge-Coupled Device)
ESE	Elastic Sensing Elements
USART	Universal Synchronous/Asynchronous Receiver/Transmitter

I. Introduction

The aircraft altitude and the speed control system are a set of control surfaces and related devices and mechanisms, in particular, mechanical, hydraulic, electrical, and electronic computing [1]-[36]. This system is to ensure selection and maintenance of altitude, horizontal and vertical flight speeds in non-automatic,

semi-automatic, automatic and combined control modes. In the general case, altitude-speed parameters control system includes an Air Data Computer (ADC), an aircraft flight complex, control system actuators, information display facilities and aircraft controls, which help to issue control action to the control system actuators. Moreover, during the flight, the pilot selects the control mode and influences the altitude and speed parameters such as flight altitude stabilization, flight speed stabilization, vertical flight speed stabilization modes, automatic reaching a given altitude, automated acceleration or deceleration to a given flight speed etc. It should be noted that there are control modes in which flight complex generates director control commands while the flight complex does not participate in aircraft control (or its participation is limited) but it only generates commands for the pilot. Modern static and total pressure sensors are part of the ADC designed to calculate the altitude-speed parameters of the aircraft flight. ADC includes an air signal computer that needs the following information: P * - total pressure, P - static pressure, T * - stagnant temperature of the external flow. In ADC, total and static pressure sensors are sources of primary information [23]. That predetermines a significant dependence of the metrological characteristics of the ADC on static and total pressures measuring accuracy (under the influence of destabilizing factors) and on maintaining the specified accuracy over time. For example, one of the widely used ADC is GDS 74A, which is part of the GARMIN G 1000 avionics system installed on DA-40, DA-42 and Cessna aircraft. As a source of air flow static and total pressures parameters, information generator-type sensors (they are also known as frequency pressure sensors) are used. This analysis of the pressure sensors currently used as part of the ADC made shows that the generator-type pressure sensors based on the frequency method of information conversion are among the most common in aviation. The frequency converters used on board the aircraft convert the oscillations of the Elastic Sensitive Element (ESE) - cylindrical resonator, into the pulse repetition rate. This information conversion method has a relatively high noise immunity. Total and static pressure in digital ADC is measured by resonant or frequency pressure sensors. In [24], a sensor based on the use of ESE oscillations (mechanical resonator) description operation principle has been presented. Since the middle of the last century, British company Solatron has been dealing with static and total pressure sensors, which has currently developed and manufactures sensors for ADC military and civil aircraft. However, frequency sensors have a number of significant drawbacks: temperature error, non-linear distortion, and relatively high power consumption.

Resonant type pressure sensors or frequency sensors have significant errors caused by temperature changes and amount to up to 7% of the measured pressure range.

In order to compensate for the temperature errors of generator-type pressure sensors, corrections are used, whose values are calculated depending on the ESE

temperature. The cylindric ESE manufacturing technology also has significant drawbacks. Their rejection in the production process is about 70%. Due to the popularity of pressure sensors based on the frequency information conversion method there are research and development to modernize and improve this method [25]-[27]. Along with ESE made in the form of cylindrical resonators, there is a large class of ESE based on flat or corrugated membranes. The fundamental foundations for the research and development of membrane ESEs have been laid by Feodosyev V. [6], [7], Panov D. [5], Felikson I.[15], Andreeva L.E. [8]-[10]. In addition, a large number of works authors are devoted to research in this area [17], [28]-[30]. Corrugated membrane ESEs are most widely used since they can obtain a significant deflection under pressure within the elastic properties limits. Dispersion hardened alloys with low values of elastic imperfections are mainly used for the membrane ESEs manufacture. In addition, they have the independence of their elasticity modulus from the ambient temperature and high elastic and strength properties, high relaxation resistance after exposure to vibration. These alloys include beryllium bronzes $CuBe2Ni(Co)$, $CuBe2NiTi$, which surpass many high-quality steels in strength and elastic properties. The hysteresis [31], [32] of beryllium bronze elastic elements is relatively small in comparison with other materials that are used as ESE pressure sensors and it is approximately 0.4-1%. The significant share of disadvantages ESE membrane use as part of total and static pressure sensors can be divided into two groups. The first group of disadvantages associated with the contact effect between ESE and the secondary pressure converter: friction between the ESE elements and the secondary converter, the measurement force on the ESE from the secondary converter elements. In addition, the size of the rigid center of the membrane ESE can also be attributed to this group. The second group of disadvantages is associated with the magnitude of equivalent stresses: residual deformations, elastic effect, elastic hysteresis, fatigue failure of the ESE. The above drawbacks manifest themselves as follows: in the form of a deviation from the set zero value, hysteresis phenomena, destruction of places of contact between the primary and secondary pressure transducers. The destruction of the places of contact interaction between the transducers is especially acute when using ESE sensors based on the structures "silicon on sapphire". The influence of hysteresis phenomena can cause distortion in barometric altimeters readings. Therefore, with a relatively fast ascent and descent of the aircraft the readings of instruments at the same height may turn out to be different. Both the first and the second groups of disadvantages are connected largely with the design and functionality of the secondary pressure converter. The first group of shortcomings is eliminated by using non-contact methods for converting the ESE deformation into an analog or digital signal. The second group of disadvantages can be solved not only by special ESE technological manufacturing operations but

also by equivalent stress minimization with highly sensitive secondary pressure transducers. The non-linearity of the static characteristics of membrane ESEs (unlike bellows, tubular springs) has predetermined their widespread use as primary pressure transducers as part of mechanical and electrical devices for indicating altitude and speed parameters to the aircraft crew. This is since the change pattern in static and the total pressures depend on the altitude and speed parameters of the aircraft is non-linear. At the same time, the non-linearity of the ESE membrane characteristics and the non-linearity of the change in the gradient of the measured pressures along the height are strictly opposite, making it possible to obtain a sensor output signal close to linear. Aerometric sensors of total and static pressure are the sources of ADC primary information, which determines the altitude and speed parameters of the aircraft. This determines significant dependence of the ADC metrological characteristics of static and total pressures under the influence of destabilizing factors and on specified accuracy preservation over time. The analysis of the metrological characteristics of ESE aerometric pressure sensors known designs of various types, shapes and materials [1] and secondary sensors [2] used with them has allowed identifying practical tendencies for their improvement. Frequency sensors in which the natural frequency of oscillations of a mechanical resonator changes depending on the value of the measured pressure for measuring total and static pressures are widespread in aviation. Frequency sensors have several significant disadvantages of which singles out the temperature error, nonlinear distortions and relatively high-power consumption. Resonant frequency pressure sensors using silicon crystals have low sensitivity and significant hysteresis phenomena. Pressure sensors in which the ESE deformation is converted into a digital signal due to the spatial distribution of the light field practically do not have these disadvantages. The specified principle allows increasing the accuracy and expanding the measurement range of aerometric pressure sensors. Original aerometric pressure sensors using linear Charge-Coupled Device (CCD), whose high sensitivity requires minimal deformation of the ESE, have been developed.

Deformation minimization allows getting rid of several methodological errors: permanent deformation, nonlinearity, imperfections of elastic material, temperature fluctuations, linear acceleration effects, vibration effects, material properties over time changes, etc. Non-contact information reception and information system vacuum durability significantly increase the efficiency of measurement processes. A significant power consumption decrease is noted.

In the second section of this article the original design of the pressure sensor considered, the algorithm for calculating elastic sensitive elements, the simulation parameters in the ANSYS environment and the experimental setup are described. In third section the theoretical approaches of the optical pressure sensors construction are shown and the analyses of the correctness of the approaches are described. In the fourth section, the results of simulations and experiments are presented. Section five discusses the results obtained. In section six, the conclusions are presented.

II. Methods and Materials

II.1. Static and Total Pressure Transducer Using Optical Information Conversion Method

The operation principle of the pressure sensor using the optical method of converting information [2] is illustrated by the device diagram shown in Figure 1. The device contains shell 1 with two holes respectively for measuring static and total pressures. Membranes 2 and 3 of the ESE (aneroid box) are spaced in height and hermetically sealed along the perimeter to the body. A vacuum space is created in the gap between the membranes. Inside the gap, a radiation source 5 and two shutters 7 with slots 8 are attached to the post 4. Two CCDs 6 are attached to two membranes 3 located above and below the radiation source. In the initial state, membranes 2 and 3 of the elastic sensitive element occupy a certain position. The luminous flux from the radiation source 5 is converted into optical spots by the cuts 8 of the shutters 7. Optical spots are focused on CCD 6 fixed to the upper 2 and lower membranes 3. In the linear CCDs, pixels are located along one coordinate.

These devices operation principle consists in the formation of an electric signal proportional to the absorbed optical energy inside each pixel. This is achieved due photosensitive p-n junction through which the photodetector element capacitor is discharged [3], [4]. The higher the optical power falling on the pixel is, the greater the photodiode current is, and therefore faster the capacitor will discharge. The residual charges of the pixel capacitors are read at the end of the measurement cycle. When the static and (or) total pressures change the elastic sensitive element membranes 2 and 3 are deformed. While the CCD 6 fixed to the upper 2 and lower membranes 3 are displaced causing optical spots shift from the radiation source 5 through the slots of 8 shutters. When the pixels are sequentially polled, an electrical signal will be formed, in which the time change of amplitude shows the optical power distribution in the photodetector matrix.
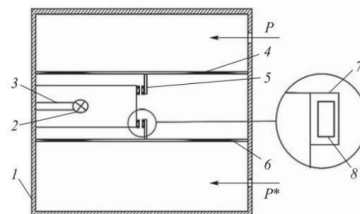

Fig. 1. Pressure sensor using optical information conversion method

In other words, signals proportional to the static and total pressures will be formed at the output of the photodetectors. Proposed pressure sensor with a temperature sensor allows calculating all the listed aerometric parameters.

II.2. Experimental Methods

II.2.1. Elastic Sensitive Elements Parameters Calculation for Static and Total Pressure Sensors

The algorithm for calculating an elastic sensitive element developed on the C++ [12] is described below.
1. Input of initial data.
1.1. Material and dimensions.
1.1.1. ESE material: E, μ (Poisson's ratio).
1.1.2. Geometric dimensions and profile of the ESE: $R, h, r0, z$, amount of corrugations n.
1.2. Secondary converter sensitivity threshold S.
1.2. The choice of the design scheme.
2.2.1. Static pressure sensor.
2.2.2. Full pressure sensor.
3. Ambient conditions during measurement:
3.1. If item 2.2.1 is selected, enter $P_0, R, T_0, \tau, H_{min}$ or P_{max}.
3.2. If item 2.2.2 is selected, enter P_0, ρ, c_{max} or $P_{din\ max}$.
4. Solution.
4.1. Coefficients calculation: $k1, k2, \alpha, a, b$ [9 p. 258 - 266], η, ξ [7 p. 291].
4.2. If item 2.2.1 is selected, calculation storing the values P_i, ω_{0i}, H_i and D_{Hi} in the data array for i from 1 to $i_{max} = \omega_{0max} /S$ where, $\omega_{0max} = f(P_{max})$.
4.3. If item 2.2.2 is selected, calculation storing the values P_i, ω_{0i}, c_i and D_{ci} in the data array for i from 1 to $i_{max} = \omega_{max} /S$ where, $\omega_{max} = f(P_{din\ max})$.
5. Output data.
5.1. Getting graphical dependencies:
5.1.1. If item 2.1 is selected. $\omega_0 = f(P)$, $\omega_0 = f(H)$, $D_H = f(H)$.
5.1.2. If item 4.2 is selected. $\omega_0 = f(P_{din})$, $\omega_0 = f(s)$, $D_c = f(s)$.
5. 2. Output of values to a table containing (Fig. 6):
5.2.1. If item 4.1 is chosen: $i, P_i, \omega_{0i}, H_i, D_{Hi}$.
5.2.2. If item 4.2 is chosen: $i, P_i, \omega_{0i}, c_i, D_{ci}$.
6. Analysis of the obtained results.
6.1. If D_{Hi} (D_{ci}) does not provide required measurement accuracy (in accordance with requirements of Airworthiness Standards) then go to step 2.
7. Saving the results to a text file.

This is followed by the calculation of the maximum stresses σ_{max} at the maximum working load and the safety factor k [13], [14]. Then it is followed by verification of condition for ensuring optimal operating stresses $\sigma_{max} \leq [\sigma_{0,005}]$ and the safety factor $k > [k]$ (where $[k]$ is the standard safety factor) by the finite element method using the ANSYS software package. If $\sigma_{max} \geq [\sigma_{0,005}]$ or $k < [k]$ then it is necessary to go to algorithm item 1.1. This method is widely used in material researches [19]-[22].

The standard safety factor $[k]$ is based on the existing operating experience of elastic sensitive elements. In general industry-wide [k] = 1.3 - 2.2 are used.

II.2.2. Elastic-Plastic Membranes Deformations Simulation by the Finite Element Method

For determining the maximum stresses σ_{max} and safety factors k via ANSYS Design Modeler software 2D models of ESE have been developed. Their geometric dimensions are presented in Table I.

This is followed by transferring geometric models to the ANSYS Mechanical module and creating a mesh model.

After these boundary conditions setting is necessary: fixed support at the edges of the corrugated membrane (Z-axis), from above (Y-axis) there is a uniformly distributed pressure of 0.107 MPa (for a static pressure sensor) and 0.131 MPa (for a total pressure sensor) with step of load application 0.005 MPa.

II.2.3. Original Pressure Sensor Experiments

Reached results reliability has been assessed with experimental data obtained in [8]-[10] and the data obtained by the authors during original pressure sensor experiments (Figs. 2).

Experimental studies have been carried out in accordance with a typical method for collecting and processing experimental results. The considered sensor (Fig. 2(b)) basis is a linear CCD photodetector 2. The accuracy of measurements using such structures depends on the geometric dimensions and the distance between the pixels of the photodetector as well as the methods of control and processing of signals coming from the photodetector.

Distance between photodetector pixels has a significant effect on the measurement accuracy.

STM32F4 series microcontrollers control program, which provides measurement of linear displacements on 1D CCD matrix [18], has been developed. Program provides to control electrical pulses generation for the ILX554B type photodetector and the incoming electrical signals conversion into a digital code followed by its mathematical processing and obtained results output through the USART interface.

TABLE I
MATERIAL AND GEOMETRIC DIMENSIONS
OF ELASTIC SENSITIVE ELEMENTS

№ ESE	ESE material	ESE sideview	R, mm	h, mm	H, mm	n, pcs.
1	CuBe2NiTi Bronze	Trapezoidal	35,98	0,13	1,088	4
2	CuBe2Ni(Co) Bronze	Sinusoidal	25	0,22	0,75	3
3	CuBe2Ni(Co) Bronze	Sinusoidal	23,25	0,145	0,26	6
4	CuBe2NiTi Bronze	Sinusoidal	24,75	0,135	0,4	12
5	CuBe2Ni(Co) Bronze	Serrated	27,74	0,15	0,54	5
6	CuBe2Ni(Co) Bronze	Sinusoidal	24,92	0,13	0,42	8

(a)

(b)
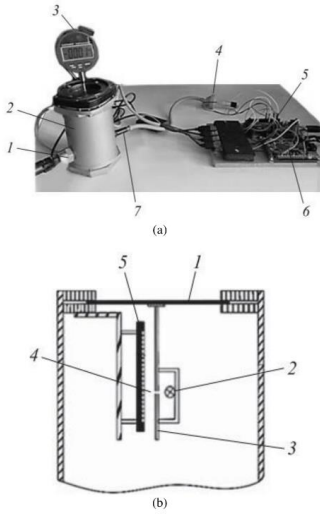
Figs. 2. Experimental setup: (a) photo of the setup, (b) design of the setup sensor: 1 - ESE, 2 - photodetector, 3 - optical radiation source, 4 - shutter, 5 – slot

Program significantly increases measurement accuracy of linear ESE displacement sensor using optical converters since polling double analog-to-digital conversion on one pixel. During the experiment, two elastic sensitive elements No. 5 and No. 6 (Figs. 3) have been used.

(a)

(b)
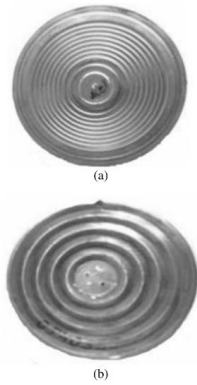
Figs. 3. Photos of experimental samples: (a) ESE No. 6, (b) ESE No. 7

III. Theory and Calculations

III.1. Elastic Sensitive Element Calculating Method Development Considering the Secondary Transducer Functionality and the Regularity Changes in the Measured Physical Quantity

The first works presenting a method for calculating corrugated membranes were published by D. Panov [5] and V. Fedosyev [6], [7] almost 77 years ago. In the work of D. Panov, equations that allowed obtaining a static characteristic of the membrane for large static deflections with a very flat sinusoidal corrugation are derived.

However, the results of calculating static membrane deflections using these equations have differed significantly from the values of real deflections.

A significant contribution to the development of methods for static corrugated membranes calculation has been made by L. Andreeva. In her works [7]-[10] an effective method of approximate static membranes calculation with corrugation of arbitrary shape and depth is determined. The main calculated expression is [10]:

$$\frac{pR^4}{Eh^4} = \eta a \frac{\omega_0}{h} + \xi b \frac{\omega_0^3}{h^3}, \qquad (1)$$

where p is the pressure at a given center deflection of the membrane in Pa, R is the membrane radius in mm, ω_0 is the membrane center deflection in mm, E is the Young's modulus in Pa, a and b are coefficients depending on the membrane profile's shape and the material nature, η and ξ are coefficients depending on the profile shape and the rigid center radius.

Below, there is the justification of the algorithm developed by the authors, which allows considering secondary converter technical characteristics and calculating the main design parameters of elastic sensitive elements in almost the entire range of their standard sizes.

In order to consider the secondary transducer technical characteristics, the secondary transducer sensitivity threshold S should be set in mm and represent the deflection of the center of the membrane as:

$$\omega_{0_i} = Si \qquad (2)$$

where i is the measurement step, i.e. integer values from 1 to $i_{max} \approx \omega_{0max} / S$.
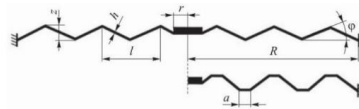

Fig. 4. Geometric dimensions of the membrane: R is the working radius of the membrane, r is the radius of the rigid center, h is the thickness of the membrane, z is the depth of the corrugation, l is the wavelength of the corrugation, φ is the angle of wave inclination, a is the width of the trapezoid (for the trapezoidal profile of the membrane)

The sensor's sensitivity threshold is understood as the minimum deflection of the membrane rigid center recorded during processing of the signal from the photodetector array. By transforming expressions (1) and (2), the following is obtained:

$$P_i = \left(\eta a \frac{Si}{h} + \xi b \frac{(Si)^3}{h^3} \right) \frac{Eh^4}{R^4}, \qquad (3)$$

where P_i is the measured pressure at the i - measurement step. The value of the height H at a given value of the static pressure P is determined by the equation:

$$H = \left(1 - \left(\frac{P}{P_0} \right)^{\tau R} \right) \frac{T_0}{\tau} \qquad (4)$$

where P_0 is the pressure at the reference height in Pa, T_0 is the temperature at zero height in K, τ is the temperature gradient in °C /m, R is the gas constant in m/° C, H is the height in m. By transforming expressions (3) and (4), the following is obtained:

$$H_i = \left(1 - \left(\frac{\left(\eta a \frac{Si}{h} + \xi b \frac{(Si)^3}{h^3} \right) \frac{Eh^4}{R^4}}{P_0} \right)^{\tau R} \right) \frac{T_0}{\tau} \qquad (5)$$

where H_i is the measured value of the height at the i - measurement step. The concept of the D_{Hi} measurement at the i measurement step for pressure sensor measurement error estimation has been introduced:

$$D_{Hi} = H_{i+1} - H_i \qquad (6)$$

This parameter has been used as a reference parameter for the pressure sensor measurement error assessment at the stage of developing an elastic sensitive element.

The pattern of D_{Hi} change at the heights working range depends on the characteristics of the elastic sensitive element. If ESE characteristic is close to linear from pressure (Fig. 5(a)) then the D_{Hi} discreteness increases significantly with height, which leads to a decrease in the measurement accuracy. If ESE characteristic is linear in height (Fig. 5(b)) then $D_{Hi} = const$. It is possible to obtain such ESE characteristics, which will ensure the specified height measurement accuracy in accordance with the requirements of Airworthiness Standards by changing the geometric dimensions of the ESE. Highly sensitive secondary transducers such as photodetectors application make it possible to increase ESE thickness, which has a positive effect on its durability, dynamic stability and allows avoiding elastic after effects. Expression (5) and (6) analysis shows that the discreteness value is influenced by ESE geometric dimensions, its profile and material as well as secondary transducer sensitivity threshold value.

The lower the secondary converter sensitivity threshold other things being equal is, the lower the discreteness value is and accordingly the higher the measurement accuracy is.
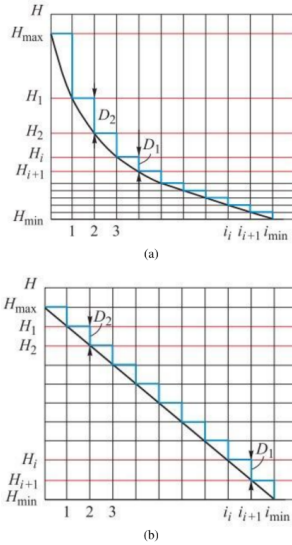
Figs. 5. Characteristic of an ESE:
(a) linear in pressure, (b) linear in height

In a similar way, the speed sensor measurement discreteness has been defined. It is known that:

$$P^* = P + \frac{\rho c^2}{2}$$
$$c = \sqrt{\frac{2(P^* - P)}{\rho}} \qquad (7)$$

Since vacuum is used as a reference pressure to measure static and total pressures in the proposed sensor ESE has an initial loaded state i.e. the membrane is bent by the amount $\omega_{0ст}$ under the action of the static pressure P. Then, by transforming expressions (3) and (7), the following is obtained:

$$c_i = \sqrt{\frac{2 \left(\left(\eta a \frac{(\omega_{0ст} + Si)}{h} + \xi b \frac{(\omega_{0ст} + Si)^3}{h^3} \right) \frac{Eh^4}{R^4} - P \right)}{\rho}}$$

and:

$$P_{dyn\,i} = \frac{\rho c_i^2}{2}$$

where $P_{dyn\,i}$ is the dynamic pressure at speed c_i:

$$P_i^* = P + \frac{\rho c_i^2}{2}$$

where, P_i^* is the total pressure at speed c_i. Discreteness of measurements Dc_i at speed c_i is:

$$D_{ci} = c_{i+1} - c_i$$

The algorithm given allows calculating ESE main design parameters practically in the standard sizes entire range and considering the technical characteristics of the secondary converter at various values and patterns of change in the measured physical quantity.

IV. Results

IV.1. Results of Static Characteristics of the ESE Numerical Simulation

Table II shows the materials used and the geometric dimensions of the studied samples of elastic sensitive elements. ESE calculation for a static pressure sensor the range of heights from - 500 m to 20,000 m has been considered. The value of the sensor sensitivity threshold has been taken as S = 0.001. Table II shows the values of the measurement discreteness by heights as well as the minimum measured pressure P_1 and the maximum deflection of the membrane ω_{0max}. ESE calculation for the total pressure sensor the speed range from 0 to 800 km/h has been considered. The sensor sensitivity threshold has been taken as S = 0.001. Table III shows the values of the measurement discreteness in terms of flight speeds.

TABLE II
DISCRETENESS OF MEASUREMENT BY HEIGHTS

№ ESE		2	3	5
Discreteness of measurement by ranges of heights	-500-0 m.	10	18	9
	0-600 m	10	18	9
	600-3000 m	12	18	9
	3000-6000 m	14	19	9
	6000-9000 m	18	19	9
	9000-12000 m	24	19	10
	12000-15000 m	35	20	11
	15000-20000 m	62	22	16
Minimum	measured pressure P_1, Pa	66,48	16,83	20,53
Maximum deflection of the membrane ω_{0max}, mm		1,024	1,245	2,085

TABLE III
DISCRETENESS OF AIRSPEED MEASUREMENT

№ ESE		1	4	6
Discreteness of airspeed measurement	50	7,40	25,00	22,00
	80	4,80	16,00	17,00
	100	3,80	13,00	12,00
	150-200	2,00	7,60	6,00
	250	1,62	6,00	5,60
	300	1,36	5,00	4,70
	350-450	1,17	3,60	4,10
	500	0,87	3,20	3,50
	550-600	0,73	2,80	2,60
	650	0,69	2,70	2,47
	700	0,65	2,50	2,33
	750	0,62	2,40	2,20
	800	0,59	2,30	2,10

IV.2. The Result of Modeling Elastic-Plastic Deformations of Membranes by The Finite Element Method Using the ANSYS Software Package

As a program result system in the form of deformation fields, stress distribution and the values of the safety factors have been obtained. Table IV shows the results of solving elastic-plastic problems by the finite element method.

IV.3. Experimental Verification of the Results Obtained

The proposed design of the sensor, the developed algorithm for control and the data processing provide deflection measurement of the membrane center with an absolute error of $\Delta = \pm 0.00036$ mm (Fig. 6). In Figs. 7, comparative results of membrane deflections are obtained by the analytical method using the ANSYS software package and experimental data are presented.

V. Discussion

The efficiency of the static pressure sensors ESE is largely determined by the implemented static characteristic [33] and in the proposed version by linear CCD at the output with a nonlinear change in pressure at the input. The pressure drop determination is required to carry out ESE deformation within the specified limits for the static pressure sensor according to the known pattern of pressure (P_H) change in with flight altitude:

$$P_H = P_0 \left(1 - \frac{\tau H}{T_0}\right)^{\frac{1}{\tau R}} \tag{8}$$

where P_0 is the pressure at zero altitude, T_0 is the temperature at zero altitude, τ is temperature gradient, R is the gas constant, H is the current altitude.

TABLE IV
FINITE ELEMENT METHOD RESULTS

№ ESE	Total deformation (ω_{0max}, mm)	Equivalent stress, MPa	Safety factor
1	4,7407	1185,2	1,01
2	1,037	705,75	1,7
3	1,58	614,52	1,95
4	2,16	716,12	1,68
5	1,364	544	2,2
6	1,676	790,36	1,52
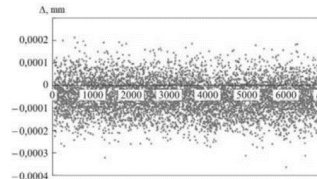
Fig. 6. The absolute error of the optical transducer ESE rigid center displacement
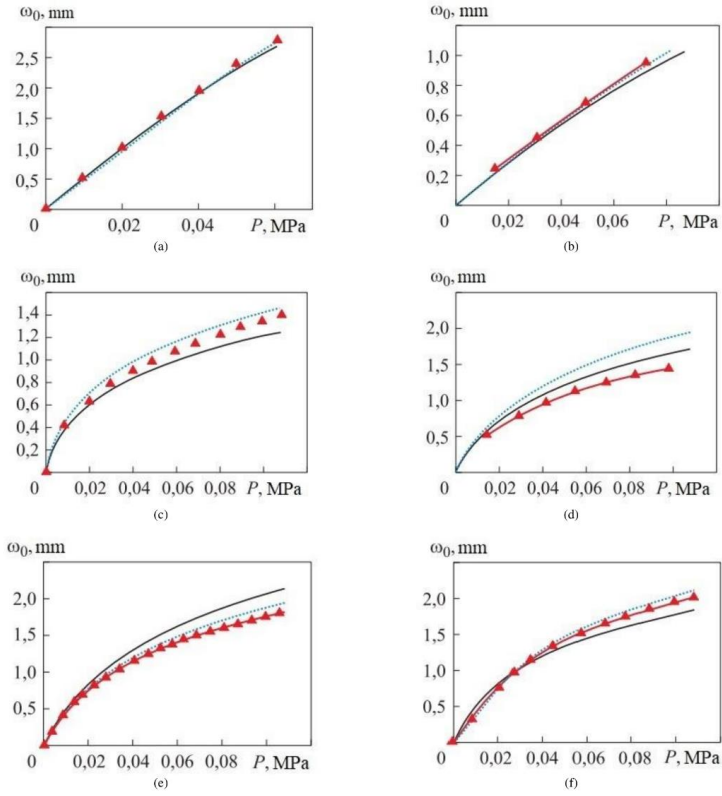
Figs. 7. Results of modeling the elastic sensitive elements static characteristics:
(a) ESE № 1, (b) ESE № 2, (c) ESE № 3, (d) ESE № 4, (e) ESE № 5, (f) ESE № 6

The maximum membrane deflection ω_{0max} is achieved at H_{min}, the minimum is ω_{0min} at H_{max}. Assuming that the characteristic of the ESE is linear in height, the equation of a straight line passing through two points with coordinates (ω_{0max}, H_{min}) and (ω_{0min}, H_{max}) is obtained:

$$H = \frac{(\omega_0 - \omega_{0max})(H_{max} - H_{min})}{\omega_{min} - \omega_{0max}} + H_{min} \qquad (9)$$

where ω_0 is the deflection of the elastic sensitive element at height H. The elastic element is deformed due to the pressure difference ΔP:

$$\Delta P = P_H - P_{vac} \qquad (10)$$

where, P_{vac} is the reference pressure (vacuum pressure).

Transforming (8) and (9) into (10), the pressure drop value required to carry out deformation within the specified limits of the ESE for the static pressure sensor has been obtained:

$$\Delta P = P_0 \times$$
$$\times \left(1 - \frac{\tau\left(\frac{\left(\begin{array}{c}(\omega_0 - \omega_{0max}) \times \\ \times (H_{max} - H_{min})\end{array}\right)}{\omega_{min} - \omega_{0max}} + H_{min}\right)}{T_0}\right)^{\frac{1}{\tau R}} + -P_{vac} \qquad (11)$$

The maximum value of the membrane deformation ω_{0max} is determined both by the geometric dimensions of the elastic sensitive element and by the technical capabilities of the secondary transducer. Similarly, the determination of the value of the pressure difference necessary for the implementation of deformation within the specified limits of the elastic sensitive element for the total pressure sensor is carried out according to the known pattern of pressure change P^* from the flight speed. Thus, the presented calculations make it possible to determine the total pressure sensor elastic element characteristics starting from the sensitivity of the secondary sensor. An aerometric pressure sensor characterized by application of CCD has been used as a secondary measuring transducer. Optical method applied as a secondary aerometric pressure transducer provides contactless interaction between the primary and secondary transducers of the sensor. The high sensitivity of CCD helps to minimize elastic sensing element deformation by providing minimum values of equivalent stresses and high values elastic element safety factor.

A method for elastic sensitive element calculating considering pressure transducer technical characteristics as CCD sensitivity threshold and the pattern of change in the measured pressures is proposed. This method allows evaluating the accuracy characteristics of an aerometric pressure sensor at the design stage that speeds up their development process. For example, in Tables II and III the results of numerical simulation, which reflect the discreteness of aerometric parameters measurement for various elastic sensitive elements with a sensitivity threshold S = 0.001 mm are presented. The results of calculating the equivalent stresses and the safety factor by the finite element modeling method showing that the developed elastic element have sufficient strength is presented in Table III. Table II shows that ESE No. 2 and No. 5 with a given measurement discreteness provide the required measurement accuracy that meets the requirements of Airworthiness Standards. Table IV shows that the best samples of sensors have an error no more than 0.01 - 0.02% of the measurement range. Such high accuracy is imposed to the sensors in connection with the need to calculate the motion parameters at a level that meets international requirements. Figures 7 show that the discrepancy between the results of numerical modeling of the static characteristics of the ESE from the experimental data is no more than 15% of the membrane rigid center working deflection; when using the ANSYS software package, no more than 9%.

VI. Conclusion

As the result of the work, an original design of the pressure sensor based on the optical method of information conversion, which has high metrological characteristics, has been created. An original method for calculating elastic sensitive elements considering the sensitivity threshold of the CCD and the pattern of changing the measured pressure gradient depending on the altitude and speed parameters of the aircraft is proposed. Numerical modeling of the accuracy characteristics of pressure sensors by analytical and finite element modeling methods and a comparative evaluation of the results have been performed. The results of the experiments carried out by the authors and the results of the experimental studies of the authors indicated in the list of references confirm the adequacy of theoretical methods for calculating the parameters of elastic elements for pressure sensors. Authors identify the main directions for further work on the research and development of aerometric pressure sensors based on CCD establishing the influence of external and boundary conditions on the accuracy of measuring altitude-velocity parameters based on the research.

References

[1]	Julien Philippe, Maria Valeria de Paolis, Cristina Arenas-Buendia, et al.. Passive and Chipless Packaged Transducer for Wireless Pressure Measurement. *Sensors and Actuators A: Physical*, Elsevier, 2018, 279, pp.753-762.

[2]	Antonets I. V., Gorshkov G. M., Borisov R.A. Aerometricheskij datchik davleniya, ispol'zuyushchij opticheskij metod preobrazovaniya informacii [*Aerometric pressure sensor using an optical information conversion method*]. Patent RF, no. 2653596, 2018.

[3]	Lebed'ko E. G., Zvereva E. N., Nguen Vu Tung. Vysokotochnoe opredelenie uglovogo polozhenija tochechnogo istochnika izluchenija s PZS-linejkami [High-precision determination of the angular position of a point radiation source from a line of photoelectric elements]. Nauchno-tehnicheskij vestnik informacionnyh tehnologij, mehaniki i optiki [*Scientific and Technical Bulletin of Information Technologies, Mechanics and Optics*], 2015, Vol. 15, no. 3, pp. 398-404. (in Russian).

[4]	Bilizhenko I. V., Volkhonskiy V. V., Vorobyov P. A., Malyshkin S. L. Formirovanija diagramm napravlennosti optiko-jelektronnyh izveshhatelej na osnove mnogojelementnyh priemnikov IK izluchenija [Formation of directionaldiagrams of passive infrared detectors based on multi-element receivers of IR radiation]. Izv. vuzov. Priborostroenie [*News of higher educational institutions. Instrumentation*], 2017, Vol. 60, no. 1. pp. 96-99 (in Russian).

[5]	Panov D.YU. O bol'shih progibah kruglyh membran so slabym gofrom [On large deflections of round membranes with a weak corrugation]. Prikladnaya mekhanika i matematika [*Applied mechanics and mathematics*], 1941, vol. 5, no. 2, pp. 303-318 (in Russian).

[6]	Feodosyev V.I. O bol'shih progibah i ustojchivosti krugloj membrany s melkoj gofrirovkoj [On large deflections and stability of a round membrane with fine corrugation]. Prikladnaya matematika i mekhanika [*Applied mechanics and mathematics*], 1945, no. 9, pp. 389-412 (in Russian).

[7]	Feodosev V.I. Uprugie elementy tochnogo priborostroenija [*Elastic elements of precision instrument making*]. Moscow, State publishing house of defense literature Publ., 1949, 284 p. (in Russian).

[8]	Andreeva L.E. Raschet harakteristik gofrirovannyh membrane [Calculation of characteristics of corrugated membranes]. Priborostroenie [*Instrument making*], 1956, no. 3, pp. 11-17 (in Russian).

[9]	Andreeva L. E. Uprugie elementy priborov [*Elastic elements of devices*]. Moscow, Engineering Publ., 1980, 230 p. (in Russian).

[10]	Andreeva L.E. Raschet gofrirovannyh membrane [Calculation of corrugated membranes]. Raschety na prochnost v mashinostroenii [*Strength calculations in mechanical engineering*]. 1955, no. 46, pp. 55-67 (in Russian).

[11]	Ponomarev S. D., Andreeva L. E. Raschet uprugih elementov mashin i priborov [*The calculation of the elastic elements of machines and devices*]. Moscow, Engineering Publ., 1989, 792 p.

(in Russian).

[12] Borisov R.A., Antonec I. V. Programma dlja rascheta uprugih chuvstvitel'nyh jelementov datchikov ajerometricheskih davlenij [*The program for calculating the elastic sensitive elements of air pressure sensors*]. No. 2019663045, 2019.

[13] Verkovich G. A., Golovenkin E. N., Golubkov V. A. Spravochnik konstruktora tochnogo priborostroeniya [*Reference Designer precision instrumentation*]. Leningrad, Engineering Publ., 1964, 460 p. (in Russian).

[14] Litvina F.L. Spravochnik konstruktora tochnogo priborostroeniya [*Reference Designer precision instrumentation*]. Moscow, Engineering Publ., 1964, 460 p. (in Russian). Moscow, Engineering Publ., 1980, 326 p. (in Russian).

[15] Felikson E. I. Uprugie elementy priborov [*Elastic elements of devices*]. Moscow, Engineering Publ., 1977, 311 p. (in Russian).

[16] Asch G. Les capteurs en enstrumentation industrielle [*Sensors in industrial instrumentation*]. Lyon, 1991, 970 p.

[17] Barber J. R. *Elasticity*, Second Edition. Kluwer, 2004, 431 p.

[18] Borisov R.A., Antonec I. V. Programma upravleniya mikrokontrollerami semejstva STM32F4, obespechivayushchaya izmerenie linejnyh peremeshchenij chuvstvitel'nyh elementov datchikov, ispol'zuyushchih opticheskie preobrazovateli. Svidetel'stvo ob ofitsial'noi registratsii programm dlya EVM [*The program for controlling microcontrollers of the STM32F4 family, providing measurement of linear displacements of sensitive elements of sensors using optical converters. The Certificate on Official Registration of the Computer Program*]. No. 2019612079, 2019.

[19] Pan'kov A.A., Pisarev P.V. Numerical modeling of electroelastic fields in the surface piezoelectric luminescent optical fiber sensor to diagnose deformation of composite plates. *PNRPU Mechanics Bulletin*, 2020, no. 2, pp. 64-77.
doi: 10.15593/perm.mech/2020.2.06

[20] Arango JD, Vélez YA, Aristizabal VH, Vélez FJ, Gómez JA, Quijano JC, Herrera-Ramirez J. Numerical study using finite element method for the thermal response of fiber specklegram sensors with changes in the length of the sensing zone. *Computer Optics* 2021; 45(4): 534-540.
doi: 10.18287/2412-6179-CO-852

[21] Mohammadi, M., Kiani-Oshtorjani, M., Mikkola, A., The Effects of Oil Entrained Air on the Dynamic Performance of a Hydraulically Driven Multibody System, (2020) *International Review on Modelling and Simulations (IREMOS)*, 13 (4), pp. 214-222.
doi: https://doi.org/10.15866/iremos.v13i4.18612

[22] Bielawski, R., Rządkowski, W., Kowalik, M., Kłonica, M., Safety of Aircraft Structures in the Context of Composite Element Connection, (2020) *International Review of Aerospace Engineering (IREASE)*, 13 (5), pp. 159-164.
doi: https://doi.org/10.15866/irease.v13i5.18805

[23] Auersvald, Jan & Draxler, Karel. (2015). *Aerometric system for general aviation*. 1-6.
doi: 10.1109/MILTECHS.2015.7153718

[24] Konovalov Roman (2015) *Digital methods and algorithms for improving the accuracy of secondary transducers of parametric pressure sensors*, Cand.Sci Dissertation, Yuri Gagarin State Technical University of Saratov, 2015., 125 p. (in Russian).

[25] Belov V, Vinokurov L, Gavrilov V, Kozhevnikov V, Kuznetsov I, Makarov N, Sorokin M, *Frequency pressure sensor*, Patent №RU 123143 U1, 2012

[26] Belozubov E, Belozubova N, Vasiliev V, *Pressure sensor with vibration-resistant nano- and microelectromechanical system*, Patent № RU 2 432 556 C1, 2011

[27] Tikhonenkov V, Sorokin M. Method of compensating multiplicative temperature error of a sensor with a vibrating element, *Bulletin of the Ulyanovsk State Technical University*, no. 2 (34), 2006, pp. 40-43.

[28] Ciarlet, Philippe. (2005). An Introduction to Differential Geometry with Applications to Elasticity. *Journal of Elasticity*. 78-79. 1-215.
doi: 10.1007/s10659-005-4738-8

[29] Elbestawi, M.A. Force measurement. In *The Measurement, Instrumentation and Sensors Handbook*; Webster, J.G., Ed.; CRC Press: Boca Raton, FL, USA, 1999; pp. 23.1–23.17.

[30] Gong, Shih-Chin & Lee, Chengkuo. (2002). Analytical Solutions of Sensitivity for Pressure Microsensors. *Sensors Journal, IEEE*. 1. 340 - 344.
doi: 10.1109/7361.983474

[31] Nyce, David S.. *Linear position sensors: theory and application*" (2004).

[32] Rieger, Marc Oliver. "*A model for hysteresis in mechanics using local minimizers of Young measures*." (2005).

[33] Borisov R., Antonec I, Method for measuring the amount of deflection of an elastic sensing element that measures static pressure *II International Correspondence Scientific and Practical Conference of BSAA "Aviation: History, Modernity, Prospects for Development"* November 9-10, 2017 (in Russian).

[34] Szabo, S., Vajdova, I., Jencova, E., Blasko, D., Rozenberg, R., Mikula, B., Fire Risk Assessment of Composite Materials in Aviation by Hazard Levels Characterized in Standard EN 45545, (2020) *International Review of Aerospace Engineering (IREASE)*, 13 (5), pp. 182-188.
doi: https://doi.org/10.15866/irease.v13i5.17697

[35] Bielawski, R., Rządkowski, W., Kowalik, M., Kłonica, M., Safety of Aircraft Structures in the Context of Composite Element Connection, (2020) *International Review of Aerospace Engineering (IREASE)*, 13 (5), pp. 159-164.
doi: https://doi.org/10.15866/irease.v13i5.18805

[36] Fioriti, M., Vercella, V., A Parametric Cost Model for Estimating Civil Aircraft Line and Base Maintenance, (2019) *International Review of Aerospace Engineering (IREASE)*, 12 (6), pp. 250-260.
doi: https://doi.org/10.15866/irease.v12i6.17333

Authors' information

[1]Ulyanovsk Civil Aviation Institute, 8/8 Mozhaiskogo Str., 432071, Ulyanovsk, Russian Federation.

[2]Saint Petersburg Electrotechnical University "LETI", 5 Professora Popova str., 197376, St. Petersburg, Russian Federation.

[3]Riga Technical University, Institute of Telecommunications, 12 Azenes Str., LV-1048, Riga, Latvia.

Ruslan A. Borisov is Post-graduate student of the Chair of Aeronautical Engineering, Ulyanovsk Civil Aviation Institute. His field of interest includes pressure sensors, digital signal processing, vibration sensors and beyond.

Ivan V. Antonec earned Doctor of Technical Sciences degree in 1980 in Ulyanovsk Civil Aviation Institute, Russia. Currently he is Professor of the Chair of Aeronautical Engineering in Ulyanovsk Civil Aviation Institute, Russia. His field of interests includes avionics, sensors and other systems onboard of aircrafts.

Aleksandr V. Krotov earned engineering degree in ETU "LETI" in 2012. Since 2019 he works at PhD study in ETU "LETI" and since 2020 in RTU. His research interests include optics, photonics, fiber optical networks, digital signal processing, avionics, sensors and beyond.

Sergey A. Tarasov graduated with honors from ETU "LETI" among the first graduates of master's degree program "Electronics and Microelectronics" of the Faculty of Electronics. In the same year, he entered the postgraduate course of ETU "LETI" and defended his PhD thesis in physical and mathematical sciences on modeling characteristics and the creation of photosensitive devices in 2001. Since 2017, he is the Head of the Department of Quantum Electronics and Optoelectronic Devices, since 2018 - Department of Photonics in Saint-Petersburg State Electrotechnical University.

Vjaceslavs Bobrovs received the M.Sc. degree in telecommunications and the Dr.Sc.Ing. degree in electronics and telecommunications from Riga Technical University, Riga, Latvia, in 2005 and 2010, respectively. He is currently a Professor and the Director of the Institute of Telecommunications, the Head of the Transmission Systems Department. His research interests include nonlinear optics, photonics, fiber optical metro and access networks, radio-over-fiber technologies, digital signal processing, 5G, and beyond.

82

5-PAPER: FPGA-Implemented Fractal Decoder with Forward Error Correction in Short-Reach Optical Interconnects

FPGA-Implemented Fractal Decoder with Forward Error Correction in Short-Reach Optical Interconnects

Svitlana Matsenko [1,*], Oleksiy Borysenko [2], Sandis Spolitis [1,3], Aleksejs Udalcovs [4], Lilita Gegere [3], Aleksandr Krotov [3], Oskars Ozolins [3,4,5] and Vjaceslavs Bobrovs [3]

[1] Communication Technologies Research Center, Riga Technical University, 1048 Riga, Latvia; Sandis.Spolitis@rtu.lv
[2] Department of Electronics and Computer Technology, Sumy State University, 40007 Sumy, Ukraine; Oleksiy.Borysenko@ekt.sumdu.edu.ua
[3] Institute of Telecommunications, Riga Technical University, 1048 Riga, Latvia; Lilita.Gegere@rtu.lv (L.G.); Aleksandr.Krotov@rtu.lv (A.K.); Oskars.Ozolins@ri.se (O.O.); Vjaceslavs.Bobrovs@rtu.lv (V.B.)
[4] Networks Unit, RISE Research Institutes of Sweden, Kista, 164 40 Stockholm, Sweden; Aleksejs.Udalcovs@gmail.com
[5] Applied Physics Department, KTH Royal Institute of Technology, 106 91 Stockholm, Sweden
* Correspondence: Svitlana.Matsenko@rtu.lv

Abstract: Forward error correction (FEC) codes combined with high-order modulator formats, i.e., coded modulation (CM), are essential in optical communication networks to achieve highly efficient and reliable communication. The task of providing additional error control in the design of CM systems with high-performance requirements remains urgent. As an additional control of CM systems, we propose to use indivisible error detection codes based on a positional number system. In this work, we evaluated the indivisible code using the average probability method (APM) for the binary symmetric channel (BSC), which has the simplicity, versatility and reliability of the estimate, which is close to reality. The APM allows for evaluation and compares indivisible codes according to parameters of correct transmission, and detectable and undetectable errors. Indivisible codes allow for the end-to-end (E2E) control of the transmission and processing of information in digital systems and design devices with a regular structure and high speed. This study researched a fractal decoder device for additional error control, implemented in field-programmable gate array (FPGA) software with FEC for short-reach optical interconnects with multilevel pulse amplitude (PAM-M) modulated with Gray code mapping. Indivisible codes with natural redundancy require far fewer hardware costs to develop and implement encoding and decoding devices with a sufficiently high error detection efficiency. We achieved a reduction in hardware costs for a fractal decoder by using the fractal property of the indivisible code from 10% to 30% for different n while receiving the reciprocal of the golden ratio.

Keywords: coded modulation; error-correcting codes; error-detecting codes; indivisible codes; fractal decoder; short-reach optical interconnects

1. Introduction

With the development of the 5G network architecture, 4K/8K video streaming, the Internet of Things (IoT), cloud computing, and other modern technologies, the task of improving the reliability of data transmission remains urgent [1]. With an increase in the volume of the transmitted information and growing traffic, a strong candidate is PAM-M since it possesses cost-effectiveness, spectral efficiency, energy efficiency, and simplicity [2–6]. Although it is studied for short-reach networks, PAM-M format modulation was considered for C-band mobile and interdata centre networks.

Optical communication systems need to maintain highly efficient and highly reliable communications using digital signal processing (DSP), forward error correction (FEC), and

modern coherent technologies via techniques such as pulse shaping. Using high spectral efficiency (SE) modulation formats and powerful FEC techniques is one way to address the Internet's exponential traffic growth and improve transmission reach. In theory of codes, there are a few types of FEC codes, such as hard-input hard-output (HIHO) and soft-input soft-output (SISO) decoders. HIHO decoding uses hard values, in which the output is quantized only to two levels. In contrast, SISO decoding uses soft values, where confidence information for the decision is not just one or zero decisions. This "soft information" is often represented using logarithmic likelihood ratios (LLRs) that operate as the input of soft-decision FEC decoders [7–10].

When post-FEC bit error rate (BER) is concerned, a minimum of 10^{-12} or preferably 10^{-15} is generally required [11]. HD-FEC codes that meet system needs of 100 Gb/s and beyond typically have a more negligible overhead, and do not require costly A/D converters for their implementation. From this type of code, the best net coding gain (NCG) at 10^{-15} post-FEC BER is provided by concatenated interleaved Bose–Chaudhuri–Hocquenghem (CI)-(BCH) 4 with a 20% overhead (OH) [12,13] and Turbo Product code with shortened BCH component codes [14], whereas CI-BCH 4 with 7% (OH), Swizzle [15] and Staircase codes [16] achieves the most outstanding performance for a standard (7%) OH. From the class of SD-FEC codes, the spatially coupled type low-density parity-check (LDPC) code [17] exhibits the highest NCG at a 10^{-15} post-FEC BER, with OH is at 5% higher than that of the other described FEC codes. LDPC-CCs [18] and ViaSat's TPCs [19,20] are the two implemented schemes with the greatest correcting performance with a 20% OH at a post-FEC BER of 10^{-15}. Some of the other proposed LDPC-based codes also achieve similar or even better performance (e.g., large-girth LDPC [21,22] or nonbinary QC-LDPCs [22,23]).

Positional number systems, on the basis of which indivisible codes are generated, such as noninteger position number systems based on the golden ratio, Fibonacci [24–28], binomial, and permutation codes, were researched in [29,30], or quaternary imaginary number systems [31]. The Fibonacci code is an error detection code capable of detecting errors in both transfers of information and processing, i.e., has an end-to-end (E2E) control property. This code is most effective in asymmetric channels for processing and transmitting information in which the errors' type is $0{\to}1$. This asymmetry is compensated for by using FEC codes with artificial redundancy, thereby obtaining a cumulative effect of improved interference resistance [24–28]. The Fibonacci code is effectively used for computer arithmetic and developing digital devices on their basis. A new method for representing images using a nonstandard positional number system was developed and considered [32]. The residue number system (RNS) arithmetic is effectively used in design technologies and new applications in cryptography, machine learning, and deep convolutional neural networks, Internet of Things (IoT) devices, postquantum algorithms and circuits, embedded processor design, and other related emergent topics [33–36].

The main criterion for any error control codes (ECC) is the use of redundant information contained in the encoded words, which is typically artificially introduced into them. Another type of redundant coding uses natural redundancy in the codewords. The application of natural redundancy codes requires far less hardware to synthesize encoding and decoding devices, and uses more straightforward methods to accomplish these tasks. Indivisible codes are practical to use for constructing coding and decoding devices. An end-to-end (E2E) control is possible in them, both transmitting information and processing, which can considerably improve their efficiency. The positive effect is achieved due to the use of indivisible codes to control digital devices that process information, and for communication channels. It reduces hardware expenses required for the work of a network, and increases performance speed and reliability. In addition, the application of hybrid types of ECC in optical communication systems using natural redundancy can be significantly enhanced by using codes with artificial redundancy. In this way, using relatively fewer complex algorithms in encoding and decoding devices for hardware implementation can achieve more effective indicators to protect transmitted and processed data.

E2E data control enables both transmission and digital devices, which significantly improves the efficiency of information systems. Codes involving artificial redundancy are designed only for error control tasks in either communication channels or information processing systems and do not allow for E2E data control. This creates effectively evaluating indivisible error detection codes with natural redundancy for their further application in digital devices and systems. As an additional control, indivisible codes can be used in conjunction with FEC codes, making it possible to simplify implementation methods of encoding and decoding devices with significant error detection properties.

In this paper, we investigate a fractal decoder, which was implemented in FPGA using Intel Quartus Prime software. The device was investigated for a 56 and 35 Gbaud PAM- M (M = 4, 8) modulation with Gray code mapping using wavelength division multiplexed (WDM) optical interconnect model with a standard single-mode fibre (SSMF) and erbium-doped fibre amplifier (EDFA). We investigate the combination of an indivisible natural redundancy error detection code with an artificial redundancy FEC based on the interleaved BCH + LDPC and RS + LDPC FEC. We also evaluate the indivisible error detecting code using the average probability method (APM), which demonstrated that the simplicity, versatility, and reliability of estimation is close to reality. This shows that it is possible to reduce the saving hardware costs of the fractal decoder by using the fractal property of indivisible code. An increase in the savings in hardware costs occurs with an increase in the code length of the indivisible code, which is limited to the reciprocal of the golden ratio. With fractal decoding, the signal delays twice as much as the standard method of constructing line Fibonacci decoders.

The paper is structured as follows: Section 2 presents the theoretical aspects and estimation of the indivisible code based on the APM for a binary symmetric channel (BSC). Section 3 analyses the 56 and 35 Gbaud wavelength division multiplexed (WDM) short-reach optical interconnects for PAM-M (M = 4, 8) modulation with Gray code mapping with SSMF and EDFA. EDFA is used for signal amplification and to investigate the code performance in the presence of ASE noise. The simulation results of the WDM optical interconnect model with interleaved BCH + LDPC, and RS + LDPC with the fractal decoder device are also presented in Section 3. Section 4 investigates the fractal decoder device for the indivisible error-detecting code implemented in FPGA software. Lastly, we conclude this paper in Section 5.

2. Theoretical Aspects and Estimation of Indivisible Code Based on APM

2.1. Theoretical Aspects of Indivisible Code

In this paper, we use the Fibonacci indivisible error-detection code. The Fibonacci number system makes it possible to generate the Fibonacci code, consisting of Fibonacci numbers whose weights are a sequence of numbers 1, 1, 2, 3, 5, 8, ... , F_n.

Equation (1) defines a sequence of numbers in an indivisible code [37–39]:

$$F_n = F_{n-1} + F_{n-2}. \tag{1}$$

It follows from Equation (1) that each subsequent element of the Fibonacci series is equal to the sum of its two preceding elements. The quantitative value of the Fibonacci numbers is set by a numbering function whose weights are the Fibonacci numbers represented as Equation (2) [25–28]:

$$N = a_n F_n + a_{n-1} F_{n-1} + \ldots + a_i F_i + \ldots + a_1 F_1 \tag{2}$$

where $a_i \in \{0, 1\}$ is the binary digit of the *i*-th bit in the positional representation of a number; n is the length of the code; F_i is the weight of the *i*-th bit, which is equal to the *i*-th Fibonacci numbers. The abbreviated form of Equation (1) is shown as Equation (3) [25–28]:

$$N_a = a_n a_{n-1}, \ldots, a_i, \ldots, a_1. \tag{3}$$

Table 1 shows the indivisible code for $n = 8$ and numbers $N = 25, 54, 33$, with bit weights 1, 2, 3, 5, 8, 13, 21, 34.

Table 1. Indivisible code for $n = 8$, $N = 25, 54, 33$, for bit weights 1, 2, 3, 5, 8, 13, 21, 34.

Bit Number	8	7	6	5	4	3	2	1
Bit Weight	34	21	13	8	5	3	2	1
$N = 25$	0	1	0	0	0	1	0	1
$N = 54$	1	0	1	0	1	0	1	0
$N = 33$	0	1	0	1	0	1	0	1

The range of Fibonacci numbers is determined from Equation (4) [25–28]:

$$P = F_n + F_{n-1} \tag{4}$$

where F_n is the weight of the n-th bit of the Fibonacci numbers; F_{n-1} is the weight of the $n-1$ bits of the Fibonacci numbers.

Using two binary numbers, the range of Fibonacci numbers equals $P_2 = 1 + 1 = 2$, for $P_3 = 2 + 3 = 5$, for $P_4 = 3 + 5 = 8$. This code prohibits having two unities side by side, which is a sign of an error. If there are three neighbouring unities in the code combination, the middle bits can be corrected by inverting it to zero, resulting in a correction in the error-detecting code. Thus, the indivisible code can detect errors and correct some, transforming this code into an FEC code.

The fractal structure of the indivisible code with $n = 5$ is shown in Table 2.

Table 2. Fractal structure of indivisible code.

Code Combinations					Code Combinations					
Fractal 1					Fractal 2					
Bit Number	5	4	3	2	1	**Bit Number**	5	4	3	2	1
Bit Weight	8	5	3	2	1	**Bit Weight**	8	5	3	2	1
№	x_5	x_4	x_3	x_2	x_1	№	x_5	x_4	x_3	x_2	x_1
0	0	0	0	0	0	8	1	0	0	0	0
1	0	0	0	0	1	9	1	0	0	0	1
2	0	0	0	1	0	10	1	0	0	1	0
3	0	0	1	0	0	11	1	0	1	0	0
4	0	0	1	0	1	12	1	0	1	0	1
5	0	1	0	0	0						
6	0	1	0	0	1						
7	0	1	0	1	0						

The indivisible code possesses the property of self-similarity consisting of fractals with several ranks. Equation (1) forms the fractal of the first rank, from which multifractals of the second, third, etc. are constructed ranks. Table 2 shows that the fractals of the first rank are the first five bits with 0 in the MSB, and the last five bits with 1 in the MSB. Bits 0 or 1 in the MSB are identifier fractals 1 and 2. Thus, they are enough to decode one of the fractals and save hardware costs. The line decoder decodes the nonfractal part of the code.

2.2. Estimation of Indivisible Code Based on Average Probability Method (APM)

We applied the APM for the BSC to estimate the indivisible code. The APM determines the probabilities of the transitions of code combinations of an indivisible code into proper, allowed, and prohibited classes. The APM possesses simplicity, versatility, and reliability of estimation, close to reality [40].

The probability of the proper transition of the indivisible code is represented by Equation (5):

$$C = \sum_{i=1}^{M} P_i p_i^i \tag{5}$$

where P_i is the probability that an information source generates the i-th code combination; p_i^i is the probability that the i-th code combination is properly transferred into the i-th code combination.

The probability of undetectable erroneous transitions of the indivisible code is represented by Equation (6):

$$V = \sum_{i=1}^{M} P_i p_i^u, \tag{6}$$

where p_i^u is the probability that the i-th code combination is erroneously transferred into the class of code combinations that is not detected.

The probability of an erroneous transition of the indivisible code is represented by Equation (7):

$$p_i^u = \sum_{j=1, j \neq i}^{M} p_{i,j}^u \tag{7}$$

where $p_{i,j}^u$ is the probability that the i-th code combination is erroneously transferred into the j-th allowable code combination.

The probability of the detected error is determined from Equation (8):

$$Z = \sum_{j=1}^{M} P_i p_i^d \tag{8}$$

where p_i^d is the probability that the i-th code combination is erroneously transferred into the j-th allowable code combination, and represented by Equation (9):

$$p_i^d = \sum_{j=M+1}^{N} p_{i,j}^d \tag{9}$$

where $p_{i,j}^d$ is the probability that the i-th code combination is erroneously transferred into the j-th prohibited combination.

Figure 1 shows the possible transformations of 2^k code combinations of indivisible code into classes C, V, Z.
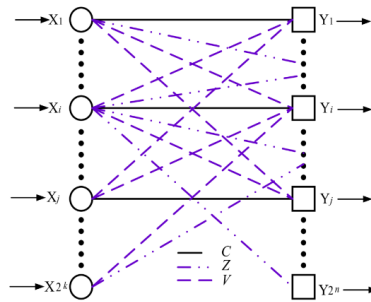

Figure 1. Possible transformations of code combinations of indivisible code into classes C, V, Z.

　　　　The input data for the APM are the probabilities of the transition of 0 to 0 (p_{00}) and 1 to 1 (p_{11}). The probability of an erroneous transition of 0 to 1 and 1 to 0 is determined by $p_{01} = 1 - p_{00}$, $p_{10} = 1 - p_{11}$.

　　　　Figure 2 shows the probability of the proper data transmission of the indivisible code: (a) $\text{Log}_{10}(C)$ from n, for example, for $p_{10} = 3 \times 10^{-4}$; 3×10^{-5}; 3×10^{-6}, and $p_{01} = 3 \times 10^{-3}$; 3×10^{-4}; 3×10^{-5}; (b) $\text{Log}_{10}(C)$ from $\text{Log}_{10}(p_{10})$ for $p_{10} = 1.5 \times 10^{-3} - 1.5 \times 10^{-7}$; $3 \times 10^{-3} - 3 \times 10^{-7}$; $5 \times 10^{-3} - 5 \times 10^{-7}$, at $n = 6$.
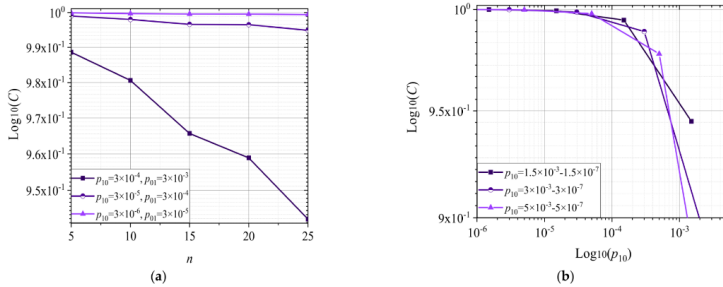
Figure 2. Probability of proper data transmission of indivisible code (**a**) $\text{Log}_{10}(C)$ from n for $p_{10} = 3 \times 10^{-4}$; 3×10^{-5}; 3×10^{-6}, and $p_{01} = 3 \times 10^{-3}$; 3×10^{-4}; 3×10^{-5}; (**b**) $\text{Log}_{10}(C)$ from $\text{Log}_{10}(p_{10})$ for $p_{10} = 1.5 \times 10^{-3} - 1.5 \times 10^{-7}$; $3 \times 10^{-3} - 3 \times 10^{-7}$; $5 \times 10^{-3} - 5 \times 10^{-7}$.

　　　　Figure 2a shows that, with an increase in n, the number of bits in which an error of the indivisible code is possible increases. The probability of correct transmission decreases with increasing n, but in some cases, it reaches 99.9%. Figure 2b shows that, with the probability value (p_{10}) decreasing, the likelihood of correct data transmission increases at $n = 6$.

　　　　Figure 3 shows the probability of an undetectable error of the indivisible code: (a) $\text{Log}_{10}(V)$ from n for $p_{10} = 3 \times 10^{-4}$; 3×10^{-5}; 3×10^{-6}, and $p_{01} = 3 \times 10^{-3}$; 3×10^{-4}; 3×10^{-5}; (b) $\text{Log}_{10}(V)$ from $\text{Log}_{10}(p_{01})$ for $p_{01} = 1.5 \times 10^{-3} - 1.5 \times 10^{-6}$; $3 \times 10^{-3} - 3 \times 10^{-6}$; $5 \times 10^{-3} - 5 \times 10^{-6}$, at $n = 6$.

Figure 3. Probability of an undetectable error of the indivisible code (**a**) $\text{Log}_{10}(V)$ from n for $p_{10} = 3 \times 10^{-4}$; 3×10^{-5}; 3×10^{-6}, and $p_{01} = 3 \times 10^{-3}$; 3×10^{-4}; 3×10^{-5}; (**b**) $\text{Log}_{10}(V)$ from $\text{Log}_{10}(p_{01})$ for $p_{01} = 1.5 \times 10^{-3} - 1.5 \times 10^{-6}$; $3 \times 10^{-3} - 3 \times 10^{-6}$; $5 \times 10^{-3} - 5 \times 10^{-6}$.
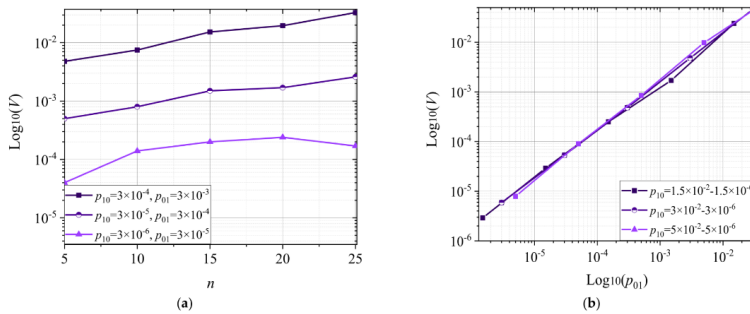
Figure 3a shows that the probability of an undetectable error of the indivisible code increases with n. Figure 3b shows that, with a decrease in the probability value (p_{01}), the probability of an undetectable error V decreases at $n = 6$.

Figure 4 shows the probability of a detected error of the indivisible code: (a) $\text{Log}_{10}(Z)$ from n for $p_{10} = 3 \times 10^{-4}$; 3×10^{-5}; 3×10^{-6}, and $p_{01} = 3 \times 10^{-3}$; 3×10^{-4}; 3×10^{-5}; (b) $\text{Log}_{10}(Z)$ from $\text{Log}_{10}(p_{10})$ for $p_{10} = 1.5 \times 10^{-3}\text{–}1.5 \times 10^{-6}$; $3 \times 10^{-3}\text{–}3 \times 10^{-6}$; $5 \times 10^{-3}\text{–}5 \times 10^{-6}$, at $n = 6$.
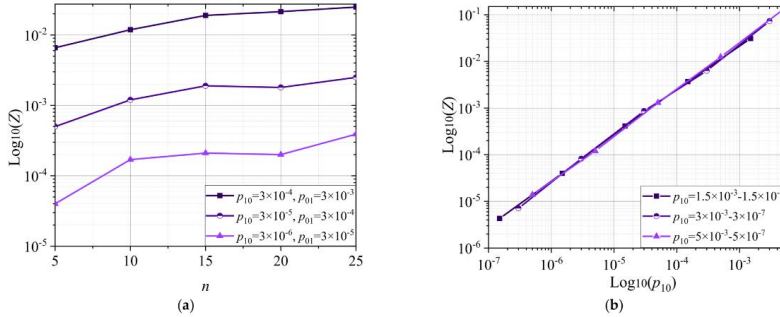
Figure 4. Probability of an error detected in the indivisible code. (**a**) $\text{Log}_{10}(Z)$ from n for $p_{10} = 3 \times 10^{-4}$; 3×10^{-5}; 3×10^{-6}, and $p_{01} = 3 \times 10^{-3}$; 3×10^{-4}; 3×10^{-5}; (**b**) $\text{Log}_{10}(Z)$ from $\text{Log}_{10}(p_{01})$ for $p_{01} = 1.5 \times 10^{-3}\text{–}1.5 \times 10^{-7}$; $3 \times 10^{-3}\text{–}3 \times 10^{-7}$; $5 \times 10^{-3}\text{–}5 \times 10^{-7}$.

Figure 4a shows that the probability of a detected error in the indivisible code increases with n. Figure 4b shows that, with a decrease in the probability value (p_{10}), the probability of the detected error decreases at $n = 6$. The APM allows for the evaluation of codes with any code distance, starting from code distance $d = 1$. The APM makes it possible to compare and estimate error probability, in both the processing and transmission of indivisible codes.

3. System Model, Achievable Rates and Numerical Analysis of an Optical System

3.1. System Model and Achievable Rates

Figure 5 shows a five-channel WDM optical interconnect model that integrates concatenated FEC based on BCH + LDPC, RS + LDPC FEC with an interleaver or deinterleaver, and the indivisible code with the fractal decoder.
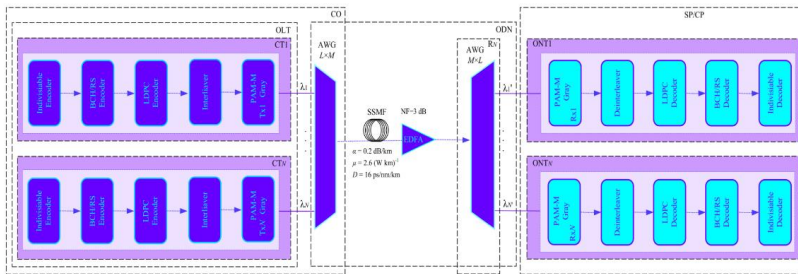
Figure 5. WDM optical interconnect model.

The architecture of the 5 WDM-channel PAM-M with Gray code mapping and simple pulse-shaping comprises a pseudorandom binary sequence (PRBS) generator; indivisible encoders; interleaved BCH + LDPC, RS + LDPC FEC encoders; optical transmitters $(Tx_1–Tx_N)$, which consist of central office (CO); optical distribution network (ODN); subscriber premises/customer premises (SP/CP); optical line terminal (OLT); channel terminals $(CT_1–CT_N)$, arrayed waveguide grating (AWGs) $N \times M$ multiplexers/$M \times N$ demultiplexers; single-mode fibre (SSMF) and EDFA amplifier with 3dB noise figure; remote node (R_N); optical network terminals $(ONT_1–ONT_N)$, which comprises the receivers $(Rx_1–RX_N)$, interleaved BCH + LDPC, RS + LDPC FEC, and indivisible decoders.

The 5-channel WDM optical interconnect model with PAM-M modulation format was chosen as the primary system parameters: the channel spacing was chosen to be equal to 100 GHz according to the ITU-T G.694.1 recommendation [41], the central frequencies were set to 193.1 THz (optical *C*-band), and the data rate per channel was 56 and 35 Gbaud for PAM-M ($M = 4, 8$). The optical line terminal (OLT) comprises N-channel terminals (CT), comprising N-optical transmitters (OT), where N is the transmitter number. The CT_N block includes the continuous wave (CW) lasers and Mach–Zehnder modulators (MZM) with a 30 dB extinction ratio, and CW lasers with an optical output power of +11 dBm. In the AWGs, the following parameters are used according to the commercial datasheet: an operation range of 193–193.5 GHz, a Gaussian passband, a 3 dB bandwidth of 75 GHz, and an insertion loss of 3 dB per channel.

Table 3 shows the simulation setup parameters for the 5 WDM optical interconnect.

Table 3. Simulation setup parameters for 5 WDM optical interconnect.

Parameter Name	Value
WDM channels	5
Baud rate	56 (PAM-4), 35 (PAM-8) Gbaud
Pulse shaping	Simple
Channel frequency spacing	100 GHz
Attenuation	0.2 dB/km
Dispersion parameter	16 ps/(nm $\times$ km)
Nonlinear coefficient	2.6×10^{-20} m^2/W
EDFA noise figure	3 dB
Coded modulation	PAM-M, Gray code mapping

The data are transmitted through a standard ITU-T G.652 SSMF span from OLT block with attenuation coefficient, 0.2 dB/km; dispersion slope, 0.08 ps/nm^2; dispersion coefficient, 16 ps/(nm $\times$ km); and nonlinear index, 2.6×10^{-20} m^2/W at reference wavelength 1550 nm [42]. The SP/CP includes N optical network terminals (ONTs), which consist of PIN receivers with thermal noise of 7.0×10^{-12} A/Hz$^{1/2}$, dark current 5.0×10^{-8} A, 4-pole order low-pass Bessel electrical filter with 18.75 GHz frequency band, deinterleaved BCH + LDPC; RS + LDPC FEC, and indivisible fractal decoders.

3.2. Numerical Analysis of an Optical System

The WDM optical interconnect model used concatenated codes, for instance, the indivisible error-detection code, interleaved BCH + LDPC (with shortened BCH codes), and RS + LDPC FEC. We used the fractal decoder for indivisible code, Berlekamp–Massey algorithm (BMA) for BCH and RS, and belief propagation algorithm (BPA) for LDPC FEC.

The RS (15, 5) FEC code used 200% overhead (OH), and code rate $R_c = 0.33$. We considered the LDPC FEC code from the digital video broadcasting satellite second-generation standard with code rate $R_c = 0.75$ with 33.3% overhead (OH), block length of $n = 64,800$ bits, and 50 decoding iterations [43].

We investigated the received optical power (ROP) and optical signal-to-noise ratio (OSNR) with concatenated FEC codes for the particular bit error rate (BER) for the WDM optical interconnect model. Figure 6a,b show the BER value change with the ROP of the

central WDM channel. Transmission distances 1000 m for PAM-4 (56 Gbaud) and PAM-8 (35 Gbaud) modulation formats with interleaved BCH + LDPC and RS + LDPC FEC. Figure 7 shows the post-FEC BER vs. pre-FEC BER performance of central WDM channel for PAM-4 (56 Gbaud) and PAM-8 (35 Gbaud) modulated with an optical signal-to-noise ratio (OSNR) and EDFA for (a) PAM-4 modulation format with interleaved BCH + LDPC, and RS + LDPC FEC, (b) PAM-8 modulation format with interleaved BCH + LDPC and RS + LDPC FEC.

Figure 6. Post-FEC BER vs. ROP with 56 and 35 Gbaud B2B and 1000 m SSMF for (**a**) PAM-4 modulation format with interleaved BCH + LDPC and RS + LDPC FEC, and (**b**) PAM-8 modulation format with interleaved BCH + LDPC and RS + LDPC FEC.

Figure 7. Post-FEC BER vs. pre-FEC BER with 56 and 35 Gbaud PAM-M (M = 4, 8) modulation formats with OSNR and EDFA for (**a**) PAM-4 modulation format with interleaved BCH + LDPC and RS + LDPC FEC, and (**b**) PAM-8 modulation format with LDPC, interleaved BCH + LDPC and RS + LDPC FEC.

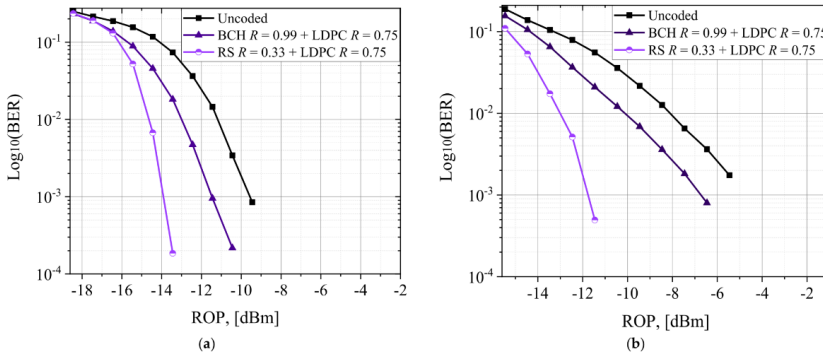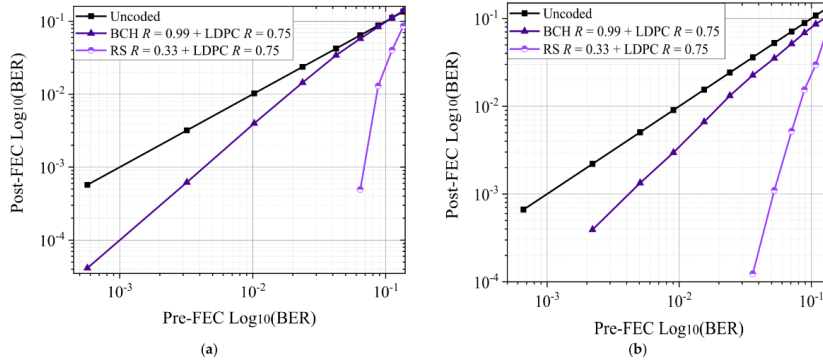Error statistics and post-FEC simulations use the Monte Carlo (MC) BER measurement up to 10^{-5}, using the standard [11] expected BER up to 10^{-15}. Compared to the BCH + LDPC FEC, the RS + LDPC FEC coded system, of which the correction symbol

errors are in each codeword, have the best post-FEC performance and the highest OH
for simulation WDM optical interconnect model. Post-FEC BER values for interleaved
BCH + LDPC and RS + LDPC, which are shown in Figure 6a,b at an ROP, were −18 and
−10 dBm for PAM-4, and −15 and −6 dBm for PAM-8; at a higher ROP, post-FEC BER
values were zero. The post-FEC BER for interleaved BCH + LDPC and RS + LDPC codes in
Figure 7a,b were achieved at an OSNR within the 28–42 dBm and 36–49 dBm for PAM-4
and PAM-8, respectively.

4. Design of the Fractal Decoder Device

Figure 8a,b show the fractal decoder device's block diagram and circuit diagram. The
fractal decoder device includes a block of switching devices 1 (SW 1.1 and SW 1.2), block of
the error detection circuit 2, and block of line decoders 3, comprising a decoder 3.1 (DC 3.1)
with $n − 1$ input, forming the fractal part of the indivisible code with $(n − 1)F_{n−1}$ inputs,
and decoder 3.2 (DC 3.2) with n inputs, forming a nonfractal part of the indivisible code
with $n(F_n − F_{n−1}) = n((F_{n−1} + F_{n−2}) − F_{n−1}) = n \times F_{n−2}$ inputs. The switching devices (SW
1.1, SW 1.2) of block 1, connected to the DC 3.1 and DC 3.2, performed the commutative
switching function of the DC 3.1 and DC 3.2 for the MSB or LSB on the basis of a value of 0
or 1. The MSB transmits to the inverter control input of SW 1.1, and at the same time to the
direct control input of SW 1.2. If the signal is 0, then SW 1.1 is turned on; if it is 1, then SW
1.2. Accordingly, the signal from the output of DC 3.1 appeared at one of the outputs of
SW 1.1 or SW 1.2. The total number of outputs of SW 1.1 and SW 1.2 of block 1 equalled
$2 \times F_{n−1}$.
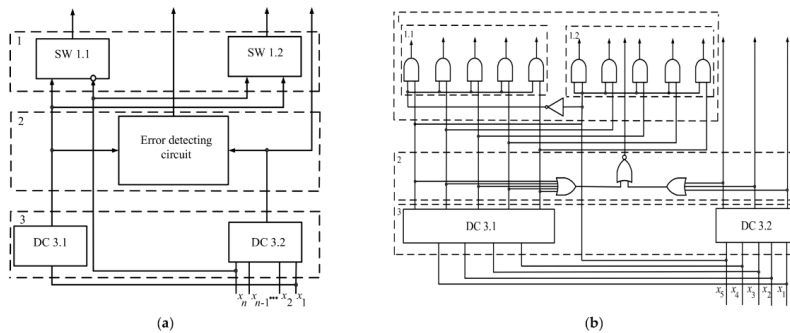
Figure 8. (**a**) Fractal decoder block diagram; (**b**) fractal decoder circuit diagram.

Decoding the essence was as follows: 4 LSB of fractal 1 repeated in 4 LSB of fractal
2 in Table 2. The difference between these fractals lay in the content of zeros or units in
the MSB. Thus, to decode code fractals, it is enough to decode one of them [15–17]. The
nonfractal part of the indivisible code decodes with the use line decoder.

For example, code combinations of the indivisible code shown in Table 2 transmit
to inputs DC 3.1 and DC 3.2. Decoder DC 3.1 decodes fractal 1 corresponding to code
combinations 0–4 or 8–12. Decoder DC 3.2 interprets fractal 2, corresponding to code
combinations 5–7. Depending on the MSB of the code combination of fractals 1 or 2, one of
the elements of switching devices SW 1.1 or SW 1.2 is triggered. If, as a result of decoding
fractal or nonfractal parts of the indivisible code, an error occurs, characterized by the
appearance of two or more units that are next to each other in the code combinations, at
the output of the error detection circuit, a signal of 1 is indicated.

The reduced hardware costs of the fractal decoder compared to the line decoder are due to using one fractal (fractal 1 or 2) in DC 3.1 to decode the code combinations of both fractals. However, instead of the excluded constituent, the fractal decoder uses the switching devices with 2-input OR elements, requiring much lower hardware costs than those of implementing components of the additional fractal part. Due to this, hardware costs are reduced, and this is more remarkable, the more significant the n of the indivisible code is.

Decoders DC 3.1 and DC 3.2 are the line decoders. However, opportunities became available to develop more economical decoder DC 3.1 by analogy with the fractal construction using the same structure as that of the DC 3.2 decoder. More economical decoders DC 3.1 can be implemented according to multifractal construction until the saved hardware costs are profitable. In this case, each subsequent DC 3.1 decoder for its synthesis uses the multifractal of a higher rank—third, fourth, etc.

For example, to implement the fractal decoder for 21 outputs on the basis of a fractal decoder with 13 outputs, the number 21 is represented as fractal equality of the first rank $21 = ((8 + 5) + 8)$, which indicates introducing an additional switching device for 16 outputs. Then, depending on the MSB of decoder 3.2, which includes eight inputs, they are triggered to one of the switching devices consisting of eight 2-input OR elements of the second stage with 16 outputs; 5 outputs in this case remain without switching. As a result, any of the 21st indivisible code combinations are decoded. In designing such multistage decoders, only multifractals of the first and second ranks are used that are then transformed, with the advent of switching devices, into fractals of second and third ranks, third and fourth, and so on, an unlimited number of ranks, thus constructing the multistage decoders.

The method of fractal decoding is as follows:

1. In a set of the indivisible code $f = x_1, x_2, \ldots, x_j, \ldots, x_n$, fractal parts are found that are distinguished by the presence of 0 or 1 in the MSB.
2. The fractal part of the indivisible codes decodes by the line decoder (D 3.1).
3. Depending on the signal of the MSB (0 or 1), the first (SW 1.1) or second switch (SW 1.2) is triggered, wherein its outputs correspond to the numbers of the first or second fractals.
4. The codes are not included in the fractal part decoding by the line decoder (D 3.2).
5. If an erroneous combination is received at the inputs of decoders DC 3.1 and DC 3.2, in which $x_j \times x_{-1} = 1, j = 1, 2, \ldots, n$, an error signal is detected.

The primary indicator in developing a fractal decoder device is saving hardware costs, which are reduced. As a measure for calculating hardware costs, we counted the number of inputs of logical elements of the fractal digital device and present them as a sum of inputs. The sum for line decoders equals the rounded product of the number of inputs by the logarithm of this number. For example, the line decoder for 13 digits has inputs equal to $13 \times 5 = 65$. The switching devices (SW 1.1, SW 1.2) that are triggered, depending on the value of the n-th bits of the MSB outputs of DC 3.2, contain 2×2 $(F_{n-1}) = 4 \times F_{n-1}$ inputs. The sum of inputs for n-bits fractal decoder:

$$S_n = (n-1)F_{n-1} + nF_{n-2} + 4F_{n-1} = nF_{n-1} - F_{n-1} + nF_{n-2} + 4F_{n-1} = nF_{n-1} + nF_{n-2} + 3F_{n-1} = nF_n + 3F_{n-1}.$$

For the line decoder device, the sum of the inputs for n-bits equals $n \times F_{n+1}$—for example, if an $n = 5$ product $n \times F_{n+1} = 5 \times 13 = 65$ exceeds the number of the fractal decoder elements by 10. In actual conditions, when the numbers of the code combinations of the indivisible code, as shown in Table 2, exceed ten digits, hardware costs of the fractal decoder can be significantly reduced [44].

Table 4 shows the number of fractal decoder inputs depending on n.

Table 4. Number of fractal decoder inputs depending on *n*.

n	S_n	*n*	S_n	*n*	S_n
2	7	12	3.21×10^3	22	6.83×10^5
3	15	13	5.59×10^3	23	1.15×10^6
4	29	14	9.67×10^3	24	1.94×10^6
5	55	15	1.66×10^4	25	3.26×10^6
6	102	16	2.84×10^4	26	5.47×10^6
7	186	17	4.87×10^4	27	9.17×10^6
8	335	18	8.30×10^4	28	1.53×10^7
9	567	19	1.41×10^5	29	2.56×10^7
10	1.05×10^3	20	2.39×10^5	30	4.28×10^7
11	1.84×10^3	21	4.04×10^5	31	7.15×10^7

Equation (10) shows the number of inputs with minimization function S_n to the number of inputs $W = n \times F_{n+1}$ fractal decoder device without minimization for *n*:

$$\frac{S_n}{W} = \frac{nF_n + 3F_{n-1}}{nF_{n+1}} = \frac{F_n}{F_{n+1}} + \frac{3F_{n-1}}{nF_{n+1}} \approx \frac{F_n}{F_{n+1}}, \tag{10}$$

where *W* is the number of inputs of the fractal decoder device without minimization of the function.

The absolute value of the number of the saving hardware costs of the fractal decoder:

$$\begin{aligned} Q &= nF_{n+1} - (nF_n + 3F_{n-1}) = n(F_n + F_{n-1}) - nF_n - 3F_{n-1} \\ &= nF_n + nF_{n-1} - nF_n - 3F_{n-1} = nF_{n-1} - 3F_{n-1} = (n-3)F_{n-1}. \end{aligned} \tag{11}$$

Ratio *Q/W* determines the relative number saving hardware costs of the fractal decoder device:

$$\frac{Q}{W} = \frac{nF_{n+1} - (nF_n + 3F_{n-1})}{nF_{n+1}} = 1 - \frac{F_n}{F_{n+1}} - \frac{3F_{n-1}}{nF_{n+1}} \approx 1 - \frac{F_n}{F_{n+1}}. \tag{12}$$

Equation (12) follows the F_{n+1}/F_n with the increase in *n* tending to the reciprocal of the golden ratio.

Table 5 shows the relative number saving hardware costs of the fractal decoder device for *n*.

Table 5. Relative number saving hardware costs of fractal decoder device from *n*.

n	$Q/W \times 100\%$	*n*	$Q/W \times 100\%$	*n*	$Q/W \times 100\%$	*n*	$Q/W \times 100\%$
5	15.38	19	32.16	12	28.77	26	33.78
6	19.23	20	32.47	13	29.17	27	33.95
7	21.76	21	32.74	14	29.88	28	34.12
8	23.89	22	32.98	15	30.58	29	34.24
9	25.45	23	33.21	16	31.05	20	34.37
10	26.74	24	33.42	17	31.42	31	34.55
11	27.97	25	33.61	18	31.81	32	34.61

For *n* = 5, the saving hardware costs of the fractal decoder device are 15.38%, and for *n* = 20, they are 34.37%, which is more than twice as high as the initial value.

We realized the fractal decoder device in FPGA using Intel Quartus Prime software with the device setup of Cyclone V 5csema5f31c6. The FPGA fitting was the realization at a clock frequency of 429.37 MHz. Figure 9 shows the simulation waveform of the fractal decoder device in FPGA for *n* = 5. We utilized adaptive logic modules (ALMs) that, after modelling, were 10/32.070 and less than <1% with low power consumption. The maximal signal delay along the longest path in a combinational circuit was 0.806 ns. No digital signal processing (DSP) slices and RAM were employed. With an increase in the *n* of the fractal

decoder, the delay time did not increase due to parallelization operations. The detecting ability of an indivisible code using the fractal decoder was analysed. For $n = 64,800$, the detecting errors of the indivisible code were 96%.
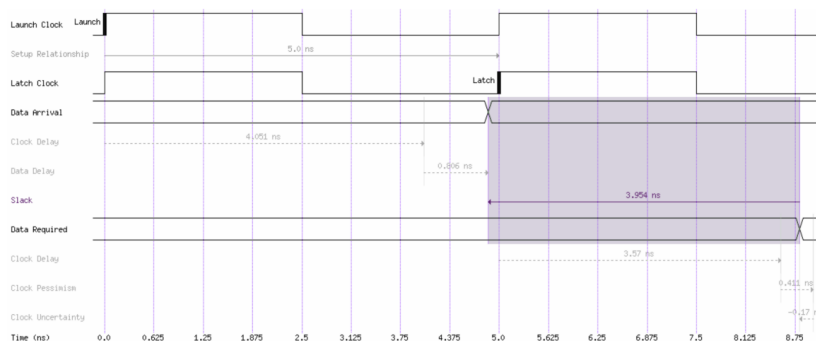

Figure 9. Simulation waveform of the fractal decoder device.

The fractal decoder has a block structure in which n increases by adding switching devices depending on the calculated number of the indivisible code. Compared to saving hardware costs, an assessment of the fractal decoder was also carried out, which reduced hardware costs from 10% to 30% compared to the implementation of line decoders based on the used codes.

5. Conclusions

This paper presented an FPGA-implemented fractal decoder with FEC codes in a short-reach optical interconnect model for additional control CM. An indivisible error-detecting code was evaluated on the basis of the APM. Detection of errors on average probability allowed for assessing indivisible codes with any code distance starting from $d = 1$. The fractal decoder was investigated for 56 and 35 Gbaud PAM-M (M = 4, 8) with PAM-M Gray code mapping with SSMF fibre and EDFA for interleaved BCH + LDPC and RS + LDPC codes. We used the MC method to evaluate the error statistics and post-FEC, in which interleaved concatenated RS + LDPC FEC was more efficient due to the correction of symbolic errors. Thus, it is possible to reduce the hardware costs of a fractal decoder device by using the fractal property of the fractal numbers from 10% to 30%. In some cases, with the increase in their digit capacity, this reduction was quite significant with 96% error detection. Fractal decoder devices use fewer hardware costs compared to line decoders due to the property of the fractality of the indivisible code, which provides significant advantages for the proposed device, reducing its cost, power consumption, and chip size.

Author Contributions: Conceptualization, S.M., O.B., S.S., A.U., L.G., A.K., O.O. and V.B.; data curation, S.M., O.B. and V.B.; investigation, S.M., O.B. and V.B.; software, S.M. and O.O.; writing—original draft, S.M.; writing—review and editing, S.M., O.B., S.S., A.U., L.G., A.K., O.O. and V.B. All authors have read and agreed to the published version of the manuscript.

Institutional Review Board Statement: Not applicable.

Informed Consent Statement: Not applicable.

Data Availability Statement: Not applicable.

Conflicts of Interest: The authors declare no conflict of interest.

References

1. Effenberger, F.J. Industrial Trends and Roadmap of Access. *J. Lightwave Technol.* **2017**, *35*, 1142–1146. [CrossRef]
2. Huo, J.; Zhou, X.; Zhong, K.P.; Tu, J.; Yuan, J.; Guo, C.; Long, K.; Yu, C.; Lau, A.P.T.; Lu, C. Transmitter and receiver DSP for 112 Gbit/s PAM-4 amplifier-less transmissions using 25G-class EML and APD. *Opt. Express* **2018**, *26*, 22673. [CrossRef] [PubMed]
3. Eiselt, N.; Wei, J.; Griesser, H.; Dochhan, A.; Eiselt, M.; Elbers, J.-P.; Olmos, J.J.V.; Monroy, I.T. First Real-Time 400G PAM-4 Demonstration for Inter-Data Center Transmission over 100 km of SSMF at 1550 nm. In Proceedings of the Optical Fiber Communication Conference (OFC), Anaheim, CA, USA, 20–24 March 2016.
4. Lee, J.H.; Chang, S.H.; Huh, J.Y.; Kang, S.-K.; Kim, K.; Lee, J.K. EML based real-time 112 Gbit/s (2 × 56.25 Gbit/s) PAM-4 signal transmission in C-band over 80 km SSMF for inter DCI applications. *Opt. Fiber Technol.* **2018**, *45*, 141–145. [CrossRef]
5. Li, H.; Hu, R.; Yang, Q.; Luo, M.; He, Z.; Jiang, P.; Liu, Y.; Li, X.; Yu, S. Improving the performance of mobile fronthaul architecture employing high order delta-sigma modulator with PAM-4 format. *Opt. Express* **2017**, *25*, 1–9. [CrossRef] [PubMed]
6. Xu, T.; Li, Z.; Peng, J.; Tan, A.; Song, Y.; Li, Y.; Chen, J.; Wang, M. Decoding of 10-G Optics-Based 50-Gb/s PAM-4 Signal Using Simplified MLSE. *IEEE Photonics J.* **2018**, *10*, 7905508. [CrossRef]
7. Zhong, K.; Zhou, X.; Huo, J.; Yu, C.; Lu, C.; Lau, A.P.T. Digital Signal Processing for Short-Reach Optical Communications: A Review of Current Technologies and Future Trends. *J. Lightwave Technol.* **2018**, *36*, 377–400. [CrossRef]
8. Ungerboeck, G. Channel coding with multilevel/phase signals. *IEEE Trans. Inf. Theory* **1982**, *28*, 55–67. [CrossRef]
9. Pillai, B.S.G.; Sedighi, B.; Guan, K.; Anthapadmanabhan, N.P.; Shieh, W.; Hinton, K.J.; Tucker, R.S. End-to-End Energy Modeling and Analysis of Long-Haul Coherent Transmission Systems. *J. Lightwave Technol.* **2014**, *32*, 3093–3111. [CrossRef]
10. Chen, B.; Lei, Y.; Liga, G.; Okonkwo, C.; Alvarado, A. Hard-Decision Coded Modulation for High-Throughput Short-Reach Optical Interconnect. *Entropy* **2020**, *22*, 400. [CrossRef] [PubMed]
11. ITU-T. Forward Error Correction for High Bit-Rate DWDM Submarine Systems. 2013. Available online: https://www.itu.int/rec/T-REC-G.975.1/en (accessed on 20 November 2021).
12. Scholten, M.; Coe, T.J.; Dillard, J. Continuously-interleaved BCH (CI-BCH) FEC delivers best-in-class NECG for 40 G and 100 G Metro applications. In Proceedings of the 2010 Conference on Optical Fiber Communication (OFC/NFOEC), Collocated National Fiber Optic Engineers Conference, San Diego, CA, USA, 21–25 March 2010; p. NTuB3.
13. Scholten, M.; Coe, T.; Dillard, J.; Chang, F. Enhanced FEC for 40 G/100 G. *Proc. ECOC* **2009**, *9*, 1–12.
14. Li, B.; Larsen, K.J.; Zibar, D.; Monroy, I.T. Over 10 dB net coding gain based on 20% overhead hard decision forward error correction in 100 G optical commnication systems. In Proceedings of the 2011 37th European Conference and Exhibition on Optical Communicatio, Geneva, Switzerland, 18–22 September 2011; pp. 1–3.
15. Northcott, P. *Swizzle, FEC for 40 G and 100 G Optical Transmission*; PMC-Sierra, Inc.: Sunnyvale, CA, USA, 2011.
16. Smith, B.; Farhood, A.; Hunt, A.; Kschischang, F.; Lodge, J. Staircase codes: FEC for 100 Gb/s OTN. *J. Lightwave Technol.* **2012**, *30*, 110–117. [CrossRef]
17. Sugihara, K.; Miyata, Y.; Sugihara, T.; Kubo, K.; Yoshida, H.; Matsumoto, W.; Mizuochi, T. A spatially-coupled type LDPC Code with an NCG of 12 dB for optical transmission beyond 100 Gb/s. In Proceedings of the OFC/NFOEC, Anaheim, CA, USA, 17–21 March 2013; pp. 1–3.
18. Chang, D.; Yu, F.; Xiao, Z.; Stojanovic, N.; Hauske, F.N.; Cai, Y.; Xie, C.; Li, L.; Xu, X.; Xiong, Q. LDPC convolutional codes using layered decoding algorithm for high speed coherent optical transmission. In Proceedings of the OFC/NFOEC, Los Angeles, CA, USA, 4–8 March 2012; pp. 1–3.
19. Dave, D. Soft-decision forward error correction in a 40-nm ASIC for 100-Gbps OTN applications. In Proceedings of the National Fiber Optic Engineers Conference, Los Angeles, CA, USA, 6–10 March 2011; p. JWA014.
20. *FEC IP Cores*; ECC66100 Series; Viasat: Cuyahoga Heights, OH, USA, 2017.
21. Djordjevic, I.; Xu, L.; Wang, T.; Cvijetic, M. Large girth low-density parity-check codes for long-haul high-speed optical communictions. In Proceedings of the National Fiber Optic Engineers Conference, San Diego, CA, USA, 24–28 February 2008; pp. 1–3.
22. Djordjevic, I.; Arabaci, M.; Minkov, L. Next generation FEC for high-capacity communication in optical transport networks. *J. Lightwave Technol.* **2009**, *27*, 3518–3530. [CrossRef]
23. Arabaci, M.; Djordjevic, I.; Saunders, R.; Marcoccia, R. High-rate nonbinary regular quasi-cyclic LDPC codes for optical communications. *J. Lightwave Technol.* **2009**, *27*, 5261–5267. [CrossRef]
24. Bergman, G. A number system with an irrational base. *Math. Mag.* **1957**, *31*, 98–110. [CrossRef]
25. Hoggatt, V. *Fibonacci and Lucas Numbers*; Houghton Mifflin: Boston, MA, USA, 1969; 92p.
26. Sergeev, I. On the Complexity of Fibonacci Coding. *Probl. Inf. Transm.* **2018**, *54*, 343–350. [CrossRef]
27. Stakhov, A. *Numeral Systems with Irrational Bases for Mission-Critical Applications*; World Scientific: Singapore, 2017; 284p.

28. Stakhov, A.; Aranson, S.; Olsen, S. *The "Golden" Non-Euclidean Geometry*; World Scientific: Singapore, 2016; 308p.
29. Borysenko, A.A.; Horiachev, O.Y.; Matsenko, S.M.; Kobiakov, O.M. Noise-immune codes based on permutations. In Proceedings of the 2018 IEEE 9th International Conference on Dependable Systems, Services and Technologies, Kyiv, Ukraine, 24–27 May 2018; pp. 609–612.
30. Borysenko, O.; Kalashnikov, V.; Kalashnikova, N. Description and applications of binomial numeral systems. *Comput. Sci. Cyber Secur.* **2016**, *2*, 13–21.
31. Knuth, D.E. An imaginary number system. *Commun. ACM* **1960**, *3*, 245–247. [CrossRef]
32. Lan, T.; Cai, Z.C. A Novel Image Representation Method under a Non-Standard Positional Numeral System. *IEEE Trans. Multimed.* **2021**, *23*, 1301–1315. [CrossRef]
33. Chang, C.H.; Sousa, L. Modular Arithmetic based Circuits and Systems for Emerging Technologies and Applications: Deep Neural Networks and Cryptography. In Proceedings of the IEEE ISCAS 2018, Florence, Italy, 27–30 May 2018.
34. Jenkins, W.K.; Soderstrand, M.A.; Radhakrishnan, C. Historical Patterns of Emerging Residue Number System Technologies During the Evolution of Computer Engineering and Digital Signal Processing. In Proceedings of the IEEE ISCAS 2018, Florence, Italy, 27–30 May 2018.
35. Olsen, E. RNS Hardware Matrix Multiplier for High Precision Neural Network Acceleration. In Proceedings of the IEEE ISCAS 2018, Florence, Italy, 27–30 May 2018.
36. Soderstrand, M.A. Contributions of Graham Jullien and William Miller to Modified Quadratic Number System Arithmetic. In Proceedings of the 2018 IEEE 61st International Midwest Symposium on Circuits and Systems (MWSCAS), Windsor, ON, Canada, 5–8 August 2018; pp. 161–164.
37. Matsenko, S.; Borysenko, O.; Spolitis, S.; Bobrovs, V. Noise Immunity of the Fibonacci Counter with the Fractal Decoder Device for Telecommunication Systems. *Latv. J. Phys. Tech. Sci.* **2019**, *56*, 12–21. [CrossRef]
38. Borysenko, A.A.; Matsenko, S.M.; Horiachev, O.Y.; Berezhna, O.V. Decoding device of Fibonacci codes in information systems. In Proceedings of the IEEE 9th International Conference on Dependable Systems, Services and Technologies (DESSERT), Kyiv, Ukraine, 24–27 May 2018; pp. 253–256.
39. Borysenko, O.; Matsenko, S. Sumy State University. Device for Decoding Fibonacci Codes. Useful Model Patent No 99587U, MPK N03M 7/36, Nou201500089, 10 June 2015. (In Ukraine)
40. Borysenko, O.; Matsenko, S.; Novhorodtsev, A.; Kobyakov, O.; Spolitis, S.; Bobrovs, V. Estimating the indivisible error detecting codes based on an average probability method. *East.-Eur. J. Enterp. Technol.* **2020**, *6*, 25–33. [CrossRef]
41. ITU-T. Spectral Grids for WDM Applications: DWDM Frequency Grid. 2012. Available online: https://www.itu.int/rec/T-REC-G.694.1 (accessed on 20 November 2021).
42. ITU-T. Characteristics of a Single-Mode Optical Fibre and Cable. 2016. Available online: https://www.itu.int/rec/T-REC-G.652 (accessed on 20 November 2021).
43. ETSI. *Digital Video Broadcasting (DVB); Second Generation Framing Structure, Channel Coding and Modulation Systems for Broadcasting, Interactive Services, Newsgathering and Other Broadband Satellite Applications (DVB-S2)*; ETSI: Valbonne, France, 2009.
44. Matsenko, S. Synthesis of Components of Digital Devices Based on the Minimal Form of the Fibonacci Code. Ph.D. Thesis, Kharkiv National University of Radio Electronics, Kharkiv, Ukraine, 2016; 150p.

6-PAPER: FPGA-Implemented Fractal Decoder with Forward Error Correction in Short-Reach Optical Interconnects

LDPC Code with Fractal Decoder Device for 100 Gbps PAM-M Optical Interconnect

Svitlana Matsenko[1], **Sandis Spolitis**[1, 2], **Oleksiy Borysenko**[3],
Mihails Pudzs[4], **Aleksandr Krotov**[2], and **Vjaceslavs Bobrovs**[2]

[1]Communication Technologies Research Center, Riga Technical University, Riga, Latvia
[2]Institute of Telecommunications, Riga Technical University, Riga, Latvia
[3]Department of Electronics and Computer Technology, Sumy State University, Sumy, Ukraine
[4]Institute of Radioelectronics, Riga Technical University, Riga, Latvia

Abstract— Modern telecommunication systems must meet the requirements for high-speed performance, low latency, reliable transfer, processing, and information storage. In line with this, the design of the optical communication systems, e.g., data center interconnects (DCI), requires high reliability of data transmission, low latency, and low overhead. It is well known that powerful forward error correction (FEC) codes with artificial redundantly being used in optical networks have several disadvantages, e.g., high-power consumption and high delays in decoder implementation. In this paper, we use an indivisible error detection code to solve these challenges, which we realized in a field-programmable gate array (FPGA) with FEC code based on the low-density parity-check (LDPC) code. Encoding and decoding methods based on the Indivisible codes are relatively less complex and capable of executing end-to-end (E2E) data control. We integrated concatenated codes into the 100 Gbps multilevel pulse amplitude (PAM-M) with Gray code mapping direct detection wavelength division multiplexed (WDM) with standard single-mode fiber (SSMF) and erbium-doped fiber amplifier (EDFA). EDFA uses for signal amplification and to investigate the code performance in the presence of ASE noise. In current conditions, strong candidates for increasing traffic are PAM-M modulation formats (e.g., PAM-4 and PAM-8) since it possesses cost-effectiveness, simplicity, spectral, and energy efficiency. We have investigated the multichannel WDM system anchored to 193.1 THz (optical C-band) central frequency, the per-channel bitrate of 100 Gbps, channel spacing of 100 GHz and EDFA with a noise figure of 3 dB. The LDPC FEC codes are simulated with code rates $R_c \in \{2/5, 3/4, 3/5, 4/5\}$ from the digital video broadcasting by satellite — second-generation (DVB-S2) standard.

1. INTRODUCTION

The task of increasing the reliability of data transmission remains urgent today, with the increase in the amount of data transmission and with the development of 4K/8K video streaming, internet of things (IoT), 5G network architecture, etc. [1]. Among a significantly large number of types of optical modulations, a powerful applicant possessing spectral efficiency, cost-effectiveness, simplicity, and energy efficiency is a pulse amplitude modulation (PAM-M) in current conditions of increasing data traffic [2–6]. For highly reliable and highly efficient modern optical communication systems, forward error correction (FEC), digital signal processing (DSP) with advanced format modulation. The use of advanced modulation formats with high spectral efficiency (SE) and strong error control coding (ECC) is one way to increase the exponential growth of Internet traffic and improve transmission coverage [7, 8]. Usually, hard-decision (HD)-FEC codes use for applications with complex requirements and severe latency (e.g., short reach) [9]. The modern soft-decision (SD)-FEC codes, which includes in many modern communication standards, for example, low-density parity-check (LDPC) code, can improve the signal-to-noise ratio (SNR) by ~ 1–2 dB at the same rate. At the same time, the task of reducing the complexity of the encoding and decoding devices that are part of the data transmission system remains essential, especially their architectural implementation in the form of an FPGA.

One of the tasks solved when using Fibonacci numbers is the development of decoding devices that detect errors in these numbers and simultaneously produce their decoding. Any typical decoder of binary numbers successfully solves this task. In this case, only logical products of variables that recognize Fibonacci numbers use in it, and all other binary numbers are perceived as erroneous, as evidenced by the absence of signals at the outputs of the decoder. This paper discusses the application of indivisible error detection codes in an optical communication system that uses relatively simple error detection methods. The indivisible code used in the studied optical communication system is implemented in the form of a fractal decoder, which provides savings in hardware costs from 10–30% compared to linear decoders based on an indivisible code based on the Fibonacci

2382

code. In this case, the connection of the block and indivisible codes is realized by the concatenation method.

2. SIMULATION MODEL WDM FIBER OPTICAL COMMUNICATION SYSTEM

Figure 1 shows the 4 WDM optical interconnect channels. The following parameters of the PAM-M WDM optical interconnect selected as the primary system parameters: 100 Gbps per-channel data rate (56 GBaud for PAM-4, and 35 GBaud for PAM-8), the central frequencies C-band set to 193.1 THz, channel spacing is chosen equal to 100 GHz frequency interval, according to the ITU-T G.694.1 recommendation [10].

The optical line terminal (OLT) consists of N — Channel Terminal (CT), which includes the N — Optical Transmitter (OT), where N — is the transmitter number. The CTs block consists of the pseudorandom bit sequence (PRBS), indivisible encoders, concatenated with LDPC FEC encoders, PAM-M with Gray code mapping, CW Laser and Mach-Zehnder modulator (MZM). Continuous wavelength (CW) light source with average power $+3$ dBm. In the simulation model, we used the Arrayed Waveguide Grating (AWGs) $N \times M$ Multiplexer/$M \times N$ Demultiplexer in the range 192.9 GHz–195.0 GHz using model type datasheet, with Gaussian passband, bandwidth — 3 dB of 75 GHz and insertion loss of 3 dB per channel. The data is being transmitted over a standard ITU-T G.652 single-mode optical fiber (SSMF) with EDFA from OLT block with attenuation coefficient — 0.2 dB/km, dispersion slope — 8 ps/(nm$^2 \times$ km), dispersion coefficient — 16 ps/nm/km, and nonlinear index — $2.6 \cdot 10$–20 m^2/W. The subscriber premises/customer premises (SP/CP) includes N — optical network terminals (ONTs), which consist of PIN receiver with thermal noise — to
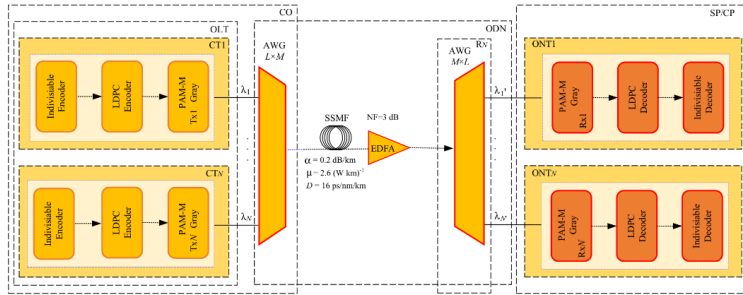
Figure 1: WDM optical interconnect model under consideration.
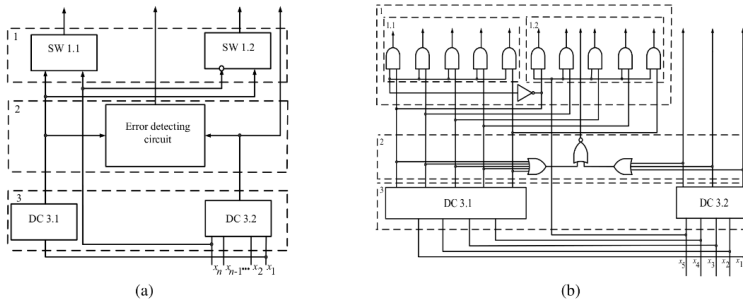
Figure 2: (a) Structural diagram of the fractal decoder device; (b) Functional diagram of the fractal decoder device.

10×10^{-12} A/Hz 1/2, 4-pole order low-pass Bessel electrical filter with $0.75\times$ Bit Rate, PAM-M with Gray code de-mapping, and LDPC decoders, concatenated with indivisible decoders.

Figure 2 shows the structural diagram of the fractal decoder device. The structural scheme of the fractal decoder device consists of a decoder 1 (DC 3.1) representing the fractal part, a decoder 2 (DC 3.2) recognizing a non-repetitive part of the Fibonacci code, an error detection circuit 2 and switching devices (SW 1.1) and (SW 1.2) intended for switching outputs of the decoder (DC 3.2) based on the value (zero or one) of the highest Fibonacci digit, respectively, to the left (DC 3.1) or right (DC 3.2) outputs of the decoding device. The operation of the circuit describes in more detail in the sources [11–14].

The absolute value of the number of the minimization of inputs of the fractal decoder

$$\begin{aligned} Q &= nF_{n+1} - (nF_n + 3F_{n-1}) = n(F_n + F_{n-1}) - nF_n - 3F_{n-1} \\ &= nF_n + nF_{n-1} - nF_n - 3F_{n-1} = nF_{n-1} - 3F_{n-1} = (n-3)F_{n-1}, \end{aligned} \tag{1}$$

where n — is a code length; $F_s = 1, 1, 2, 3, 5, 8, ..., F_n$, $F_n = F_{n-1} + F_{n-2}$ — is a Fibonacci number.

The relative value of the number of the minimization of inputs determines by the ratio Q/W.
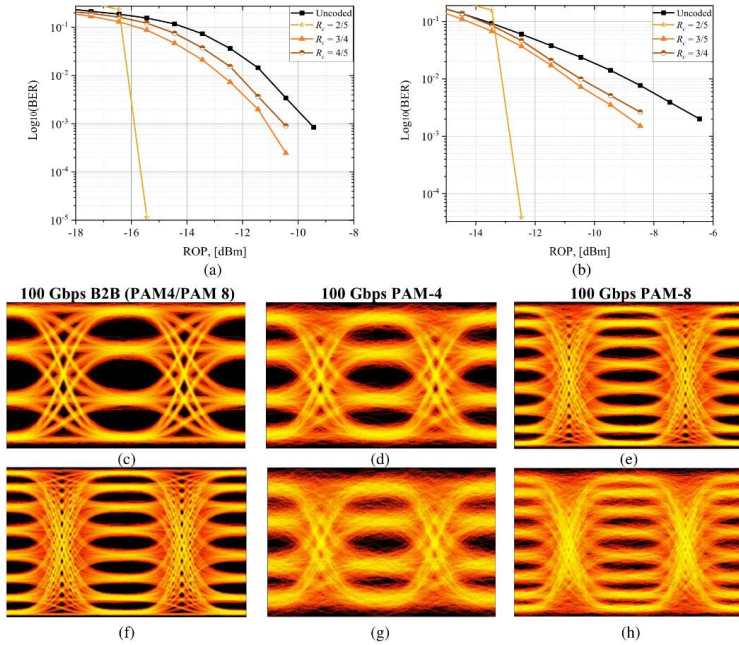
Figure 3: Post-FEC BER vs. ROP for (a) PAM-4 modulation format with $R_c \in \{2/3, 3/4, 4/5\}$; (b) PAM-8 modulation format with $R_c \in \{2/5, 3/4, 3/5\}$. The eye diagrams of received 100 Gbps B2B for (c) PAM-4 modulation format, BER $= 6.2 \times 10^{-12}$; (f) PAM-8 modulation format, BER $= 1.2 \times 10^{-6}$. The eye diagrams of received 100 Gbps and 1000 m SSMF for (d) PAM-4 modulation format, BER $= 5.3 \times 10^{-5}$; (g) PAM-4 modulated, BER $= 2.9 \times 10^{-3}$; (e) PAM-8 modulation format, BER $= 3.3 \times 10^{-5}$; (h) PAM-8 modulation format, BER $= 7.0 \times 10^{-3}$.

For the growth of n, it will tend to a value

$$\frac{Q}{W} = \frac{nF_{n+1} - (nF_n + 3F_{n-1})}{nF_{n+1}} = 1 - \frac{F_n}{F_{n+1}} - \frac{3F_{n-1}}{nF_{n+1}} \approx 1 - \frac{F_n}{F_{n+1}}. \tag{2}$$

With an increase in n, the ratio F_n/F_{n+1} approaches the value of the inverse golden section, the relative savings of the inputs of the fractal decoder device limited by the difference between this value and 1 [14].

3. NUMERICAL ANALYSIS OF THE WDM OPTICAL INTERCONNECT SYSTEM

Figure 3 shows the Post-FEC bit error rate (BER) vs ROP for PAM-M format modulations and received eye diagrams.

As seen from Figs. 3(a), (b), the most substantial error-correcting effect is the LDPC code with $R_c = 2/5$ for Figs. 3(a), (b) when applying to the HD-FEC method. The paper [12, 13] shows the evaluation of the indivisible error detection code based on the general method and the average probability method for average probabilities and n code length. This paper follows that the share of the detected errors by the Fibonacci code with increasing n tends to 1, and achieving good error detection capability. The fractal decoder device operates based on the fractal decoding method implemented in the software and design of the device.

We realized fractal decoder device in FPGA using Intel Quartus Prime with the device setup of Cyclone V 5csema5f31c6. The FPGA fitting was the realization at a clock frequency of 429.37 MHz. Fig. 4 shows the simulation waveform of the fractal decoder.

We utilized adaptive logic modules (ALMs), which, after modelling, was $10/32,070$, those less than $< 1\%$, respectively, with low power consumption. The maximum signal delay along the longest path in a combinational circuit was 0.806 ns. No digital signal processing (DSP) slices and RAM were employed. With an increase in the n of the fractal decoder, the delay time does not increase due to parallelization operations. We investigated LDPC FEC with an indivisible code and the fractal decoder for $R_c \in \{2/5, 3/4, 3/5, 4/5\}$, wherein $n = 64800$, the number of detected errors was 96%.
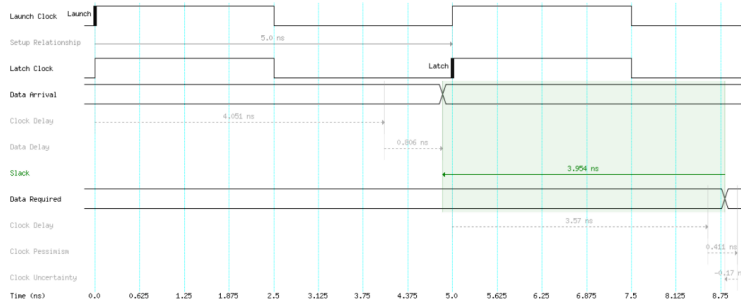
Figure 4: Simulation waveform of the fractal decoder.

4. CONCLUSIONS

This paper researched the 100 Gbps (56 GBaud for PAM-4, and 35 GBaud for PAM-8) PAM-M with Gray code mapping WDM optical interconnect system with concatenated indivisible and FEC codes. We investigated this system with SSMF and EDFA amplifier for C-band and 100 GHz channel spacing. For the LDPC FEC code, we used code rates $R_c \in \{2/5, 3/4, 3/5, 4/5\}$ from the DVB-S2 standard from ROP and received eye diagrams for PAM-4 and PAM-8 optical modulation formats. The fractal decoder device was implemented in the FPGA and tested NI Multisim software. The LDPC FEC code with $R_c = 2/5$ showed the best error correction performance. We detected 96% errors at different LDPC FEC code rates. Using indivisible codes, the possible implementation

of E2E data control is also relatively more minor complex for encoding and decoding methods. ALMs utilization was less than $< 1\%$.

ACKNOWLEDGMENT

REFERENCES

1. Effenberger, F. J., "Industrial trends and roadmap of access," *Journal of Lightwave Technology*, Vol. 35, 1142–1146, 2017.
2. Huo, J., X. Zhou, K. P. Zhong, J. Tu, J. Yuan, C. Guo, K. Long, C. Yu, A. P. T. Lau, and C. Lu, "Transmitter and receiver DSP for 112 Gbit/s PAM-4 amplifier-less transmissions using 25G-class EML and APD," *Optics Express*, Vol. 26, 22673–22686, 2018.
3. Eiselt, N., J. Wei, H. Griesser, A. Dochhan, M. Eiselt, J.-P. Elbers, J. J. V. Olmos, and I. T. Monroy, "First real-time 400G PAM-4 demonstration for inter-data center transmission over 100 km of SSMF at 1550 nm," *Optical Fiber Communications Conference and Exhibition (OFC)*, 1–3, 2016.
4. Lee, J. H., S. H. Chang, J. Y. Huh, S.-K. Kang, K. Kim, and J. K. Lee, "EML based real-time 112 Gbit/s (2×56.25 Gbit/s) PAM-4 signal transmission in C-band over 80 km SSMF for inter DCI applications," *Optical Fiber Technology*, Vol. 45, 141–145, 2018.
5. Li, H., R. Hu, Q. Yang, M. Luo, Z. He, P. Jiang, Y. Liu, X. Li, and S. Yu, "Improving performance of mobile fronthaul architecture employing high order delta-sigma modulator with PAM-4 format," *Optics Express*, Vol. 25, 1–9, 2017.
6. Xu, T., Z. Li, J. Peng, A. Tan, Y. Song, Y. Li, J. Chen, and M. Wang, "Decoding of 10-G optics-based 50-Gb/s PAM-4 signal using simplified MLSE," *IEEE Photonics Journal*, Vol. 10, 1–8, 2018.
7. Ungerboeck, G., "Channel coding with multilevel/phase signals," *IEEE Transactions on Information Theory*, Vol. 28, 55–67, 1982.
8. Szczecinski, L. and A. Alvarado, *Bit-interleaved Coded Modulation: Fundamentals, Analysis and Design*, 320, Wiley-IEEE Press, 2015.
9. Chen, B., Y. Lei, G. Liga, C. Okonkwo, and A. Alvarado, "Hard-decision coded modulation for high-throughput short-reach optical interconnect," *MDPI Entropy*, Vol. 22, No. 400, 1–19, 2020.
10. ITU-T Recommendation G.694.1, "Transmission media and optical systems characteristics characteristics of optical systems: Spectral grids for WDM applications: DWDM frequency grid," 7–12, 2012.
11. Borysenko, A. A., S. M. Matsenko, O. Y. Horiachev, and O. V. Berezhna, "Decoding device of Fibonacci codes in information systems," *IEEE 9th International Conference on Dependable Systems, Services and Technologies (DESSERT)*, 253–256, 2018.
12. Matsenko, S., O. Borysenko, S. Spolitis, and V. Bobrovs, "Noise immunity of the fibonacci counter with the fractal decoder device for telecommunication systems," *Latvian Journal of Physics and Technical Sciences*, Vol. 56, No. 5, 12–21, 2019.
13. Borysenko, O., S. Matsenko, A. Novhorodtsev, O. Kobyakov, S. Spolitis, and V. Bobrovs, "Estimating the indivisible error detecting codes based on an average probability method," *Eastern-European Journal of Enterprise Technologies*, Vol. 6, 25–33, 2020.
14. Useful Model Patent No 99587U, MPK N03M 7/36 (2006.01), Device for decoding Fibonacci codes, O. Borysenko, S. Matsenko, the applicant and patent holder Sumy State University, Nou201500089, filed 06.01.2015, issued 10.06.2015. Bul. No11. (in Ukraine).

104

7-PAPER: Possibilities for Increasing the Signal-To-Noise Ratio in Technical Vision Systems of Robotic Complexes Using Laser Structured Lighting

Possibilities for Increasing the Signal-To-Noise Ratio in Technical Vision Systems of Robotic Complexes Using Laser Structured Lighting

Aleksandr V. Krotov[1, 2], Sergei I. Artamonov[1], Victor I. Kuprenyuk[1], Viktorija M. Nikitina[1], Nikolai A. Romanov[1], Evgeny N. Sosnov[1]

Abstract – *The development of high-resolution machine vision systems with a long observation distance is an urgent task.*
The possibilities to increase the observation distance by increasing the signal-to-noise ratio (SNR) based on the use of the active parallax method are discussed in the article. The achievable observation distance in such systems is determined by the brightness of the illumination source and the ratio of the brightness of the illumination source to the brightness of the background illumination (the SNR for the photodetector pixel).
The goal of the investigation: The article considers the possibility of further increasing the SNR in machine vision systems with laser structured lighting due to the use of pulsed or repetitively pulsed mode of the backlight laser in combination with a time-gated photodetector. This allows to realize a machine vision system with gating, which will provide an increase in the observation distance due to the time cutoff of the background component of the recorded image. In the current scientific literature, the data on machine vision systems with temporal gating of the photodetector device are not known.
Methods: To consider the possibilities of increasing the SNR in vision systems, a numerical analysis by analytical formulas was used for the parameters and the operating conditions typical for robotic technical systems. The data on the number of solar photons reflected by the object and backscattering photons arising from scattering of the both solar and laser radiation were used to calculate the SNR in machine vision systems with a conventional-type matrix photodetector and with a time-gated photodetector.
Results: The calculation analysis has shown that, the using of laser illumination repetitively pulsed mode and a gated photodetector device allows to increase significantly both the SNR and the observation distance.
Practical significance: The proposed technical vision system implementation can improve the characteristics of robotic systems. **Copyright © 2018 Praise Worthy Prize S.r.l. - All rights reserved.**

***Keywords**: Signal-to-Noise Ratio, Robotics System, Machine Vision, Triangulation, Structured Lighting, Range Gating*

Nomenclature

Abbreviations

SNR	Signal-to-noise ratio
LED	Light emitting diode
MTF	Modulation transfer function

Description		*Unit of measure*
nob	Number of signal photoelectrons	
nf	Number of signal photoelectrons	
$\langle n\Sigma \rangle$	RMS value of total noise	
$\langle n_d \rangle$	RMS value of dark noise	
$\langle n_{ph} \rangle$	RMS value of photon noise	
$\langle n_{ds} \rangle$	RMS value of data sampling noise	[e]

n_{ob}	Number of signal photoelectrons	[e]
$n_{p.s}$	Number of background photoelectrons	[e]
$n_{bs.s}$	Number of backscattering solar photoelectrons	[e]
$n_{bx.l}$	Number of backscattering laser photoelectrons	[e]
F	Pulse frequency	[Hz]
L	Distance	[m]
c	Speed of light	[m/s]
$E1$	Laser pulse energy	[J]
Pcw	CW laser power	[W]
Pu	Pulse laser power	[W]
S/N	Signal to noise ratio	
$T_{oo}(v_x, v_y)$	Modulation transfer function	

328

$T_{atm}(v)$	MTF of the atmospheric path	
$T_{phd}(v)$	MTF of the photodetector	
$T_{el}(v)$	MTF of the photodetector electronics	
Greek Notations		
τi	Pulse duration	[s]
τcdr	Frame duration	[s]
τct	Strob (photodetector gate) duration	[s]
vx, vy	Angular spatial frequencies	[rad^{-1}]
α	Divergence of the laser beam	[rad]

I. Introduction

In the set of the requirements imposed on the machine vision system, the most important are: the speed of updating the information on environment, the accuracy of determining three-dimensional coordinates of observable objects, the maximum range of coordinate measurements, the cost and the reliability of the machine vision system [1]-[3].

Currently, existing machine vision systems mainly use two principles of operation: 1) systems based on triangulation methods to measure the coordinates of objects [4]; 2) systems based on time-of-flight methods to measure the coordinates of objects [5], [6]. Machine vision systems, based on triangulation measurement methods, including stereoscopic systems and systems with structured lighting have a number of practical advantages, in particular low cost and reliability [7].

The disadvantages of triangulation systems include the small range of measurements caused by a decrease in the signal-to-noise ratio (SNR) for the received signal, which is formed when external illumination is scattered from low-contrast objects.

To increase SNR in such systems, the measurement of the distance to the observed objects is based on the illumination of the observed scene by an artificially formed structured light source.

The brightest light is provided by laser sources. In addition, using a laser to form a structured illumination allows the effective filtering of the broadband background radiation through narrow-band interference filters at the input of the objective of the photodetector device [1].

Therefore, different ways to ensure an increase in the signal-to-noise ratio in a triangular type machine vision system are of great practical importance.

II. Literature Review

Active parallax method is one of the most promising methods to realize active real-time object-oriented machine vision systems for robotic complexes that uses structured lighting of the observed scene [7]. The machine vision systems based on structured lighting are made up of an illumination source and a video camera with a matrix photodetector placed at a certain distance from each other. The field of view of the video camera

and the illumination area overlap in the observation zone.

As a source of illumination, which forms a particular deterministic structure in the space of objects, video projectors, LED and laser sources are used.

The maximum range of the machine vision systems can be performed by using laser sources of illumination for structured lighting, which provides an increase in intensity at the points of the lighting structure relative to the background [8], [9].

Moreover, the monochromaticity of the laser radiation provides an effective filtering of background illumination via narrow-band interferometric filters at the input of a photodetector objective, imaging the object lighted structure at the matrix photodetector.

Also, a method of increasing the signal-to-noise ratio in the images of remote objects is known, and it is based on the use of a time-of-flight method to measure the coordinates of an object probed by the laser radiation pulse combined with a time-gated photodetector [10]-[12].

In systems of this type, the photodetector is closed at the instant of laser pulse emission and it is opened (gated) when the pulse reflected from the object arrives.

The strobe duration determines the ranges at which observed objects could be located and the exposure time of the matrix photodetector pixel by background radiation. Since the duration of the strobe is much shorter than the time between laser pulses, the exposure time by background radiation can be reduced by hundreds and thousands times [13], [14].

It is of interest to estimate the possible gain in the observation distance of a machine vision system, using the structured laser illumination that is formed by a repetitively pulsed laser and a gated photodetector.

III. Materials and Methods

Continuous wave and repetitively pulsed lasers can be used to create laser illumination. On the diagrams in Figs. 1 to 3, three different operating modes of the machine vision systems with laser illumination are presented. The upper diagram shows the mode of laser operation, the middle one shows the background illumination of the photodetector by diffused sunlight through the interference filter in front of the photodetector lens, while the lower one shows the temporal structure of the signal detected by the node pixel of the receiving photodetector (the pixel that takes laser illumination node).

Fig. 1 shows the cyclograms of machine vision systems operation illuminated by a continuous wave laser. In this case, the photodetector registers the energy accumulated during the continuous exposure of the pixel by the useful laser illumination, the laser radiation backscattered on the propagation path, and the incoherent background (solar) illumination. The exposure time of the frame is τcdr. Fig. 2 shows the cycloramas for a system illuminated by a sequence of laser pulses with duration τi and frequency *F*.
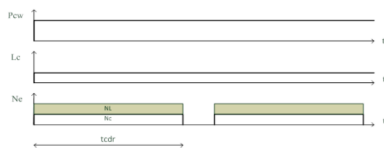
Fig. 1. MVS operation cyclogram with continuous wave laser illumination; *Pcw*: laser illumation power; *Lc*: solar background illumination power; *Ne*: instant value of the of the number of photoelectrons from one pixel of the matrix; *NL*, *Nc*: number of photoelectrons made by laser and solar background photons
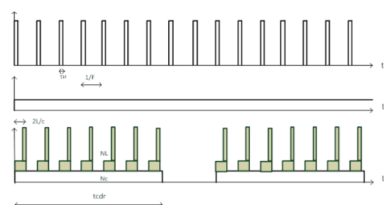
Fig. 2. MVS operation cyclogram with repetitively impulse laser illumination and non-strobed photoselector; *Pcw*: laser illumation power; *Lc*: solar background illumination power; *Ne*: instant value of the of the number of photoelectrons from one pixel of the matrix; *NL*, *Nc*: number of photoelectrons made by laser and solar background photons

In this case, the pixel of the photodetector also fixes the reflected and the scattered pulsed laser and the background components of the signal, too. The backscattered laser radiation is recorded as pulses whose duration is equal to the time of pulse propagation (flight) to the object and back 2L/c and as the reflected laser pulse with duration τi.

To compare the considered systems it can be assumed that the continuous wave and the repetitively pulsed mode of laser provide the same energy of pixel exposure per frame, i.e. the energy of one pulse $E1$ and the average power of a continuous laser Pcw coming to the node pixel of the photodetector matrix are related as $E1=Pcw/F$ and the pulse power is related by $Pi= Pcw /(F \cdot \tau i)$. Then, the number of scattered laser photons on the propagation path in exposure time τcdr will be the same for the both laser modes.

It is known that the pulsed and the repetitive pulsed operating mode of the laser in combination with a time-gated photodetector make it possible to realize a laser vision system [3], which is capable to increase the range of action of laser vision system by temporarily cutting off the background component of the recorded image. Fig. 3 shows the cycloramas for a system using the lighting by a sequence of laser pulses and a photodetector with gating duration as $\tau cm \geq \tau i$. In this case, during the frame exposure time, the pixel of the photodetector catches reflected and scattered pulsed laser and solar background

components of the signal, but the integral background exposure time decreases to $\tau ct \cdot F \cdot \tau cdr$.

In machine vision systems, using structured lightning the maximum measurement range associated with photodetector spatial resolution is limited by the noise level. Therefore, in order to compare the different machine vision systems constructions, Authors will calculate the signal-to-noise ratio (SNR) when the nodal point of the illumination structure is registered.
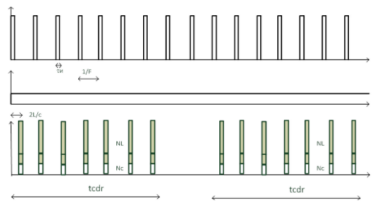
Fig. 3. MVS operation cyclogram with repetitively impulse laser illumination and non-strobed photoselector; *Pcw*: laser illumation power; *Lc*: solar background illumination power; *Ne*: instant value of the of the number of photoelectrons from one pixel of the matrix; *NL*, *Nc*: number of photoelectrons made by laser and solar background photons

For an observation system that does not use a visual analyzer, the SNR reduced to one pixel of the photodetector is determined as follows [15]:

$$(S / N) = \frac{|\bar{n}_{ob} - \bar{n}_f|}{\langle n_\Sigma \rangle} T_{sys}(v_x, v_y) \qquad (1)$$

where:
- *nob*, *nf* is the average number of signal and background photoelectrons accumulated during exposure time in one pixel of the photodetector matrix;
- $\langle n\Sigma \rangle$ is the RMS value of total noise in the receiving channel, reduced to the pixel of the photodetector matrix, expressed in electrons;
- *Tsys*·(*vx, vy*) is the modulation transfer function (MTF) of receiving channel;
- *vx, vy* is the angular spatial frequencies of the observed object.

The MTF of the receiving channel is a product of transfer functions of the optical path, the atmospheric path, the photodetector, and of the electronic circuit of amplification and digitization of the signal. Formulas for the calculation of transfer functions are given in [8] (Section 9.1).

In machine vision systems signal, photoelectrons are electrons obtained by converting laser photons reflected from the surface of an object in an illumination node, background photoelectrons are electrons obtained by the conversion of backscattered photons, reflected solar photons and scattered solar photons.

The total pixel noise of the photodetector matrix is made up of dark noise (n_d), photon noise (n_{ph}) and data sampling noise at the output of the photodetector (n_{ds}) [8]:

$$\langle n_\Sigma \rangle = \sqrt{\langle n_d \rangle^2 + \langle n_{ph} \rangle^2 + \langle n_{ds} \rangle^2} \qquad (2)$$

The dark noise is determined by specification of the photodetector matrix. For high-sensitivity matrices, the average value of dark noise does not exceed 10 photoelectrons per pixel with an exposure of about 20 ms.

To compare SNR values of various machine vision systems, authors can suggest the sampling noise and dark noise sum equal to 10 photoelectrons per pixel.

As a rule, the photon noise predominates in the photodetector. To determine the dispersion $\langle n_{ph} \rangle^2$ caused by optical radiation fluctuations, it is necessary to calculate the average number of signal n_{ob} and background photoelectrons $n_{p.s}$ generated by reflecting the laser and solar radiation from the surface of the object as well as by backscattering the solar and laser radiation in the atmosphere (air environment) $n_{bs.s}$, $n_{bs.l}$.

So:

$$\langle n_{ph} \rangle = \sqrt{\frac{\overline{n_{ob}} + \overline{n_{p.s}} + \overline{n_{bs.s}} + \overline{n_{bs.l}}}{2}} \qquad (3)$$

and (eq. (4)):

$$(S/N) = \frac{\overline{n_{ob}} - \overline{n_{p.s}}}{\sqrt{\langle n_m \rangle^2 + \frac{1}{2}\left(\overline{n_{ob}} + \overline{n_{p.s}} + \overline{n_{bs.s}} + \overline{n_{bs.l}}\right) + \langle n_{ds} \rangle^2}} T_{sys}(\nu) \qquad (4)$$

In [6] (Sections 9.1, 11.3) the ratios are enabled to calculate the number of photoelectrons and MTF values:

$$T_{sys}(\nu) = T_{atm}(\nu) T_{phd}(\nu) T_{el}(\nu) \qquad (5)$$

where $T_{atm}(\nu)$ is the MTF of the atmospheric path, $T_{phd}(\nu)$ is the MTF of the photodetector and $T_{el}(\nu)$ is the MTF of the photodetector electronics.

For machine vision systems, the most interesting parameter is the function transfer of spatial frequencies corresponding to the angular size of the illumination structure node at distance ensuring a reliable node registration.

If the probability of detection is equal to 0.8 this condition is ensured at the angular spatial frequency $\nu_{0,8} \cong 2/\alpha$, where α is the total divergence of the laser beam forming the illumination node.

IV. Results

To estimate the achievable gain in machine vision systems operation range achieved by time-gating photodetector, in this paper a numerical comparative analysis for schemes without and with gating of the photodetector has been performed.

In Figs. 4-6 the results of the calculation of the number of photoelectrons and the signal-to-noise ratio in dependence of observation distance z are given under the following conditions for two considered schemes:

1. machine vision systems operates on an atmospheric path with average weather conditions at a meteorological range of visibility of 10 km, without atmospheric precipitation.
2. machine vision systems use a laser with 1.06 μm wavelength and average power Pcw to create a structured lightning. The structure of the illumination is a rectangular N×N~50×50 pixels grid, generated using a two-dimensional Dammann grid installed at the output of the laser beam forming system with a diameter of 15 mm at least. In the results given below, beam divergence was supposed to be 140 μrad. The laser was capable to operate in both the continuous waves and repetitively pulsed modes with the repetition rate up to 4 kHz providing 0.5 to 10 W power level. The results are obtained for the power of 4 W. The pulse duration in the calculations was assumed to be $\tau i=$ 10 ns, while the duration of the gating interval was assumed to be $5\tau i$.
3. a bistatic illumination scheme with the laser and photodetector 0.5 m spacing distance was considered.
4. a video camera with a matrix photodetector operating at 25 frames per second was used to record the information about reflected laser radiation structure. The angular size of the matrix pixel was assumed to be equal to 75 μrad; the quantum efficiency was equal to 0.5, and the diameter of the objective entrance pupil was 10 mm. At the objective entrance, an interference filter to the laser wavelength was set and the filter bandwidth was 5 nm.

V. Discussion

Figs. 4 and 5 show the dependences of the number of photoelectrons per pixel on the observation distance z for system versions without time-gating and with gating. It can be seen that for the system without gating the sunlight from the object and the backscattered sunlight exceed in the total the useful signal beginning from distances of about 50 m.

In this case, as it can be seen from Fig. 6, the signal-to-noise ratio decreases rapidly with the increase of the distance. It is known that, to ensure reliable recognition of an object, it is necessary to provide a signal-to-noise ratio exceeding 7 to 10.

Thus, under conditions accepted in calculations, in machine vision system without gating, the observation range cannot exceed 50 to 60 m.
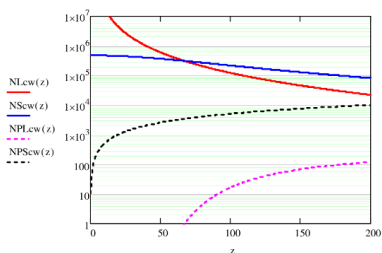
Fig. 4. The number of electrons per matrix pixel with using continuous wave laser lightning and repetitively pulsed lightning without gating. *NLcw, NScw* are the number of laser and solar photoelectrons reflected from the object, *NPLcw, NPScw* are the number of laser and solar backscattered photoelectrons. The abscissa distance is expressed in meters
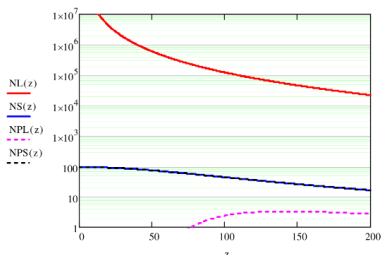

Fig. 5. The number of electrons per matrix pixel with using laser repetitively pulsed lightning and a photodetector with gating. *NL, NS* are the number of laser and solar photoelectrons reflected from the object, *NRL, NPS* are the number of laser and solar backscattered photoelectrons. The abscissa distance is expressed in meters
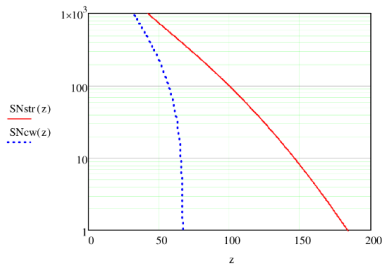
Fig. 6. Signal-to-noise ratio for machine vision systems without gating (dashed) and with gating (solid line) on (to) the observation distance. The abscissa distance is expressed in meters

As it can be seen from the comparison of Figs. 4 and 5, the passage to a system with gating gives the following

result: the background sunlight from the object is weakened several thousand times, the backscattered solar radiation is practically absent and the level of backscattering of the laser radiation is reduced by two orders of magnitude. This is resulted from the fact that, when the pulse width is 10 ns, the duration of the strobe is 50 ns and the interval between pulses is 250 microseconds (repetition rate is 4 kHz), the total exposure time of the pixel at gating mode decreases by a factor of 5000.

As a result, as it can be seen from Fig. 6, at SNR = 10, which ensures a confident recognition of the object, the observation range for the system with gated photodetector increases to 150 m, i.e. in 2,5 times.

VI. Conclusion

The numerical analysis presented has shown that, in machine vision systems with structured lightning, it is expedient to use the repetitively pulsed mode of the illumination laser in combination with the time-gated photodetector. The use of such system can allow to increase significantly (1.5 ... 3 times) the observation range due to the reduction of background noise.

Acknowledgements

References

[1] Carsten Steger, Markus Ulrich, Christian Wiedemann (2018). *Machine Vision Algorithms and Applications* (2*nd ed.*). Weinheim: Wiley-VCH. p. 1.
[2] Arun Kumar, Nitin Chauhan. Rewiew on application of mashine vision. *International Journal of Mechanical Engineering and Technology (IJMET)*. Volume 8, Issue 7, July 2017, pp. 1710–1717.
[3] Chen F., Brown G., Song M. Overview of three dimensional shape measurement using optical methods. *Opt. Eng.* 2000; 39:10–22.
doi: 10.1117/1.602438
[4] R. I. Hartley and P. Sturm, *Triangulation, Computer vision and image understanding*, Vol. 68, No. 2, November, pp. 146–157, 1997.
[5] S. May, D. Droeschel, D. Holz, S. Fuchs, E. Malis, A. N¨uchter, J. Hertzberg, Three-dimensional mapping with time-of-flight cameras. Journal of Field Robotics, *Special Issue on Three-Dimensional Mapping*, Part 2 26 (11-12) (2009) 934–965.
[6] Pagès J., Collewet C., Chaumette F., Salvi J. A camera-projector system for robot positioning by visual servoing; *Proceedings of the 2006 Conference on Computer Vision and Pattern Recognition Workshop* (CVPRW 2006); New York, NY, USA. 17–22 June 2006.
[7] N. A. Gryaznov, V. V. Kirichenko. Volumetric technical vision for autonomization of ground-based robotic systems, *Proc. IX Vseross. scientific and technical. Conf. "Extreme robotics*, SPb, 2006, p. 281.
[8] N. A. Gryaznov, D. A. Kochkaryov, E. N. Sosnov. *Laser-television triangulation system of three-dimensional positioning*

on the basis of a high-speed television camera, Scientific and technical lists of the St. Petersburg State Polytechnic University ("LETI"), SPb, 2013, p. 215.

[9] Sturm J., Konolige K., Stachniss C., Burgard W. 3D pose estimation, tracking and model learning of articulated objects from dense depth video using projected texture stereo; *Proceedings of the 2010 RGB-D: Advanced Reasoning with Depth Cameras Workshop*; Zaragoza, Spain. 27 June 2010.

[10] V. E. Karasik, V. M. Orlov. *Locating laser vision systems*. (Moscow, Izd. MSTU them. N.E. Bauman, 2013).

[11] May S., Werner B., Surmann H., Pervolz K. 3D time-of-flight cameras for mobile robotics; *Proceedings of the 2006 IEEE/RSJ International Conference on Intelligent Robots and Systems* (IROS 2006); Beijing, China. 9–15 October 2006; pp. 790–795.

[12] S. Inbar and O. David, *Laser Gated Camera Imaging System and Method*, Patent Application, WIPO WO 2004/072678 A1

[13] Christnacher Frank, Schertzer Stéphane, Metzger Nicolas, Bacher Emmanue, Poyet Jean-Michel. On the real performance of SWIR range-gated active imaging in scattering media. *Proceedings of the SPIE*, Volume 9987, id. 998702 10 pp. (2016). DOI: 10.1117/12.2240763.

[14] M. H. Ettenberg, R. M. Brubaker, M. A. Blessinger, and V. J. Burzi, A 320x256 InGaAs Camera for Range Gated and Staring Applications, presented at *SPIE Conference on Defense and Security*, Orlando, 2005.

[15] Liang Weiwei, Chen Qianrong, Hao Yongwang, Guo Hao, Zhang Wenpan. Simulation of signal-to-noise ratio for the laser range-gated imaging system. *Proceedings of the SPIE*, Volume 9674, id. 967417 7 pp. (2015). DOI: 10.1117/12.2199353

Authors' information

[1]The Russian State Scientific Center for Robotics and Technical Cybernetics (RTC), Russia.

[2] Saint Petersburg Electrotechnical University "LETI", Russia.

Aleksandr V. Krotov
e-mail: a.krotov@rtc.ru
St. Petersburg Electrotechnical Univeristy (2012)
Laser Lidars, Laser Vision Systems, Robot Vision Systems
www.rtc.ru

Sergei I. Artamonov
e-mail: s.artamonov@rtc.ru
State University of Aerospace instrumentation (2012)
Laser Lidars, Laser Vision Systems, Robot Vision Systems
www.rtc.ru

Victor I. Kuprenyuk
e-mail: v.kuprenuk@rtc.ru
Leningrad Electrotechnical Inst. (1971),
Ph. D. in optics (1980)
Lasers, Laser Optics, Laser Lidars, Laser Vision Systems, Robot Vision Systems
www.rtc.ru

Viktorija M. Nikitina
e-mail: v.nikitina@rtc.ru
ITMO University (2014)
Robot Vision Systems
www.rtc.ru

Nikolai A. Romanov
e-mail: n.romanov@rtc.ru
Moscow Physical-Technical Inst. (1978)
Lasers, Laser Lidars, Robot Vision Systems
www.rtc.ru

Evgeny N. Sosnov
e-mail: e.sosnov@rtc.ru
Leningrad State University (1980)
Lasers, Laser Lidars, Robot Vision Systems
www.rtc.ru

8-PAPER: Method   for   measuring distortion in wide-angle video channels

METHOD FOR MEASURING DISTORTION IN WIDE-ANGLE VIDEO CHANNELS

Aleksander Krotov* Dmitry Volkov Nikolay Romanov Nikolay Gryaznov Evgeny Sosnov Dmitry Goryachkin

St. Petersburg Electrotechnical University ("LETI"), The Russian State Scientific Center for Robotics and Technical Cybernetics (RTC), Russian Federation

Methods for correcting aberrations of images, obtained by an optoelectronic camera with the use of preliminary measured calibration function, provoke wide interest in recent years. For the most part these methods are not characterized by high accuracy and are typically used for cameras with objectives having rather high relative distortion. In this article the method is discussed for measuring distortion of a wide-angle objective for calibration of photoelectric cameras designed to measure angular coordinates of remote objects with the accuracy as high as 10 arcseconds. It is proposed to use an air mirror-wedge as a test object, which allows creating a sheaf of collimated beams. The calibration function of a photoelectric camera is calculated by mathematical post-processing of the recorded frames. The proposed method was experimentally tested for photoelectric cameras with full angular fields-of-view of 21 degrees and angular pixel sizes of 20 arcseconds. The subpixel accuracy of determining the calibration function is demonstrated.

Key words: Distortion, Radial distortion, Numerical optimization, Image correction, High accuracy, Calibration function

INTRODUCTION

For high precision measurements of remote objects angular coordinates, in particular for astronomical measurements with using photoelectric registration, it is necessary to take into consideration the image aberrations resulted from imperfect optics at the stage of recorded frames processing. The significant contribution to image aberration, especially for wide-angle lenses, results from distortion of optical systems.

A method for in-laboratory distortion measurement of wide-angle cameras for electronic theodolites is considered in this paper. To create a test light source it is proposed to use an air mirror-wedge (AMW) formed by two plane-parallel plates. The method is characterized by universality, simplicity and efficiency, as well as by the low cost of the equipment necessary for its implementation.

LITERATURE REVIEW

To take into account the distortion, a camera consisting of a wide-angle objective and a photoelectric array is typically calibrated using a test light source whose angular coordinates of the elements are known with the required accuracy. There are a lot of investigations are devoted to measuring the image distortion [01-15]. Most of them deal with calibration of photoelectric cameras for surveying at a finite distance, and are not intended for accurate measurements of angular coordinates.

The most popular methods of distortion measurement are usually designed to investigate sufficiently large geometric distortions of the image (more than 1%) with a relatively small accuracy [01, 02, 04-10, 13-15] or to measure distortion with a high accuracy, but only for narrow field-of-view optical systems [03].

In this article the method is considered for calibration of wide field-of-view video channels for electronic theodolites, intended for measurements of angular coordinates with the accuracy better than 10 arcseconds. The A test light source in this case should consist of a set of point sources located in the far-field zone. Their angular coordinates should be a priori known with the accuracy not worse than 2-3 arcseconds. The point sources should fill totally the field-of-view of the video channel.

The most commonly used test object for calibration of wide-angle cameras intended for measuring the angular coordinates of remote objects is the stellar sky [16]. The calibration based on the stellar sky survey must be carried out in the field at night and requires using of high precision clocks and accurate positioning of the calibrated camera.

The method considered in this article provides a high-precision and simple measurement of distortion even in orthoscopic optical systems with a basic level of relative distortion not exceeded fractions of a percent. A description of the method and experimental results of distortion measurement of wide-angle cameras with an angular field-of-view up to 21 degrees (full angle) and relative distortion at edges of the field-of-view not exceeded 0.3 percent are presented below.

* St. Petersburg Electrotechnical University ("LETI"), ul. Professora Popova 5, 197376 St. Petersburg, Russian Federation
a_krotov_k@mail.ua

274

MATERIALS AND METHODS

The optical schematic for distortion measurement of wide-angle photoelectric cameras is shown in Figure 1. AMW 4, formed by two plane-parallel plates is used as a test light source. The angle between the plates is α. The interior plate surfaces are covered with partially reflective coatings with a reflection coefficient of 85 percent in the operating spectral range. The outer surfaces of the plates are antireflection coated.

Figure 1: Optical schematic for distortion measurement of wide-angle photoelectric cameras.

1 - light source,

2 - diaphragm,

3 - collimator,

4 - air mirror-wedge,

5–tested photoelectric camera

The beam with a plane wave front formed by collimator 3 falls onto the AMW. A sheaf of equidistant collimated beams separated by the angles equal to double wedge angle *α* is formed at the AMW output.

In the focal plane of the photoelectric camera objective (video channel), the beam sheaf is imaged as a chain of focal spots ("star track"). The focal spot corresponding to the non-deflected beam is located near the point of intersection of the optical axis of the objective and the focal plane. When the video channel or the AMW is rotated around the axis, the orientation of the "star track" in the frame changes. Thus, several frames are recorded to fill uniformly the field-of-view of the photoelectric camera with star tracks, as shown in Figure 2.
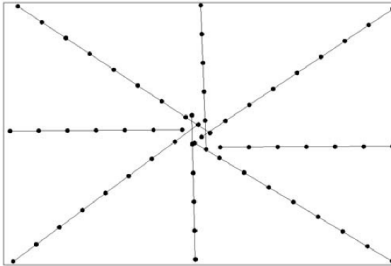
Figure 2: Filling field of view of the photoelectric camera (video channel) with "star tracks". A straight line for clarity connects the focal spots of each of the tracks

For calibration of the video channel during the subsequent processing of the recorded frames the coordinates of pixels corresponding to the energetic gravity centers of the "star track" focal spots for each frame are calculated. Also, angle of the "star track" slope *γ* relative to horizontal axis X of the matrix is calculated in the frame by the least squares method.

To calculate the radial distortion, a seventh-order distortion model was used. In "pixel" units of measurement, this model can be written in the following form:

$$N_d = N_u \cdot \left(1 + K_3 \cdot N_u^2 + K_5 \cdot N_u^4 + K_7 \cdot N_u^6\right) \quad 1)$$

where N_d is the "measured" (distorted) distance from the gravity center of the focal spot to the camera axis, N_u is the "undistorted" position of the focal spot K_3, K_5, K_7 are respectively the third, fifth and seventh order distortion coefficients.

The "measured" distance N_d is related to the video channel parameters by the following ratio:

$$N_d = \sqrt{(X_m - X_c)^2 + (Y_m - Y_c)^2} \quad 2)$$

where X_m, Y_m, are the measured values of the coordinates of the gravity center pixel of mth focal spot X_c, Y_c, are the coordinates of the camera axis pixel.

The following ratio relates the "undistorted" position of the focal spot N_u to the video channel parameters:

$$N_u = \frac{F \cdot tan(\theta)}{d_{pix}} \quad 3)$$

Here *F* is the focal distance of the video channel, θ is the angle between the axis of the objective and the axis of the given sheaf beam, d_{pix} is the pixel size.

Since aberrations introduced by distortion are negligibly small for the non-deflected beam in the sheaf (the first beam), angle θ_0 between the axis of the objective and the axis of this beam is related to the coordinates of the gravity center of the spot and the parameters of the video channel, as follows:

$$tan(\theta_{x0}) = \frac{(X_{d0} - X_c) \cdot d_{pix}}{F} \quad 4)$$

$$tan(\theta_{y0}) = \frac{(Y_{d0} - Y_c) \cdot d_{pix}}{F} \quad 5)$$

$$tan(\theta_0) = \sqrt{tan^2(\theta_{x0}) + tan^2(\theta_{y0})} \quad 6)$$

where X_{d0}, Y_{d0}, are the measured coordinates in pixels of the gravity center of the focal spot for the first beam.

275

114

The coordinate system of the video channel is defined as follows: X-axis of the video channel is parallel to X-axis of the matrix, Y-axis of the video channel is parallel to Y-axis of the matrix, Z-axis of the video channel coincides with the axis of symmetry of the objective (the radial distortion axis).

The unit vector of the axis direction of jth beam in the sheaf in the coordinate system of the video channel is determined by the formula:

$$K_j = \begin{pmatrix} \cos(\gamma)\cdot\sin(2\cdot(j-1)\cdot\alpha-\psi) - \sin(\gamma)\cdot\sin(\varphi)\cdot\cos(2\cdot(j-1)\cdot\alpha-\psi) \\ \sin(\gamma)\cdot\sin(2\cdot(j-1)\cdot\alpha-\psi) - \cos(\gamma)\cdot\sin(\varphi)\cdot\cos(2\cdot(j-1)\cdot\alpha-\psi) \\ \cos(\varphi)\cdot\cos(2\cdot(j-1)\cdot\alpha-\psi) \end{pmatrix} \quad 7)$$

Here γ is the angle of inclination of the "star track" in the frame relative to X-axis of the matrix, ψ is the angle between the first beam and the projection of the axis of the photoelectric camera on the plane in which the sheaf of beams lies (sheaf plane), φ is the angle between the axis of the video channel (the axis of the objective) and the sheaf plane.

The angles of orientation of the sheaf plane relative to the camera's coordinate system (ψ and φ) are related to the coordinates of the first beam and the orientation of the "star track" in the frame with the following ratios:

$$\tan(\varphi) = \cos(\gamma)\cdot\tan(\theta_{y0}) - \sin(\gamma)\cdot\tan(\theta_{x0}) \quad 8)$$

$$\tan(\psi) = -\frac{\cos(\gamma)\cdot\tan(\theta_{x0}) + \sin(\gamma)\cdot\tan(\theta_{y0})}{\sqrt{1 + \left(\cos(\gamma)\cdot\tan(\theta_{y0}) - \sin(\gamma)\cdot\tan(\theta_{x0})\right)^2}} \quad 9)$$

Finally, the angle between the axis of the jth beam in the sheaf and the axis of the video channel is given by:

$$\cos(\theta_j) = K_{j_z} \quad 10)$$

To find the camera parameters and distortion coefficients by the Levenberg-Marquardt method, the optimization problem for equation (1) is solved for each focal spot from each frame of "star track" recording with taking into account the interrelation of the quantities described by expressions (2 - 10). The most probable values of the following parameters are determined: the focal length of the camera F, pixel coordinates of the axis of the video channel X_c, Y_c, (the symmetry axis of the distortion function), and the third, fifth and seventh order distortion coefficients K_3, K_5, K_7.

RESULTS

Experimental measurements of the distortion according to the presented method were carried out with video channels of two types differing by image sensors and objectives [17, 18]. Both objectives were specially designed for use in electronic theodolites, and therefore they were subjected to high demands in terms of distortion correction and uniformity of an image quality throughout the field, including corners of the frame. Technical characteristics of video channels, including parameters of video sensors and optical objectives, used in the investigated video channels, are given in Table 1.

For both objectives the distortion was corrected almost completely and even in the corners of the frame it did not exceed 0.3 percent. The difference between the paraxial and real position of the image of any point did not exceed 20 μm (almost along the full field its value ranges from 0 to 8 μm). This is less or comparable to the size of a single pixel of the image sensor, which was 7.4 μm in video channel 1, and 5.5 μm in video channel 2. Below, in Figure 5, the calculated distortion function is given with the ideal accuracy of assembling the objectives.

At achieved level of distortion correction a high-precision measurement of the geometrical distortions of the optical system should be made taking into consideration the contribution of asymmetric aberrations of broad beams, as well as inaccuracy in the components manufacture, and errors in assembly and alignment of the both objectives and video channels.

Considering this, in the both objectives special attention was paid to minimizing coma aberrations and field curvature, and their design included adjustment movements of the most sensitive optical components, which made it possible to achieve uniformity and high resolution in the video channels over the full frame. The curves of polychromatic modulation transfer function (MTF) of the objectives are shown in Figure 3.
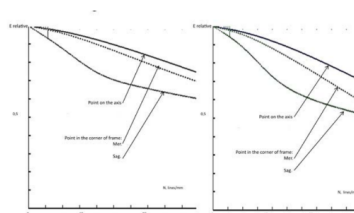

Figure 3: MTF of video channel No.1 lenses (left) and video channel No.2 (right)

The test sheaf of beams was created with the use of a collimator from a standard optical bench (focal length 1600 mm, light diameter 150 mm) and an AMW. The AMW was formed by two plane-parallel plates of BK7 glass with the diameter of 80 mm and the surface optical quality N = 0.1, ΔN = 0.1. Plates were assembled in a mount, which provided possibility to adjust the angle between the plates and to fix them rigidly after that.

The maximum number of beams in the sheaf was limited by the optical quality of the surfaces of the AMW plates. Multiple reflections from mirror surfaces of the AMW result in distortions of the beam wavefront, which arise due to surfaces imperfectness and accumulate (practically add up together). For the AMW unit used in our experiments, the angular divergence of the beam after 9 reflections (beam number 9) turns out to be unacceptably large. Therefore, the value of AMW angle was chosen so that a half angle of the field of view of the video channel comprises nine beams (that is, there are nine focal spots in the half image diagonal). For example, to measure the distortion of video channels No. 2, the angle between the plates was chosen about 40 arcminutes. The AMW angle was measured using a goniometer with the accuracy not less than 0.5 arcsecond.

Note that the AMW must be set in such a way that its edge should be perpendicular to the input beam axis. Deviation from the perpendicularity $\delta\varphi$ will lead to error $\delta\alpha$ in angle 2·α between the adjacent beams so that $\delta\varphi \sim \sqrt{\frac{\delta\alpha}{\alpha}}$. As estimations show, the requirements on the perpendicularity are not rigid. For example, if $\delta\alpha$ = 0.1 arcsecond and α = 40 arcminutes, the permissible deviation in the AMW edge perpendicularity to the input beam axis is $\delta\varphi \sim$ 22 arcminutes. During the measurement of the distortion of video channels the edge of the AMW was set perpendicular to the axis of the incident beam using the autocollimator with the accuracy better than 10 arcseconds.

For each video channel the eight successive frames were recorded with different orientations of the "star track" in the frame field in accordance with Figure 2. As indicated above, the following values were calculated as a result of mathematical processing of these frames: camera focal length F, pixel coordinates X_c, Y_c of the video channel axis (axis of symmetry of the distortion function) and third, fifth and seventh order distortion coefficients K_3, K_5, K_7 (see 1-10).

Figure 4 shows an example of the results of the distortion measurement for one of the video channels 2.

The solid curve represents the calibration function of the video channel (distortion function) calculated using ratio:

$$D_{cal}(\theta) = K_3 \cdot \left(\frac{F\cdot\tan\theta}{d_{pix}}\right)^3 + K_5 \cdot \left(\frac{F\cdot\tan\theta}{d_{pix}}\right)^5 + K_7 \cdot \left(\frac{F\cdot\tan\theta}{d_{pix}}\right)^7 \quad 12)$$

The points in Figure 4 correspond to focal spots of the sheaf of beams and show the measured value of the distortion $D_{exp}(\theta)$ for each focal spot. The position of each point was calculated using ratio:

$$D_{exp}(\theta) = \sqrt{(X_m - X_c)^2 + (Y_m - Y_c)^2} - \frac{F\cdot\tan\theta}{d_{pix}} \quad 13)$$

The root-mean-square deviation of the measured distortion values of the focal spots from the calibration function of the video channel shown in Figure 4 was 0.098 pixels.
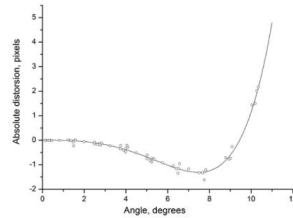
Figure 4: The calibration function of the video channel (distortion function, solid line) calculated according to the results of measurements. The circles show positions of the focal spots of the "star tracks"

DISCUSSION

As mentioned above, the proposed method was verified by calibration of several wide-angle video channels developed by the authors of this paper. Figure 5 shows comparison of the measurement results and the theoretical function of distortion.

In Figure 5 the solid curve shows the distortion function for the objective with the ideal accuracy of assembling. The dotted lines show the calibration functions obtained from the results of measurements for 15 video channels No. 2.
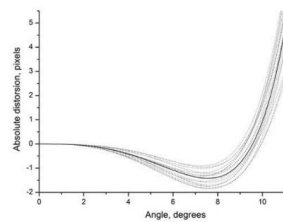
Figure 5: Distortion function (solid line) calculated for ideal assembling the objective. Dotted lines show calibration functions for 15 video channels

Table 1: Technical specifications of video channels

Technical specifications	Video channel No. 1	Video channel No.2
Video Sensor	KAI-4021 IMAGE SENSOR	KAI-08051 IMAGE SENSOR
Number of Active Pixels	2048×2048	3296×2472
Pixel Size	7.4µm×7.4µm	5.5 µm×5.5 µm
Linear size of the image receiver, mm	15.15×15.15 (diagonal 21.43)	18.13×13.60 (diagonal 22.66)
Focal length of the objective, mm	80 (objective17)	60.1 (objective18)
Angular pixel size, arcsec	19'	18.75'
The largest diameter of the entrance pupil, mm	61	46
f-number	f/1.3	f/1.3
Spectral range, nm	680 – 820	680 – 820
Field-of-view, degree	16	21.3
Number of elements/groups	8/7	8/7
Length / diameter, mm	150/68	134/56

NOMENCLATURE

Abbreviation		
AMW	Air mirror-wedge	
MTF	Modulation transfer function	
Description		Unit of measure
α	angle of the air mirror-wedge	rad
γ	angle of the "star track" slope	rad
N_d	"measured" (distorted) distance in "pixel" units	
N_u	"undistorted" position of the focal spot in "pixel" units	
K_3, K_5, K_7	third, fifth and seventh order distortion coefficients	
X_m, Y_m	measured coordinates of the spot gravity center in pixels	
X_c, Y_c	coordinates of the axis in pixels	
F	focal distance of the video channel	mm
θ	angle between the axis of the objective and the axis of the beam	rad
d_{pix}	pixel size	mm
θ_0	angle between the axis of the objective and the axis of the first beam of the sheaf	rad
X_{d0}, Y_{d0}	measured coordinates in pixels of the focal spot for the first beam	
ψ	angle between the first beam and the projection of the axis of the objective on the sheaf plane	rad
φ	angle between the axis of the objective and the sheaf plane	rad
θ_j	angle between the axis of the jth beam in the sheaf and the axis of the objective	rad
Kj	unit vector of the axis direction of jth beam	
δφ	deviation from the perpendicularity of the input beam axis to AMW edge	
δα	error in angle 2·α between the adjacent beams of the sheaf	
$D_{cal}(\theta)$	calibration function of the video channel	
$D_{exp}(\theta)$	measured value of the distortion	

As can be seen, the maximum deviations of the measured calibration functions of the video channels from the calculated distortion function are about 0.5 pixels, that corresponds to ≈10 arcseconds in terms of angular units and less than 3 μm in linear units. Apparently, these differences are associated with errors in the manufacture of optical components and an inaccuracy in assembling the system within the tolerances of the mutual position of the optical components of the system. As the Monte-Carlo calculations showed, within allowable deviations in the assembly accuracy the measured distortion positions of the focal spots in the photodetector plane differ from the calculated ones by values not exceeding 3 μm.

As follows from the results of measurements of the distortion function, the proposed method makes possible to determine the calibration function with the sub-pixel accuracy. The AMW allows to use both monochromatic and broadband light sources for channel calibration.

CONCLUSION

The method, proposed in the paper, makes it possible to derive theoretically and experimentally the calibration function for wide-angle video channels with objectives having small relative distortion. The calibration function derived in such a way can be used for image correction as well as for precise calculation of angular coordinates of the targets in a frame.

The method is characterized by universality, simplicity and efficiency, as well as by the low cost of the equipment necessary for its implementation.

It is worth noting that the method proposed fits objectives with the symmetric function of distortion. There are precisely those wide-angle objectives of sufficiently high optical quality, which are used in electronic theodolites.

ACKNOWLEDGMENTS

REFERENCES

1. GOST 20825-75. Objectives for photography. Method of measuring distortion. (1976), from http://docs.cntd.ru/document/1200015646, accessed on 2018-01-23.

2. Zhimbueva, L.D. (n.a.). Method of determination of summary distortion of digital images. Computer Optics, vol. 1, no. 3, 347-355.

3. Kozhin, A.V., Zavyazkin, V.F., Silant'eva, N.S. (2006). Method of determination of distortion of long-focus objectives. PatentRU No.2276778. JSC "Krasnogorsky Zavod", Krasnogorsk, from http://www.freepatent.ru/patents/2276778, accessed on 2017-11-21.

4. Cattaneo, C., Mainetti, G., Sala, R. (2015). The importance of camera calibration and distortion correction to obtain measurements with video surveillance systems. Journal of Physics: Conference Series, vol. 658, no. 1, DOI: 10.1088/1742-6596/658/1/012009, from https://www.researchgate.net/publication/284204844_The_Importance_of_Camera_Calibration_and_Distortion_Correction_to_Obtain_Measurements_with_Video_Surveillance_Systems?_sg=JohWRHlkQ8VHPkRhmh2JGXlcn4SadAHMBnCQkYizrrq-42ZAIlYi7S4Yk_e2oXDHaCifHMvfN7VzriY, accessed on 2017-12-20.

5. Reznicek, J. (2014). Method for measuring lens distortion by using pinhole lens. The International Archives of the Photogrammetry, Remote Sensing and Spatial Information Sciences, vol. XL-5, no. 5, 509-515, DOI: 10.5194/isprsarchives-XL-5-509-2014, from https://www.researchgate.net/publication/274676151_Method_for_Measuring_Lens_Distortion_by_Using_Pinhole_Lens?ev=publicSearchHeader&_sg=BiBS0sMJKgrHbyy1XmfN6sTGI7wbu8QADfKwGcZ6lke9Z-kgJALD-yGXc9gQxLbAeRaMQeKmUy3BI7dQ, accessed on 2017-12-25.

6. Cheng, T.-H. (2004). Method for calibration and correction of radial lens distortion, from https://patents.google.com/patent/WO2003043308A2, accessed on 2017-11-23.

7. Remondino, F., (2006). Digital camera calibration methods: considerations and comparisons. ISPRS Commission V Symposium "Image Engineering and Vision Metrology", vol. XXXVI, part 5, p. 266-272, from http://close-range.com/docs/Digital_camera_calibration_methods_10.1.1.67.8805.pdf, accessed on 2017-11-24.

8. Lin, T.-W., Chang, C.-Y. (2009). Enhanced calibration method for camera distortion. ICCAS-SICE 2009, p. 1115-1120.

9. Souchard, C. (2011). Estimating and removing lens distortion from scenes. US 20070098296 A1, from http://patft.uspto.gov/netacgi/nph-Parser?Sect1=PTO1&Sect2=HITOFF&d=PALL&p=1&u=%2Fnetahtml%2FPTO%2Fsrchnum.htm&r=1&f=G&l=50&s1=7,912,317.PN.&OS=PN/7,912,317&RS=PN/7,912,317, accessed on 2018-04-11.

10. Tang, Zh., Grompone von Gioi, R., Monasse, P., Morel, J.-M. (2012). High-precision camera distortion measurements with a "calibration harp". Journal of the Optical Society of America, vol. 29, no. 10, 2134-2143, DOI: 10.1364/JOSAA.29.002134, from https://www.researchgate.net/publication/233827976_High-precision_camera_distortion_measurements_with_a_calibration_harp?_sg=ONonP9P_B-XjpJbeDazL08dA7D-HsOT-uRnRFnFebvhqZXwYpEQBZ-KAE1FxH1u7LZ6WXmtkAvmCRxfQ, accessed on 2018-02-19.

11. Huang, C.-W., Chou, C.-M., Lin, T.-W., Chang, C.-Y. (2013). Adaptive calibration method for camera distortion. Journal of Vibration and Control, vol. 19, no. 1, 86-93, DOI: 10.1177/1077546311433915.

12. Villiers de, J.P., Leuschner, F.W., Geldenhuys, R. (2008). Centi-pixel accurate real-time inverse distortion correction. 2008 International Symposium on Optomechatronic Technologies. SPIE, DOI: 10.1117/12.804771, from http://researchspace.csir.co.za/dspace/bitstream/handle/10204/3168/De%20Villiers_2008.pdf;jsessionid=8225D91FFB4F-83483F8EACBFAEC67031?sequence=1, accessed on 2018-03-09.

13. Wang, A., Qiu, T., Shao, L. (2009). A simple method of radial distortion correction with centre of distortion estimation. Journal of Mathematical Imaging and Vision, vol. 35, no. 3, 165-172, DOI: 10.1007/s10851-009-0162-1, from https://www.researchgate.net/publication/220146291_A_Simple_Method_of_Radial_Distortion_Correction_with_Centre_of_Distortion_Estimation?ev=publicSearch-Header&_sg=ZC-yxkCHBQNdXXgFymjkD9hBVI-uxYufw2EXynpu67xcaQF0ejjXNtANda4ii8bsctNicRg6nazNVasg, accessed on 2018-03-01.

14. Zhang, Z., Matsushita, Y., Ma, Y. (2014). Camera calibration with lens distortion from low-rank textures. Patent: US8818132B2, from http://perception.csl.illinois.edu/matrix-rank/Files/calibration.pdf, accessed on 2018-03-27.

15. Wenzel, K., Ábrahám, G., Tamás, P., Urbin, Á. (2015). Measurement of distortion using the moiré interferometry. Optics, vol. 4, no. 3-1, 14-17, DOI: 10.11648/j.optics.s.2015040301.14, from http://article.sciencepublishinggroup.com/html/10.11648.j.optics.s.2015040301.14.html, accessed on 2018-03-19.

16. Kurkov, V.M. (1980). Methods of recording systematic aberrations of an aero photograph. Selfcalibration. Izvestiya Vuzov. Geodezy and Aero Photograpy, no. 6, 75-79.

17. Volkov, D.Yu., Gryaznov, N.A., Kovalev, I.A., Sosnov, E.N. (2017). High luminosity objective. Patent on useful model RU No.169945 as of 07.04.2017.

18. Volkov, D.Yu., Gryaznov, N.A., Kovalev, I.A., Sosnov, E.N. (2017). High luminosity objective. Patent on useful model RU No.169342 as of 15.03.2017.

AUTHOR'S INFORMATION

[1]The Russian State Scientific Center for Robotics and Technical Cybernetics (RTC).

[2]The Russian State Scientific Center for Robotics and Technical Cybernetics (RTC).

[3]The Russian State Scientific Center for Robotics and Technical Cybernetics (RTC).

[4]The Russian State Scientific Center for Robotics and Technical Cybernetics (RTC).

[5]The Russian State Scientific Center for Robotics and Technical Cybernetics (RTC).

[6]The Russian State Scientific Center for Robotics and Technical Cybernetics (RTC).

[7]Saint Petersburg Electrotechnical University "LETI".

Aleksandr Krotov was born in 1989, in Leningrad. He received a Professional Engineering degree from Saint Petersburg State Electrotechnical University (2012). He is currently a researcher at the Institute of Photonics, Electronics and Telecommunications of RTU Faculty of Computer Science, Information Technology and Energy.